Engineering Hybrid Interfaces of Organic – Inorganic 2D Semiconductors

by

Che-Hsuan Cheng

A dissertation submitted in partial fulfillment
of the requirements for the degree of
Doctor of Philosophy
(Materials Science and Engineering)
in the University of Michigan
2022

Doctoral Committee:

Assistant Professor Parag B. Deotare, Co-Chair
Associate Professor Emmanouil Kioupakis, Co-Chair
Professor Jinsang Kim
Professor Zetian Mi

Che-Hsuan Cheng

chehsuan@umich.edu

ORCID iD: 0000-0002-8528-6786

Dedication

This dissertation is dedicated to those who have supported me throughout this journey.

Acknowledgements

This dissertation thesis could not have been accomplished without the generous support and help of many individuals, to whom I would like to express my sincere gratitude.

First and foremost, I would like to thank my parents for their unconditional love and support that have led me to overcome many obstacles along the way. They have always been the sources of my strength and my courage throughout my life adventure.

I would like to thank my thesis advisor Prof. Parag Deotare. His insightful guidance and advice towards my research projects have brought me thus far and I cannot be more grateful. His constant encouragement towards new ideas and relentless support towards this Ph.D. degree are truly appreciated. He is my role model in the academia and his passion in academic research always motivates me to keep looking ahead.

I would like to thank my co-advisor Prof. Emmanouil Kioupakis for his guidance and support on this Ph.D. journey. His kindness always reminds me to stay positive. I would like to thank my committee members Prof. Jinsang Kim for his professional insights on organic molecules and Prof. Zetian Mi for his extensive knowledge on semiconductor materials.

I also would like to take this opportunity to thank all my current and past lab colleagues: Dr. Darwin Cordovilla, Zidong Li, Kanak Datta, Zhengyang Lyu, Emmett Litvak, Sung Woon Jang, Aaditya Hambarde, Zhaohan Jiang, and Yuchen Kan, Their friendships and assistance throughout my Ph.D. study are greatly appreciated.

Last but not least, I would like to express my sincere gratitude to the Department of Materials Science and Engineering, Rackham Graduate School, and the University of Michigan for providing me with this great opportunity to pursue my Ph.D. in a world class institution.

Copyright acknowledgements

Table of Contents

List of Tables

List of Figures

Abstract

The unique properties of two-dimensional (2D) materials have inspired widespread interests in integrating distinct 2D materials into van der Waals (vdW) heterojunctions for innovative device configurations. The organic-inorganic heterojunctions, combining atomically thin inorganic semiconductors with a wide variety of organic molecules, provide versatile platforms not only for the exploration of novel physical phenomena at nanoscale but also for the development of emerging device applications with promising functionalities. Since the hybridization optimizes the intrinsic properties of organics and inorganics, the heterojunctions have been shown to exhibit enhanced electrical and optical performances. In this thesis, we explore the science and applications of two hybrid interfacial systems that consist of organic molecules and inorganic transition metal dichalcogenides (TMD) monolayers.

In the first part, we investigate the energy transfer mechanisms across the hybrid interface of j-aggregates of organic dye and monolayer molybdenum disulphide (MoS_2) by using phototransistor's photoresponsivity. The hybrid interface combines high absorption of organics with high charge mobility of inorganics. Besides, the spectral alignment between the emission of j-aggregates and the absorption of MoS_2 *B*-exciton in the material system enables the study of Förster resonance energy transfer (FRET) across the hybrid interface. The hybrid phototransistors show nearly 93 ± 5 % enhancement of photoresponsivity in the excitonic spectral overlap regime due to efficient energy transfer from j-aggregate to MoS_2. We also report a short Förster radius of

1.88 nm for the hybrid system. Based on the study, we then investigate the energy transport dynamics of hybrid charge transfer exciton (HCTE), a quasi-particle formed by another energy transfer mechanism Dexter energy transfer (DET) in this hybrid system. Following photoexcitation, highly diffusive *hot* HCTEs are formed in about 36 ps *via* scattering with optical phonons at the hybrid interface. Once the energy drops below the optical phonon energy, the excess kinetic energy is relaxed slowly *via* acoustic phonon scattering. As a result, the energy transport that is initially dominated by highly diffusive *hot* HCTEs transition into slower *cold* HCTEs in about 110 ps. By using Fröhlich and deformation potential theory, we model the exciton-phonon interactions and attribute the prolonged transport of *hot* HCTEs to phonon bottleneck. We also find that the diffusivity of HCTEs in both *hot* and *cold* transport regions is higher than the diffusivity of MoS_2 *A* exciton.

In the second part, we explore another organic-2D TMDs hybrid system and utilize nanoscale strain engineering to create a self-erasable and rewritable optoexcitonic platform. We employ the reversible structural change of azobenzene based (A3) molecules to strain the overlying monolayer tungsten diselenide (WSe_2), and consequently, tune its optical bandgap. By using such a hybrid material combination, we are able to generate large (>1%) local strain that results in dramatic photoluminescence (PL) wavelength shift (> 11 nm). The strain in layered A3 molecules can be relaxed under visible light exposure or can be retained up to seven days under dark condition. Based on the study, we use the same hybrid materials system and apply the principles to develop high performance hybrid transistor devices. The strain is created in an ultrathin monolayer WSe_2 conducting channel by the photoisomerization of A3 molecules. The carrier mobility of the hybrid transistor can be tuned from 50 to as high as 125 cm^2/Vs using the induced

strain. Besides, the hybrid transistor exhibits a superior UV responsivity of 155 A/W, more than four times higher than in bare WSe_2.

Chapter 1 Introduction

1.1 Background and motivation

Since the revolutionary discovery of graphene and the emergence of two-dimensional (2D) van der Waals (vdW) semiconductors, numerous efforts have been inspired to fundamentally study their scientific properties and integrate them for advanced electronic and optoelectronic devices. Conventional limitations in bulk inorganic semiconductors have been overcome by atomically thin material systems with ultra-flat surfaces, high surface sensitivity, strong spin-orbit coupling, and direct to indirect band gap transition as a result of quantum confinement[1,2]. Among the commonly studied 2D materials, transition metal dichalcogenides (TMDs) such as MoS_2 and WSe_2 have received increasing attention recently due to their robustness and unique electronic, optical, and mechanical properties. Besides, these materials exhibit extraordinary characteristics such as dangling-bond free surface, atomic-scale thickness, and strong light-matter interaction, opening up new scientific and technological opportunities beyond the reach of other materials[3,4]. Even though 2D TMDs exhibit a variety of new properties that are distinct from traditional bulk semiconductors or thin films, developing such materials into large-scale and defect-free atomic layers with thickness controllability on desired substrates is still challenging. The state-of-art mechanical exfoliation method produces high quality monolayers of TMDs, but this technique is not scalable. Chemical vapor deposition (CVD) has been developed as a possible solution due to its potential for high scalability and degree of morphological control[5,6].

The field of organics has been well-established in terms of synthesis, characterization and device applications. In contrast to their inorganic counterparts, organic molecules hold key unrivalled advantages such as low production costs, versatile synthesis processes, wide variety of choices, high compatibility with any substrate including transparent glass and flexible polymeric materials. In particular, organic semiconductors have high absorption coefficients owing to their large wavefunction overlap between the ground state and the lowest excited state, thus validating strong light absorption of organic materials and making them advantageous for optoelectronic devices. Despite the prototypical demonstrations of organic materials, the performance of organic electronic devices is apparently left behind by their inorganic counterparts, due mostly to the low charge carrier mobility, low efficiency in charge injection, and inferior stabilities of the organic materials[7-9]. The incorporation of 2D TMDs with organic molecules into weakly bonded van der Waals heterostructures can leverage on the well-developed organic semiconductor technologies and unique properties of 2D TMDs, and thus improving the overall figures of merit of the hybrid platform. Figure 1.1 summarizes the applications of organic-2D TMDs heterojunction for enhanced device performance[10].

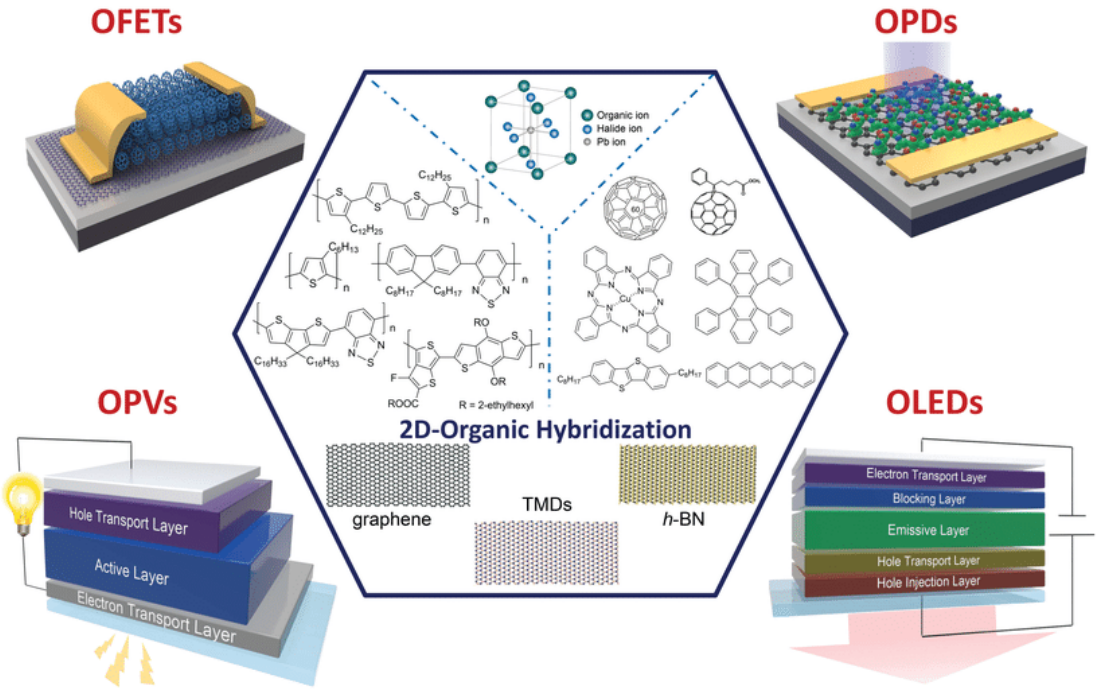

Figure 1.1 Device applications of organic-2D TMDs hybridization for enhanced performance. Adapted from reference 10.

1.2 Transition metal dichalcogenide (TMD) monolayers

Transition-metal dichalcogenide (TMD) monolayers are atomically thin semiconductors with chemical formula MX_2, where M is a transition-metal atom such as Mo and W, and X is a chalcogen atom such as S and Se. TMD monolayers consist of one layer of M atoms sandwiched between two layers of X atoms. They are layered materials, like graphene, that stack together via the weak van der Waals (vdW) interactions. As part of the large family of 2D materials, TMDs possess extraordinary atomic scale thinness with the thickness of a single layer ranging from 6.5 Å to 9 Å. A key aspect of TMDs is the evolution of the electronic band structure with respect to the number of layers. When the dimension of the materials decreases from three-dimensional bulk to two-dimensional atomically thin films, the increase of quantum confinement, interlayer coupling, and

symmetry elements result in dramatic changes of the electronic band structure[11-13]. Fascinating phenomena such as indirect-to-direct bandgap transition, bandgap broadening, large exciton binding energies, and valley polarization are absent in their bulk forms[14-16]. Figure 1.2 shows the band structure evolution of MoS_2 from bulk, quadrilayer, bilayer, to monolayer, using first principles density functional theory (DFT) calculations[11]. The calculated bandgap for bulk MoS_2 is 0.88 eV with valence band (VB) maximum located at the Γ point and a conduction band (CB) minimum located at the midpoint along Γ–K. By contrast, monolayer MoS_2 has a bandgap of 1.71 eV with both VB maximum and CB minimum located at the K point[11]. This indirect to direct bandgap change due to quantum confinement effect shows strong potential for advanced optoelectronics. Figure 1.3 lists the energy levels of conduction band and valence band of some of the most studied TMD monolayers[17]. Compared to their bulk counterpart, the photoluminescence quantum yield in monolayer MoS_2 is enhanced by more than 4 orders of magnitude[18], indicating the transition to direct band gap in monolayer MoS_2. Similar phenomena are also observed for other TMD monolayers, such as WS_2 and WSe_2. Compared to conventional semiconductors, excitons in TMD monolayers exhibit relatively large binding energies that can survive at room temperature environment, a property typically found in Frenkel excitons of organic semiconductors. Along with strong light matter interactions at nanoscale, TMD monolayers provide ideal platforms to study excitonic behaviors at the hybrid interfaces. These diverse properties of 2D TMD monolayers enable a wide range of applications in flexible devices, including field-effect transistors (FETs), photovoltaics, photodetectors, and sensors[19-22].

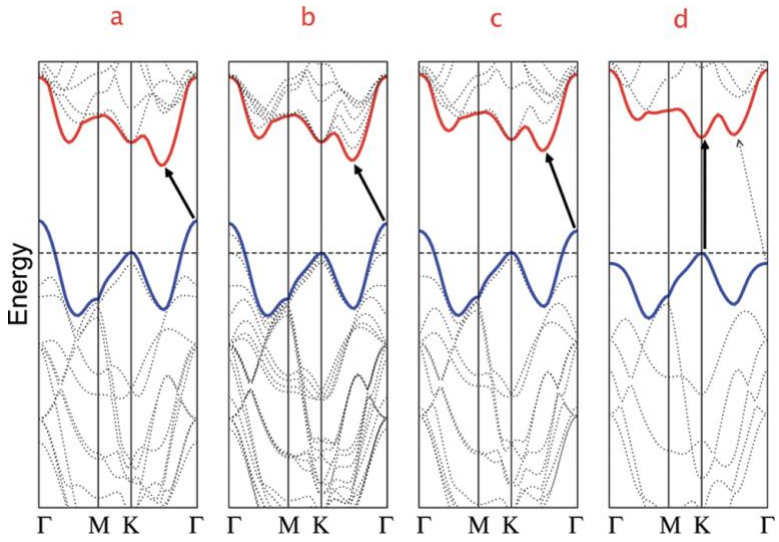

Figure 1.2 Bandgap evolution of MoS_2 with decreasing number of layers. (a)Bulk. (b)Quadrilayer. (c)Bilayer. (d)Monolayer. Adapted from reference 11.

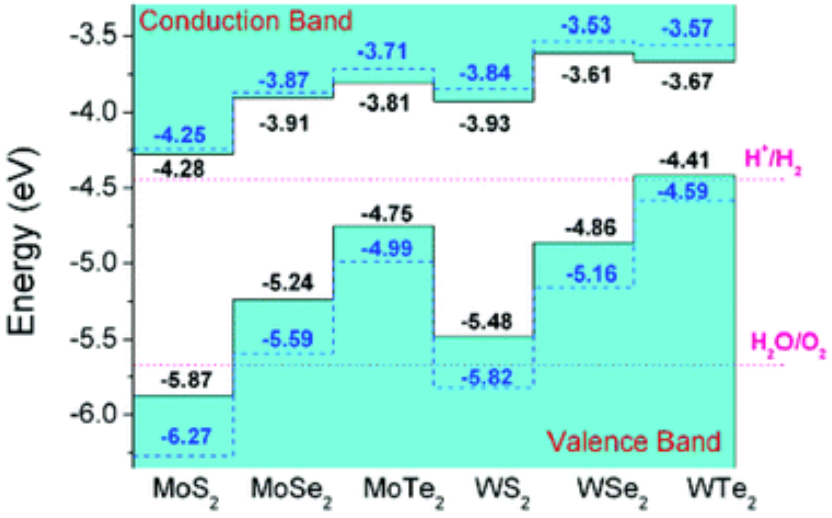

Figure 1.3 Conduction band and valence band energy levels of some common TMD monolayers. Adapted from reference 17.

1.3 Organic-inorganic hybrid interfaces

The specific disparities between organics and inorganics have inspired the idea of marrying the materials from the two worlds to form organic-inorganic heterojunctions, which will not only optimize the intrinsic properties of organic and inorganic materials but also enable brand new capabilities to the hybrid system and broaden the horizon of individual components toward innovative and multi-functional applications. Besides, energy dynamics associated with the Frenkel excitons in organics and Wannier-Mott excitons in inorganics at the hybrid heterojunctions remains an underexplored territory and the prime motivation of this thesis work. Understanding the rich physics behind the unique phenomena at the hybrid organic-2D-TMD interfaces is the key to the rational bottom-up design of hybrid organic-2D-TMD devices. The solid-state electronic devices covering both fields of organic electronics and inorganic electronics have undergone booming development in the past few decades due to wide and intensive exploration. The electronic devices based on organic-inorganic heterojunctions, particularly field-effect transistors and photodetectors, generally present the functionalities and advantages combined from the two kinds of constituent materials.

1.3.1 Field-effect transistors

A field-effect transistor (FET) is the fundamental building block in the modern electronic industry. Transistors based on two-dimensional materials are promising for scaling-down and device miniaturization. Although considerable efforts have been devoted toward the development of two-dimensional material based FETs, the performances of these devices are not promising enough for them to completely replace conventional silicon-based electronics. The hybridization of organic semiconductors and 2D TMD materials brings more intriguing transistor performance, such as higher field-effect mobility, larger current on/off ratio, and lower voltage operation[23-25].

Figure 1.4 shows enhanced source-drain current of a hybrid organic-2D TMD transistor, where organic molecules serve as charge carrier dopant to the adjacent TMD semiconductor[26].

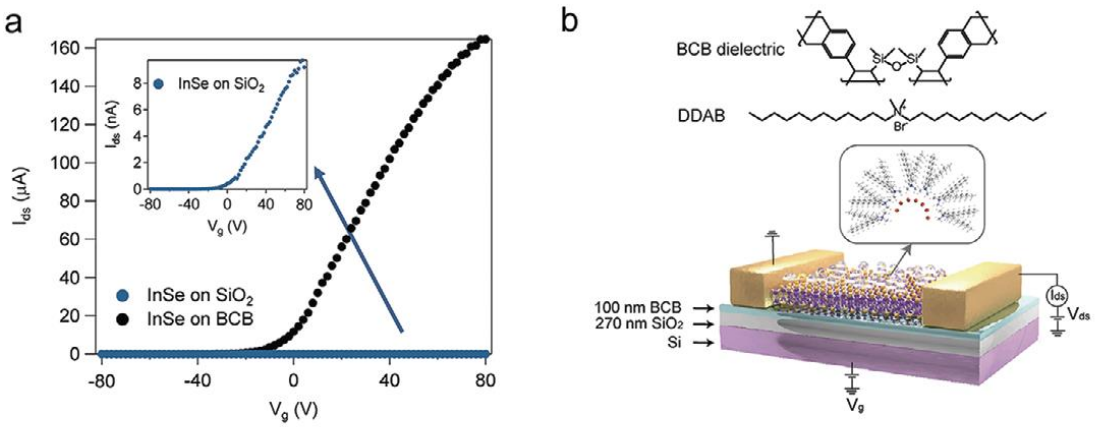

Figure 1.4 Hybrid organic-2D TMD transistor. The source-drain current is enhanced by molecular doping from the organics. Adapted from reference 26.

1.3.2 Photodetectors

As the most fundamental element in the optoelectronic devices, the photodetector, a device converting incident light into electrical signals that are compatible with the standard electronics, has widespread applications in imaging, biomedical sensing, environmental monitoring, and optical communication. The photodetectors based on 2D TMD semiconductors have broadband photodetection and high sensitivity characteristics due to their high surface to body ratio and ultrafast charge transport[27]. However, most TMDs suffer from the photoconductivity effect due to intrinsic trap states in the materials or at the interfaces in the devices[28]. While organic semiconductors are promising for use as light absorbers in which the bandgap can be modulated over a wide spectral range, 2D TMD materials offer important advantages of high mobility and a

long carrier diffusion length. With complementary properties possessed by these systems, organic-2D TMD hybrid structures hold great potential for application to high-performance photodetectors. Figure 1.5 shows a hybrid photodetector where the hybrid interface is favorably suppress the photoconductivity effect in the TMD monolayer by separating photogenerated carriers from the traps in the monolayer and the interface[29].

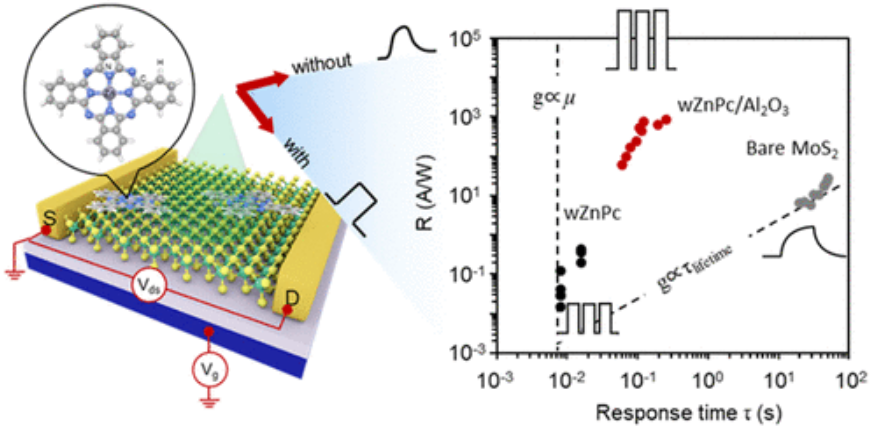

Figure 1.5 Hybrid organic-2d TMD photodetector. The organic molecules provide pathways to separate photogenerated carriers from traps, thus enhancing the photoresponsivity and shortening the response time. Adapted from reference 29.

1.4 Thesis outline

The research work in this thesis can be classified into two primary parts. The first part including Chapter 2 and 3 emphasizes on the energy transfer mechanisms and energy transport dynamics across the organic-2D TMDs hybrid interfaces. The second part including Chapter 4 and 5 focuses on the applications of strain engineering at the hybrid interfaces that utilize photoactive organic molecules and TMD monolayers.

This thesis consists of six chapters. The first chapter introduces the scientific background of organic and inorganic 2D semiconductors and the motivation to theoretically and experimentally study the dynamics of charges and excitons across the organic-inorganic hybrid interfaces. The second chapter discusses the energy transfer process and mechanisms across the hybrid interface from the organic to the inorganic that result in enhanced photoresponsivity of TMD monolayer. The third chapter, which follows the study from the previous chapter and uses the same hybrid material system, focuses on the discovery of the ultrafast transport behavior of hybrid charge transfer excitons at the hybrid interface and the physics behind such phenomenon. The fourth chapter explores strain engineering, another territory of organic-2D TMD hybridization, by using photoactive organic molecules and TMD monolayer to create a self-erasable and rewritable optoexcitonic platform. The fifth chapter, which follows the work from the fourth chapter, employs strain engineering to create high performance hybrid transistors with tunable mobility and superior UV detectivity. The final chapter summarizes the research work presented in this thesis and provides some insights in the future outlook.

1.5 References

(1) Yu, S. H.; Lee, Y.; Jang, S. K.; Kang, J.; Jeon, J.; Lee, C.; Lee, J. Y.; Kim, H.; Hwang, E.; Lee, S.; Cho, J. H. Dye-Sensitized MoS_2 Photodetector with Enhanced Spectral Photoresponse. *ACS Nano* **2014**, *8*, 8285–8291.

(2) Shastry, T. A.; Balla, I.; Bergeron, H.; Amsterdam, S. H.; Marks, T. J.; Hersam, M. C. Mutual Photoluminescence Quenching and Photovoltaic Effect in Large-Area Single-Layer MoS_2-Polymer Heterojunctions. *ACS Nano* **2016**, *10*, 10573–10579.

(3) Liu, X.; Gu, J.; Ding, K.; Fan, D.; Hu, X.; Tseng, Y. W.; Lee, Y. H.; Menon, V.; Forrest, S. R. Photoresponse of an Organic Semiconductor/Two-Dimensional Transition Metal Dichalcogenide Heterojunction. *Nano Lett.* **2017**, *17*, 3176–3181.

(4) Huang, Y. L.; Zheng, Y. J.; Song, Z.; Chi, D.; Wee, A. T. S.; Quek, S. Y. The Organic–2D Transition Metal Dichalcogenide Heterointerface. *Chem. Soc. Rev.* **2018,** *47, 3241-3264*.

(5) Jariwala, D.; Howell, S. L.; Chen, K. S.; Kang, J.; Sangwan, V. K.; Filippone, S. A.; Turrisi, R.; Marks, T. J.; Lauhon, L. J.; Hersam, M. C. Hybrid, Gate-Tunable, van Der Waals p-n Heterojunctions from Pentacene and MoS2. *Nano Lett.* **2016**, *16*, 497–503.

(6) Petoukhoff, C. E.; Krishna, M. B. M.; Voiry, D.; Bozkurt, I.; Deckoff-Jones, S.; Chhowalla, M.; O'Carroll, D. M.; Dani, K. M. Ultrafast Charge Transfer and Enhanced Absorption in MoS2-Organic van Der Waals Heterojunctions Using Plasmonic Metasurfaces. *ACS Nano* **2016**, *10*, 9899–9908.

(7) Flatten, L. C.; Coles, D. M.; He, Z.; Lidzey, D. G.; Taylor, R. A.; Warner, J. H.; Smith, J. M. Electrically Tunable Organic-Inorganic Hybrid Polaritons with Monolayer WS2. *Nat. Commun.* **2017**, *8*, 1608.05274.

(8) Homan, S. B.; Sangwan, V. K.; Balla, I.; Bergeron, H.; Weiss, E. A.; Hersam, M. C. Ultrafast Exciton Dissociation and Long-Lived Charge Separation in a Photovoltaic Pentacene-MoS2van Der Waals Heterojunction. *Nano Lett.* **2017**, *17*, 164–169.

(9) Zheng, Y. J.; Huang, Y. L.; Chen, Y.; Zhao, W.; Eda, G.; Spataru, C. D.; Zhang, W.; Chang, Y. H.; Li, L. J.; Chi, D.; Quek, S. Y.; Wee, A. T. S. Heterointerface Screening Effects between Organic Monolayers and Monolayer Transition Metal Dichalcogenides. *ACS Nano* **2016**, *10*, 2476–2484.

(10) Reers, M.; Smith, T. W.; Chen, L. B. J-Aggregate Formation of a Carbocyanine as a Quantitative Fluorescent Indicator of Membrane Potential. *Biochemistry* **1991**, *30*, 4480–4486.

(11) Kuroda, S. I.; Ito, H.; Uchiyama, Y.; Mori, T.; Marumoto, K.; Hatta, I. J-Aggregate Formation of 6-Methyl-Merocyanine Dye in Mixed Langmuir-Blodgett Films with Arachidic Acid in a Wide Range of Mixing Ratio. *Japanese J. Appl. Physics, Part 1 Regul. Pap. Short Notes Rev. Pap.* **2002**, *41*, 6223–6227.

(12) Bradley, M. S.; Tischler, J. R.; Bulović, V. Layer-by-Layer J-Aggregate Thin Films with a Peak Absorption Constant of 106 Cm-1. *Adv. Mater.* **2005**, *17*, 1881–1886.

(13) Peyratout, C.; Daehne, L. Aggregation of Thiacyanine Derivatives on Polyelectrolytes. *Phys. Chem. Chem. Phys.* **2002**, *4*, 3032–3039.

(14) Lee, J.-H.; Min, C.-K.; Joo, T. Ultrafast Optical Dynamics of Excitons in J-Aggregates Optical Dynamics of Excitons in Aggregates of a Carbocyanine Dye Ultrafast Optical Dynamics of Excitons in J-Aggregates. *J. Chem. Phys. J. Chem. Phys. J. Chem. Phys. J Aggreg. J. Chem. Phys.* **2001**, *1141*.

(15) Walker, B. J.; Dorn, A.; Bulović, V.; Bawendi, M. G. Color-Selective Photocurrent Enhancement in Coupled J-Aggregate/Nanowires Formed in Solution. *Nano Lett.* **2011**, *11*, 2655–2659.

(16) Balandin, A. A.; Nika, D. L. Phononics in Low-Dimensional Materials. *Mater. Today* **2012**, *15*, 266–275.

(17) Mas-Ballesté, R.; Gómez-Navarro, C.; Gómez-Herrero, J.; Zamora, F. 2D Materials: To Graphene and Beyond. *Nanoscale* **2011**, *3*, 20–30.

(18) Fiori, G.; Bonaccorso, F.; Iannaccone, G.; Palacios, T.; Neumaier, D.; Seabaugh, A.; Banerjee, S. K.; Colombo, L. Electronics Based on Two-Dimensional Materials. *Nat. Nanotechnol.* **2014**, *9*, 768–779.

(19) Manzeli, S.; Ovchinnikov, D.; Pasquier, D.; Yazyev, O. V.; Kis, A. 2D Transition Metal Dichalcogenides. *Nat. Rev. Mater.* **2017**, *2*, 17033.

(20) Lopez-Sanchez, O.; Lembke, D.; Kayci, M.; Radenovic, A.; Kis, A. Ultrasensitive Photodetectors Based on Monolayer MoS 2. *Nat. Nanotechnol.* **2013**, *8*, 497–501.

(21) Yin, Z.; Li, H.; Li, H.; Jiang, L.; Shi, Y.; Sun, Y.; Lu, G.; Zhang, Q.; Chen, X.; Zhang, H. Single-Layer MoS2phototransistors. *ACS Nano* **2012**, *6*, 74–80.

(22) Zhang, W.; Chiu, M. H.; Chen, C. H.; Chen, W.; Li, L. J.; Wee, A. T. S. Role of Metal Contacts in High-Performance Phototransistors Based on WSe2monolayers. *ACS Nano* **2014**, *8*, 8653–8661.

(23) Choi, W.; Cho, M. Y.; Konar, A.; Lee, J. H.; Cha, G. B.; Hong, S. C.; Kim, S.; Kim, J.; Jena, D.; Joo, J.; Kim, S. High-Detectivity Multilayer MoS2 Phototransistors with Spectral Response from Ultraviolet to Infrared. *Adv. Mater.* **2012**, *24*, 5832–5836.

(24) Yin, Z.; Li, H.; Li, H.; Jiang, L.; Shi, Y.; Sun, Y.; Lu, G.; Zhang, Q.; Chen, X.; Zhang, H. Single-Layer MoS2 Phototransistors. *ACS Nano* **2011**, *6*, 74–80.

(25) Lopez-Sanchez, O.; Dumcenco, D. O.; Charbon, E.; Kis, A. Avalanche Photodiodes Based on MoS2 / Si Heterojunctions. *ArXiv e-prints* **2014**.

(26) Tsai, D. S.; Liu, K. K.; Lien, D. H.; Tsai, M. L.; Kang, C. F.; Lin, C. A.; Li, L. J.; He, J. H. Few-Layer MoS2 with High Broadband Photogain and Fast Optical Switching for Use in Harsh Environments. *ACS Nano* **2013**, *7*, 3905–3911.

(27) Zhong, X.; Zhou, W.; Peng, Y.; Zhou, Y.; Zhou, F.; Yin, Y.; Tang, D. Multi-Layered MoS 2 Phototransistors as High Performance Photovoltaic Cells and Self-Powered Photodetectors. *RSC Adv.* **2015**, *5*, 45239–45248.

(28) Bie, Y.-Q.; Grosso, G.; Heuck, M.; Furchi, M. M.; Cao, Y.; Zheng, J.; Bunandar, D.; Navarro-Moratalla, E.; Zhou, L.; Efetov, D. K.; Taniguchi, T.; Watanabe, K.; Kong, J.; Englund, D.; Jarillo-Herrero, P. A MoTe2-Based Light-Emitting Diode and Photodetector for Silicon Photonic Integrated Circuits. *Nat. Nanotechnol.* **2017**, 1–19.

(29) Lopez-Sanchez, O.; Lembke, D.; Kayci, M.; Radenovic, A.; Kis, A. Ultrasensitive Photodetectors Based on Monolayer MoS2. *Nat. Nanotechnol.* **2013**, *8*, 497–501.

Chapter 2 Energy Transfer across Organic – Inorganic Hybrid Interfaces

2.1 Introduction

Devices made from organic semiconductors today rival inorganic devices in niche areas such as displays and flexible photovoltaics. The unique photophysical properties such as tunable bandgap, high exciton binding energy and thermal independence along with the ability to deposit materials in the form of thin films make organic semiconductors particularly suitable for the above energy conversion applications. These unique properties of organics when compared to inorganic materials primarily arise from the difference in the nature of chemical existence. While inorganics are mostly crystalline solids with covalent or ionic bonds, organics are dominantly covalent bonded molecular solids.

Not surprisingly, investigations to understand the organic-inorganic semiconductor interfaces, especially in terms of energy transport has gathered a lot of interest of the research community.[1–7] The hybrid heterojunction formed by combining inorganic and organic semiconductors offers a unique platform that can reap the benefits of both the material systems. For instance, organics are well known for the strong absorption but have poor charge mobility, whereas inorganics have comparably low absorption but excellent charge transport properties. Pairing these disparate systems can not only lead to a new material system that is highly absorptive with exception mobility but also enable control over band-like transport in inorganics to charge hopping transport in organics.[8,9] However, energy dynamics associated with the Frenkel excitons

in organics and Wannier-Mott excitons in inorganics at the hybrid heterojunctions remains an untrespassed area and the prime motivation of this research. The hybrid heterojunctions offer a unique platform to study unknown rich physics associated with ET processes and could open plethora of applications ranging from biochemical sensing, ambient lighting, photovoltaics to beyond CMOS devices.

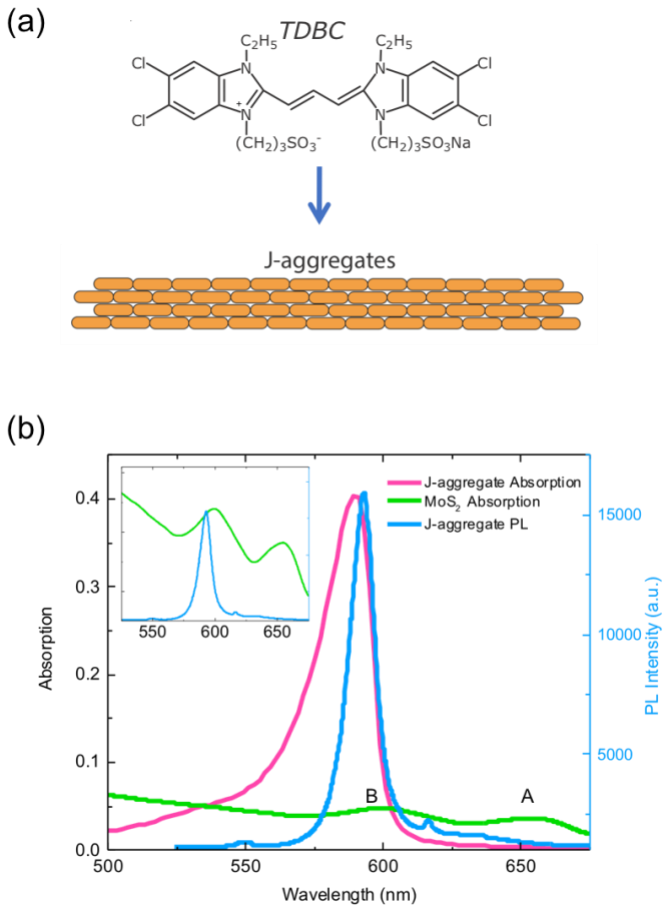

Figure 2.1 Spectral alignment of MoS_2 and TDBC j-aggregate. (a) Chemical structure of organic dye TDBC and the head-to-tail molecule orientation in its j-aggregate form. (b) Spectra showing j-aggregate absorption, PL emission, and MoS_2 absorption. *A* and *B* excitonic resonances of MoS_2 at 655 and 599 nm were denoted on the figure, respectively. The inset figure shows the normalized spectra, highlighting the spectral overlap between j-aggregate emission and MoS_2 *B* exciton absorption.

In this work we fabricate a hybrid photodetector based on an organic-inorganic heterojunction and use it as a platform to study the ET process across the interface. The photodetector features a heterojunction made of highly absorbing j-aggregate thin film of organic dye TDBC (5,6-dichloro-2[3-[5,6-dichloro-1-ethyl-3-(3-sulfopropyl)-2(3H)-benzimidazolidene]-1-propenyl]-1-ethyl-3-(3-sulfopropyl) benzimidazolium hydroxide) and a monolayer Molybdenum disulphide (MoS_2). J-aggregates of organic dyes are formed due to dipole alignment of fluorescent molecules as shown in Figure 2.1a . The expected head-to-tail arrangement of molecules in j-aggregates is identified by the narrow and intense absorption spectrum.[10–13] The absorption spectrum of TDBC shifts from a broad monomer band centered around 515 nm to a strong and narrow j-band peaked at 590 nm, while the photoluminescence (PL) peak is red shifted by just 4 nm as shown in **Error! Reference source not found.**b.[14] The peak absorption coefficient c an be as high as 10^6 cm^{-1} for a thin film of 5 nm.[12] These light sensitive aggregate films have been utilized to enhance the photocurrent of inorganic nanowires, where the organic molecules act as donors and the inorganic semiconducting nanowires as acceptors, giving rise to a presumably efficient charge transfer across their interface.[15]

We use monolayers of MoS_2, as the inorganic material due to its atomic scale two-dimensionality, which is the physical limit that cannot be achieved using other engineered structures and excellent spectral overlap with TDBC j-aggregate. It belongs to the well-known class of van der Waals materials known as transition metal dichalcogenides (TMDs) that not only exhibit layer by layer two-dimensional structure, but also support a semiconducting bandgap that can be utilized for designing optical devices.[16–19] These materials are characterized by a stable room temperature Wannier-Mott exciton, high absorption of light per monolayer, valley degree of polarization and strong non-linear optical response. Numerous applications including

photodetectors,[20–29] field effect transistors,[18,30–37] light emitting diodes,[28,33,38–40] and solar cells[2,27,34,41–43] have been demonstrated, establishing its potential as a future optoelectronic material platform. As shown in Figure 2.1b, the *B* excitonic[44] absorption peak of MoS_2 has high spectral overlap with the j-aggregate PL emission. The inset in Figure 2.1b shows the normalized MoS_2 absorption and j-aggregate PL spectra for easier visualization of the overlap. The MoS_2 resonances are very sensitive to the local dielectric environment (substrate).[45,46] We found that the *B* excitonic resonance were typically located at 595 nm for the photodetector samples further improving the overlap. The peak shown in Figure 2.1b is slightly red shifted, due to a different substrate (transparent) used for collecting the absorption data.

While energy transport between donor-acceptor pairs is traditionally studied by measuring photoluminescence (PL) quenching and exciton lifetime,[47–50] we demonstrate a new approach that can be used for studying material systems with short exciton lifetimes that fall beyond the measurement capabilities of the commonly used time correlated single photon counting (TCSPC) technique. Photodetectors fabricated using the proposed material system with varying separation between the two materials, provides an excellent platform to study the ET process. Using this concept, we not only study the ET mechanism across the sharp organic-TMD interface but also use the hybrid platform to demonstrate the feasibility of the material platform for fabricating ultrasensitive photodetectors.

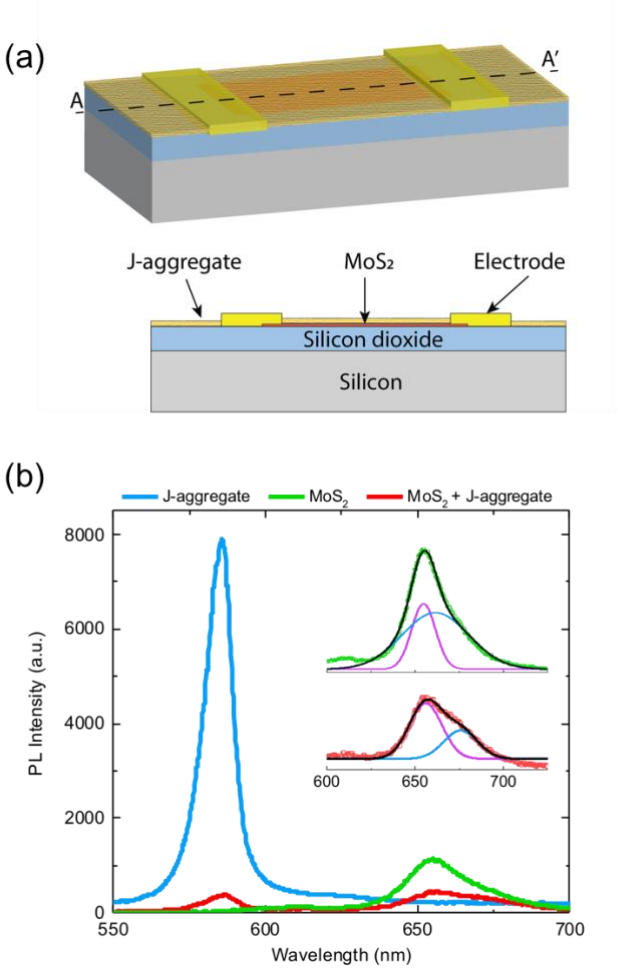

Figure 2.2 Monolayer MoS_2 photodetector sensitized by TDBC j-aggregate. (a) The schematic diagram of the device. (b) PL emission spectra from TDBC j-aggregate, monolayer MoS_2, and monolayer MoS_2/j-aggregate heterostructure. PL quenching is observed for both materials in the heterostructure region. The inset shows the Gaussian fitted neutral exciton (purple), trion (blue), and overall (black) peaks. The redshift of trion peak along with lowering of intensity of neutral exciton peak after TDBC j-aggregate deposition suggest *n* doping of MoS_2 monolayer by TDBC j-aggregates.

2.2 Results and discussion

2.2.1 Device fabrication

Monolayers of MoS_2 were prepared on a 300 nm SiO_2/Si substrate using mechanical exfoliation and an all-dry transfer method. The dimensions of the monolayers ranged between 20 µm to 200 µm. Raman spectroscopy and atomic force microscopy (AFM) was used for confirming the thickness of exfoliated samples. The thickness of the monolayers was measured to be approximately 0.7 nm, which matched well with values reported in literature.[51] Electrodes were fabricated on the MoS_2 monolayers by photolithography followed by metal deposition and lift off. The schematic diagram of the device is shown in Figure 2.2a. J-aggregate film was deposited on top of the monolayer MoS_2 using layer-by-layer deposition by immersing the device alternately in TDBC and polyelectrolyte solutions.[12] A thin film of 5.5 bilayers was deposited on all devices. Further information on device fabrication can be found in methods section.

2.2.2 PL spectra analysis

The PL spectra of monolayer MoS_2, TDBC j-aggregate, and MoS_2/j-aggregate at a constant excitation density are shown in Figure 2.2b. A significant decrease in the emission intensity of j-aggregate was observed in coupled MoS_2/j-aggregate hetero-region. As mentioned earlier, near perfect spectral overlap between j-aggregate PL and monolayer MoS_2 absorption provides a suitable condition for the photo generated excitons in j-aggregate thin film to transfer its energy to MoS_2 layer through Förster Resonance Energy Transfer (FRET).[47,49,50,52] ET through charge exchange can also occur at short distances due to wave function overlap through Dexter mechanism (DET).[53] Both mechanisms result in the significant decrease of j-aggregate PL

emission intensity, as seen in Figure 2.2b. In spite of the efficient ET from j-aggregate thin film, the monolayer MoS_2 PL appears to be quenched. This PL quenching is due to the charge transfer across the interface and has been reported as mutual photoluminescence quenching[2] due to type II energy band alignment between two materials (Inset of Figure 2.3a shows the optical band gaps). To support the argument, the PL spectra from bare monolayer MoS_2 and monolayer MoS_2/j-aggregate hetero-junction are fitted with two Gaussians corresponding to neutral and charged exciton (trion) as shown in the inset of Figure 2.2b. The hetero-junction PL shows a red shifted trion peak and a reduced neutral exciton peak intensity suggesting *n* doping of MoS_2 by j-aggregate thin film. This agrees well with reported work on doping dependent PL of TMDs.[54,55]

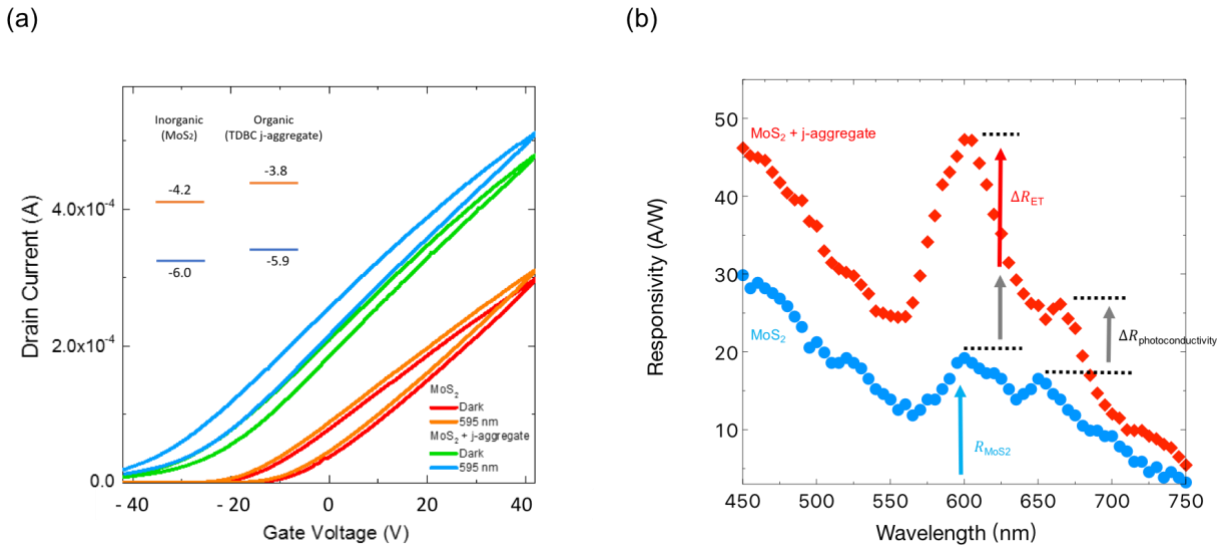

Figure 2.3 Enhanced photoresponse of monolayer MoS_2 photodetector after TDBC j-aggregate deposition. (a) IV characteristics of the photodetector before and after j-aggregate deposition. The excitation wavelength is 595 nm. Inset: optical band gaps of monolayer MoS_2 and TDBC j-aggregate show type II energy band alignment between two materials. (b) Wavelength dependent photoresponsivity before (blue) and after (red) j-aggregate deposition. The responsivity enhancement near j-aggregate absorption has contributions from ET and photoconductive gain increase, as shown in the figure.

2.2.3 Photoresponse characterization

The photoresponse of the intrinsic MoS_2 devices were measured under room temperature and ambient condition. An on/off ratio of 10^7 and a photoresponsivity of ~20 A/W at 595 nm (corresponding to *B* exciton peak) with a drain-source bias of 10 V and a back-gate voltage of 10 V was measured. Similar measurements were preformed after j-aggregate deposition in an inert nitrogen atmosphere to prevent photo oxidation. The deposited j-aggregate film is expected to absorb nearly 40 % of incident light at 590 nm and about 33 % at 595 nm (*B* exciton peak of MoS_2), contributing to the enhancement of the photoresponse of MoS_2 monolayer photodetector. Figure 2.3a compares the IV characteristics of a MoS_2 photodetector before and after j-aggregate deposition with a drain-source bias of 10 V and illumination at 595 nm (power density of 0.025 W/cm^2). As expected, higher photocurrent I_{ph}, which is defined as ($I_{light} - I_{dark}$), was observed in hybrid devices due to ET mechanisms discussed earlier. In addition, increase in the dark current after j-aggregate deposition is observed indicating *n* doping of MoS_2 monolayer by TDBC molecules.

Photoresponsivity (defined as the ratio of I_{ph} to incident power) of the photodetector before and after j-aggregate deposition were measured across the visible range (450-750 nm) as shown in Figure 2.3b. The blue dots and red squares correspond to the bare MoS_2 and MoS_2/j-aggregate devices respectively. An overall enhancement in responsivity was observed across the spectrum. This was mainly due to the change in the photoconductive gain of the photodetector.[56] The photoconductivity gain is proportional to the dark current of the device and hence contributes equally throughout the spectrum above the lowest excitonic energy state (*A* exciton).[56,57] However, a much higher enhancement in responsivity was observed corresponding to j-aggregate absorption. The extra enhancement is attributed to the efficient ET from j-aggregate to MoS_2. We note that

there is a small enhancement contribution to photoresponsivity at shorter wavelengths due to ET from the long absorption tail of the j-aggregate as shown in the spectrum in Figure 2.1. Hence, to quantify the ET contribution at *B* excitonic resonance, we subtract the overall responsivity enhancement by the enhancement at *A* excitonic resonance. The enhancement seen at the *A* excitonic resonance of MoS_2 is mostly due to photoconductivity gain. The enhancement due to ET, defined as the ratio of change in photoresponsivity after depositing j-aggregate (ΔR_{ET}) to the original bare MoS_2 (R_{MoS_2}) photoresponsivity is given by:

$$\boldsymbol{E_{ET}} = \frac{\Delta R_{total} - \Delta R_{photoconductivity}}{R_{MoS_2}} = \frac{\Delta R_{ET}}{R_{MoS_2}} \tag{2.1}$$

A maximum enhancement of 93 ± 5 % at 600 nm was estimated due to the efficient ET between the dye molecules and the semiconducting monolayer. Both FRET and DET mechanisms contribute to the enhancement due to the proximity of the two materials. The maximum enhancement wavelength should correspond to the peak absorption wavelength of j-aggregates (590 nm). However, red shift (corresponding to the maximum enhancement wavelength) in j-aggregate absorption spectra was observed upon deposition over MoS_2 (confirmed from reflectivity measurements in Figure 2.4). Similarly, red shift in MoS_2 *A* excitonic resonance was also observed upon j-aggregate deposition as shown in Figure 2.3b due to the change in the dielectric screening. Similar shift is expected for *B* excitonic resonance as well.

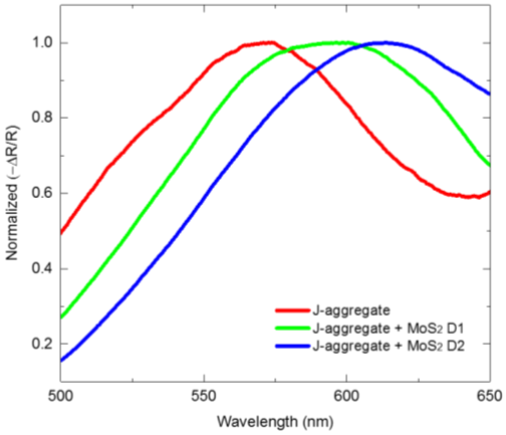

Figure 2.4 Reflection spectra ($-\Delta R/R$) of j-aggregate deposited on monolayer MoS_2 transistors and bare j-aggregate film from nearby region (same Si/SiO_2 substrate). The differential reflection is directly proportional to absorption. D1 and D2 represent two adjacent different devices. Red shifts of j-aggregate absorption were observed for both devices in the heterointerface region.

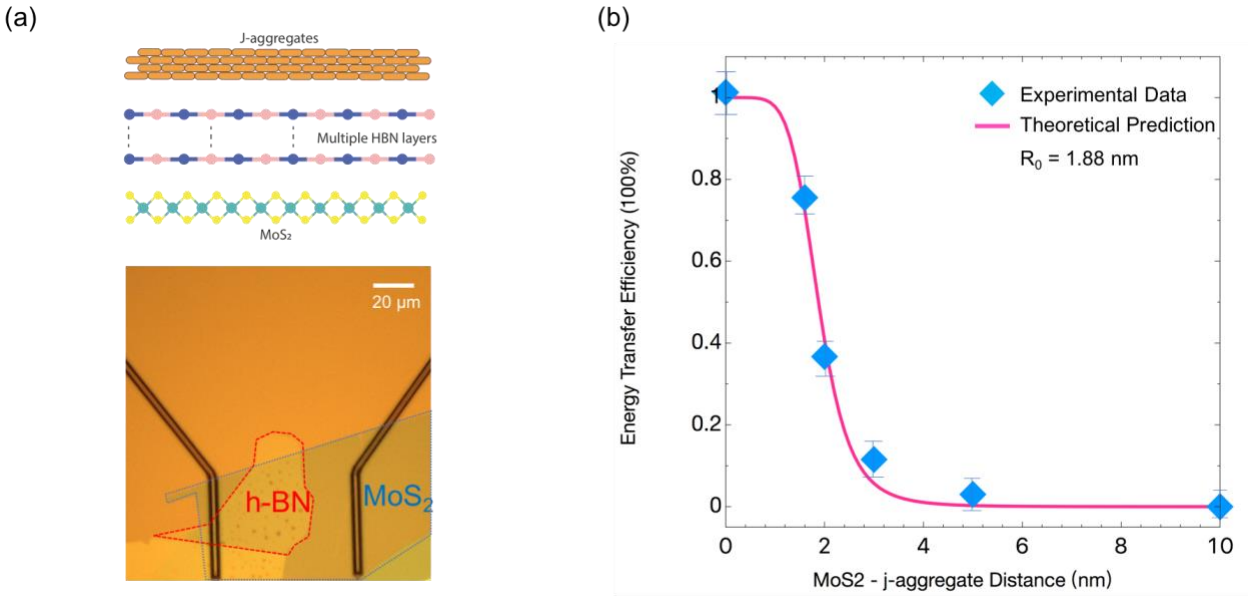

Figure 2.5 FRET efficiency between monolayer MoS_2 and TDBC j-aggregate film. (a) Schematic diagram showing the use of layered h-BN as a spacer and an optical image of a represented device with a 2 nm h-BN transferred on top of MoS_2. (b) FRET efficiency as a function of separation between MoS_2 monolayer and j-aggregate film. The solid line denoted the expected dependence using FRET theory. At 0 nm (no h-BN spacer), both FRET and DET contribute to the enhancement.

2.2.4 FRET across hybrid interface

To quantify the FRET mechanism across the organic-inorganic interface, spacing between the MoS_2 monolayer and j-aggregate thin film was varied by introducing hexagonal Boron Nitride (h-BN) layers with varying thickness of 1.6, 2, 3, 5, and 10 nm. The thickness of each h-BN flake was measured by AFM. Figure 2.5a shows the schematic diagram for the hybrid photodetector with h-BN spacer along with a bright field image of the device with a 2 nm h-BN spacer. The h-BN flakes were introduced using the same approach as MoS_2 monolayers. h-BN is a two-dimensional insulator with a single layer thickness of approximately 0.4 nm and a bandgap of 6 eV[58,59]. Thus, h-BN spacer prevents Dexter transfer (up to 1 nm) between the materials and helps to isolate the system to study the FRET process ($\boldsymbol{E_{ET} = E_{FRET}}$). We observed enhancement of MoS_2 PL for samples with thin h-BN spacers (1.6 nm) confirming suppression of charge transfer and dominance of FRET (Figure 2.6). FRET is a non-radiative emission-reabsorption process through a virtual photon that can occur within 10 nm of donor-to-acceptor distance.[50] To compare various devices, an optical excitation spot of 10 μm in diameter was used to illuminate specific regions of the sample and the devices were measured at a fixed current density of 10^{-8} A/μm^2 and a gate voltage of 10 V. Table 2.1 shows the enhancement for various devices.

Table 2.1 Photoresponsivity enhancement as a function of MoS_2 and j-aggregate distance.

MoS_2 and J-aggregate distance (nm)	0	1.6	2	3	5	10
Enhancement (100%)	93.2±5.8	67.3±5.2	32.7±4.5	10.3±4.2	2.7±3.1	0.3±1.5

The FRET efficiency (η_{FRET}) can be derived from the responsivity enhancement by:

$$\eta_{FRET} = \frac{E_{FRET}}{6.3*\eta_j*\kappa^2} \tag{2.2}$$

where $\eta_j = 0.2$ is the quantum yield of j-aggregate,[49] κ^2 is the dipole orientation factor,[60] and 6.3 is the absorption ratio of j-aggregate to MoS_2 at maximum responsivity (the maximum responsivity occurs at the maximum absorption of j-aggregate film). Since excitons in MoS_2 and j-aggregates are limited in-plane, we estimated the dipole orientation factor to be 0.7 (refer methods section)[61–63]. This is slightly higher than the generically used value of 2/3 for isotropic case. **Error! Reference source not found.**b plots the FRET efficiency for photodetectors with different h-BN thicknesses. The figure compares the measured data with values estimated using FRET theory, where FRET efficiency is given by:

$$\eta_{FRET} = \frac{1}{1+(\frac{r}{R})^6} \tag{2.3}$$

where *r* is the donor-to-acceptor separation, and *R* is the Förster radius. *R* is defined as the distance where 50% of the energy is transferred from the donor to the acceptor molecule. The FRET radius for the TDBC j-aggregate – MoS_2 pair was estimated to be 1.88 nm across the hybrid interface. Typical FRET radius between organic-organic molecules lie between 2 to 7 nm[64]. Our experimental results show a smaller FRET distance in this hybrid organic-inorganic system which tallies with previous theoretical study. This is possibly due to the small exciton Bohr radii as well as the well aligned orientations of excitons in both materials systems. The closely fitted experimental data along with their corresponding theoretical values shown in Figure 4b confirm that FRET dominates between the j-aggregate film and MoS_2 monolayer as the separation between them becomes larger than 1 nm. Less than 3% of the absorbed energy was transferred to the MoS_2

monolayer for donor-acceptor separation larger than 5 nm. As observed, the efficiency is close to 100 % for the devices without h-BN due to contributions from both FRET and DET mechanisms.

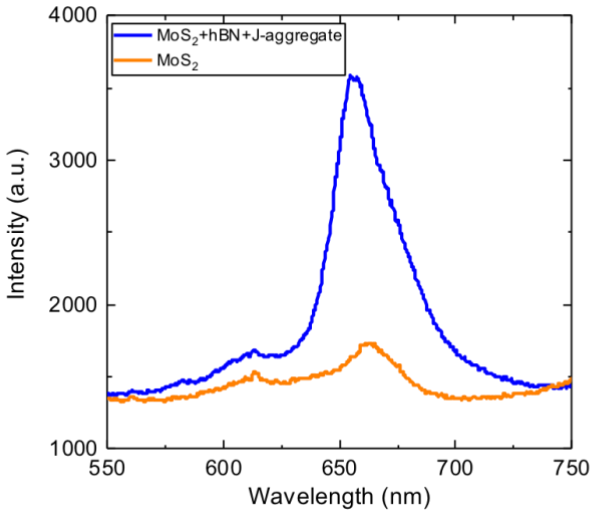

Figure 2.6 PL spectra of bare monolayer MoS_2 and MoS_2/j-aggregate hybrid layers separated by 1.6 nm h-BN. The PL intensity of MoS_2 *A* exciton peak at 665 nm was significantly enhanced after j-aggregate deposition due to efficient FRET effect. The charge transfer between two materials was suppressed by the h-BN layer.

2.3 Conclusion

In this work, we investigated the ET mechanism between a TDBC j-aggregate and monolayer MoS_2. Due to the near perfect spectral overlap between TDBC j-aggregate and MoS_2, 93 ± 5 % photoresponsivity enhancement was observed. This enhancement is attributed to FRET and Dexter charge transfer between j-aggregate thin film and monolayer MoS_2. By measuring the responsivity enhancement in a photodetector made using the hybrid organic-inorganic interface for various separation distances, a Förster radius of 1.88 nm was estimated. Such short FRET distance is primarily due to atomically thin TMD structure as well as the small exciton Bohr radii in both the material systems. This work provides a comprehensive and systematic approach of studying the ET mechanism across organic-TMD interfaces that will help improve performances of energy conversion devices. At the same time, it demonstrates the feasibility to fabricate dye sensitized TMD photodetectors with highly enhanced responsivities. While direct bandgap and the atomically thin existence with room temperature stable exciton make TMD's a prosperous optoelectronic material system, organic-TMD heterointerfaces allow us to further enhance the performance and provide control over desired optoelectronic properties. We envision these results to pave ways for further research in understanding the co-existence of Wannier Mott and Frenkel excitons as well as designing next generation energy efficient optoelectronic devices.

2.4 Methods

2.4.1 Phototransistor fabrication

MoS_2 and h-BN were exfoliated from synthetically grown crystals (2D Semiconductors) and then transferred onto Si/SiO_2 substrates using PDMS stamps (Gel Pak PF films). Potential monolayer MoS_2 samples were identified by optical contrast using Nikon upright microscope, and further confirmed using PL and Raman spectroscopy using 532 nm CW laser excitation and Princeton Instrument spectrometer (IsoPlane 320). The thickness of h-BN was measured using AFM (ICON AFM). Contact electrodes were then fabricated using photolithography, followed by metal deposition (Cr/Au with thicknesses of 10/90 nm) and lift off process.

2.4.2 TDBC j-aggregate deposition

TDBC J-aggregate films were prepared using layer-by-layer assembly with alternate polyelectrolyte (PDAC) and dye (TDBC) deposition. Both chemicals were purchased from Alfa Chemistry. The samples were first immersed into PDAC solution ($3*10^{-2}$ M) for 15 minutes and rinsed in three beakers of DI water for 2, 2, and 1 minutes respectively. The samples were then immediately transferred to the TDBC solution ($5*10^{-5}$ M) followed by the previous rinse routine. After 5 cycles, the samples were deposited with the final layer of electrolyte. To ensure uniform deposition of j-aggregate film onto the device, PL measurements were performed on random spots across the sample using a 532 nm CW laser excitation.

2.4.3 Absorption measurement

MoS_2 monolayer sample was prepared on a transparent PDMS-glass slide substrate. Fiber-coupled broadband light from a tungsten-halogen source was used to illuminate the sample and the transmitted light was collected and analyzed using a spectrometer (Princeton Instruments Spectrometer (Isoplane 320)). Transmitted/reflected spectrum from the monolayer and a background spectrum from a nearby region without the monolayer were measured. The dark current background signal was subtracted from both sets of data. If these two sets of data are T_1 (flake) and T_0 (substrate), the transmittance (T) is defined as T_1/T_0. Absorption is defined as A = 1-T-R. A 10X, 0.3 NA objective provided a spot size of ~4 μm for the measurements. All measurements were performed at room temperature. The j-aggregate absorption measurement was performed using a Perkin Elmer UV-Vis absorption spectrophotometer (Lambda 650).

2.4.4 Device testing

A probe station was used to measure the IV characteristics of the devices (2900 series source meter units from Keysight Technologies). The photoresponse of devices were measured by scanning a monochromator (Cornerstone 260, Newport Corporation) and detecting the photocurrent using a lock-in amplifier (SR830, Stanford Research Systems). A low noise current preamplifier (SR570, Stanford Research Systems) was used as an intermediate stage. The chopped monochromator light was coupled through a multimode fiber and delivered onto the sample using a 20X objective. The spot size was approximately 10 μm on the devices. The monochromator delivered an average power between 0.1 μW to 0.15 μW for the scan range of 450 nm to 750 nm at a wavelength resolution of 5 nm. An inert nitrogen environment around the probe station was created using an enclosure to avoid photo-oxidation of j-aggregates. Prior to start of the experiments, the enclosure was purged using ultrapure nitrogen (99.9999 %) for 30 minutes.

2.4.5 FRET equation derivation

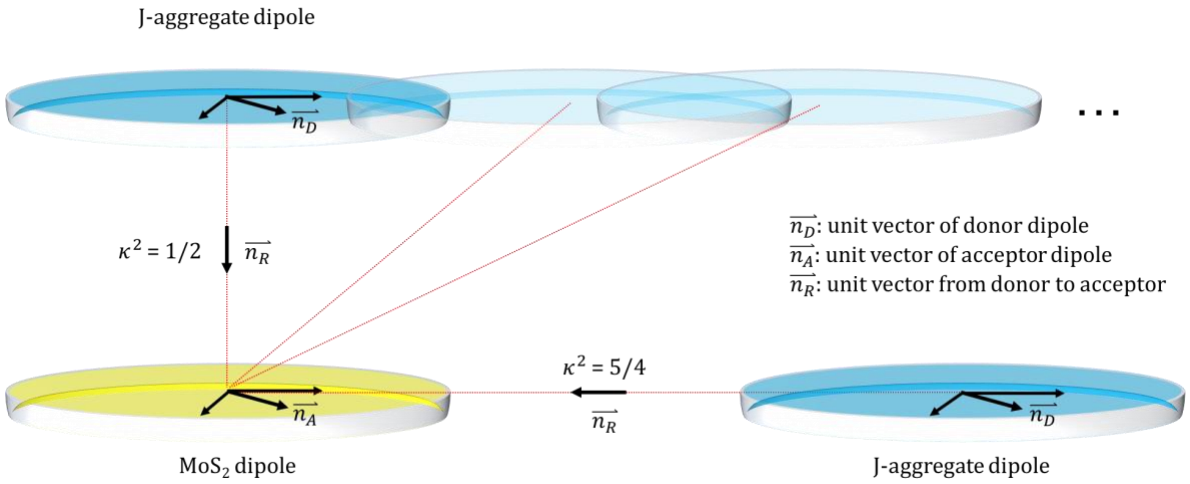

Figure 2.7 Possible dipole orientations of donor (j-aggregate) and acceptor (MoS_2). The orientation factor is maximum at head-to-tail arrangement and is minimum at parallel stacking.

Enhancement as defined in equation 2.1 can be written as:

$$E_{FRET} = \frac{A_j * \eta_j * \kappa^2 * \eta_{FRET} * IQE_{MoS_2}}{A_{MoS_2} * IQE_{MoS_2}}$$

where η_j is the quantum yield of j-aggregate, κ^2 is the orientation factor for transition dipoles, η_{FRET} is the FRET efficiency, IQE_{MoS_2} is the internal quantum efficiency of MoS_2, and A_j and A_{MoS_2} are the absorption of j-aggregate and MoS_2 respectively. The numerator represents the photocurrent increase from the light absorbed by j-aggregate and successfully transferred to MoS_2. The denominator represents the photocurrent of bare MoS_2. The FRET efficiency can be obtained from this equation based on our measured data and references.

The isotropic average value of κ^2 is 2/3 and has been taken in most FRET studies. However, this is not a valid assumption in our case of interacting thin films consisting of layer by layer

deposited j-aggregate and 2D MoS_2. We model them as 2D films and the donor and acceptor dipoles are considered to be randomly distributed in the 2D plane as shown in the following Figure 2.7.

Two extreme cases are demonstrated with one in parallel stacking and the other head-to-tail arrangement. The κ^2 value is given by:

$$\kappa^2 = [\overrightarrow{n_D} \cdot \overrightarrow{n_A} - 3(\overrightarrow{n_R} \cdot \overrightarrow{n_D})(\overrightarrow{n_R} \cdot \overrightarrow{n_A})]^2$$

The κ^2 value is 1/2 for parallel case and 5/4 for head-to-tail case. In our j-aggregate - MoS_2 interface the value should be intermediate since there may be multiple j-aggregate dipoles coupling to each MoS_2 dipole with varying $\overrightarrow{n_R}$ and polar angle ranging from 0 to $\pi/2$. The average value of 0.7 was estimated and used in our FRET calculation.

2.5 References

(1) Yu, S. H.; Lee, Y.; Jang, S. K.; Kang, J.; Jeon, J.; Lee, C.; Lee, J. Y.; Kim, H.; Hwang, E.; Lee, S.; Cho, J. H. Dye-Sensitized MoS_2 Photodetector with Enhanced Spectral Photoresponse. *ACS Nano* **2014**, *8*, 8285–8291.

(2) Shastry, T. A.; Balla, I.; Bergeron, H.; Amsterdam, S. H.; Marks, T. J.; Hersam, M. C. Mutual Photoluminescence Quenching and Photovoltaic Effect in Large-Area Single-Layer MoS2-Polymer Heterojunctions. *ACS Nano* **2016**, *10*, 10573–10579.

(3) Liu, X.; Gu, J.; Ding, K.; Fan, D.; Hu, X.; Tseng, Y. W.; Lee, Y. H.; Menon, V.; Forrest, S. R. Photoresponse of an Organic Semiconductor/Two-Dimensional Transition Metal Dichalcogenide Heterojunction. *Nano Lett.* **2017**, *17*, 3176–3181.

(4) Huang, Y. L.; Zheng, Y. J.; Song, Z.; Chi, D.; Wee, A. T. S.; Quek, S. Y. The Organic–2D Transition Metal Dichalcogenide Heterointerface. *Chem. Soc. Rev.* **2018,** *47, 3241-3264*.

(5) Jariwala, D.; Howell, S. L.; Chen, K. S.; Kang, J.; Sangwan, V. K.; Filippone, S. A.; Turrisi, R.; Marks, T. J.; Lauhon, L. J.; Hersam, M. C. Hybrid, Gate-Tunable, van Der Waals p-n Heterojunctions from Pentacene and MoS2. *Nano Lett.* **2016**, *16*, 497–503.

(6) Petoukhoff, C. E.; Krishna, M. B. M.; Voiry, D.; Bozkurt, I.; Deckoff-Jones, S.; Chhowalla, M.; O'Carroll, D. M.; Dani, K. M. Ultrafast Charge Transfer and Enhanced Absorption in MoS2-Organic van Der Waals Heterojunctions Using Plasmonic Metasurfaces. *ACS Nano* **2016**, *10*, 9899–9908.

(7) Flatten, L. C.; Coles, D. M.; He, Z.; Lidzey, D. G.; Taylor, R. A.; Warner, J. H.; Smith, J. M. Electrically Tunable Organic-Inorganic Hybrid Polaritons with Monolayer WS2. *Nat. Commun.* **2017**, *8*, 1608.05274.

(8) Homan, S. B.; Sangwan, V. K.; Balla, I.; Bergeron, H.; Weiss, E. A.; Hersam, M. C. Ultrafast Exciton Dissociation and Long-Lived Charge Separation in a Photovoltaic Pentacene-MoS2van Der Waals Heterojunction. *Nano Lett.* **2017**, *17*, 164–169.

(9) Zheng, Y. J.; Huang, Y. L.; Chen, Y.; Zhao, W.; Eda, G.; Spataru, C. D.; Zhang, W.; Chang, Y. H.; Li, L. J.; Chi, D.; Quek, S. Y.; Wee, A. T. S. Heterointerface Screening Effects between Organic Monolayers and Monolayer Transition Metal Dichalcogenides. *ACS Nano* **2016**, *10*, 2476–2484.

(10) Reers, M.; Smith, T. W.; Chen, L. B. J-Aggregate Formation of a Carbocyanine as a Quantitative Fluorescent Indicator of Membrane Potential. *Biochemistry* **1991**, *30*, 4480–4486.

(11) Kuroda, S. I.; Ito, H.; Uchiyama, Y.; Mori, T.; Marumoto, K.; Hatta, I. J-Aggregate Formation of 6-Methyl-Merocyanine Dye in Mixed Langmuir-Blodgett Films with Arachidic Acid in a Wide Range of Mixing Ratio. *Japanese J. Appl. Physics, Part 1 Regul. Pap. Short Notes Rev. Pap.* **2002**, *41*, 6223–6227.

(12) Bradley, M. S.; Tischler, J. R.; Bulović, V. Layer-by-Layer J-Aggregate Thin Films with a Peak Absorption Constant of 106 Cm-1. *Adv. Mater.* **2005**, *17*, 1881–1886.

(13) Peyratout, C.; Daehne, L. Aggregation of Thiacyanine Derivatives on Polyelectrolytes. *Phys. Chem. Chem. Phys.* **2002**, *4*, 3032–3039.

(14) Lee, J.-H.; Min, C.-K.; Joo, T. Ultrafast Optical Dynamics of Excitons in J-Aggregates Optical Dynamics of Excitons in Aggregates of a Carbocyanine Dye Ultrafast Optical Dynamics of Excitons in J-Aggregates. *J. Chem. Phys. J. Chem. Phys. J. Chem. Phys. J Aggreg. J. Chem. Phys.* **2001**, *1141*.

(15) Walker, B. J.; Dorn, A.; Bulović, V.; Bawendi, M. G. Color-Selective Photocurrent Enhancement in Coupled J-Aggregate/Nanowires Formed in Solution. *Nano Lett.* **2011**, *11*, 2655–2659.

(16) Balandin, A. A.; Nika, D. L. Phononics in Low-Dimensional Materials. *Mater. Today* **2012**, *15*, 266–275.

(17) Mas-Ballesté, R.; Gómez-Navarro, C.; Gómez-Herrero, J.; Zamora, F. 2D Materials: To Graphene and Beyond. *Nanoscale* **2011**, *3*, 20–30.

(18) Fiori, G.; Bonaccorso, F.; Iannaccone, G.; Palacios, T.; Neumaier, D.; Seabaugh, A.; Banerjee, S. K.; Colombo, L. Electronics Based on Two-Dimensional Materials. *Nat. Nanotechnol.* **2014**, *9*, 768–779.

(19) Manzeli, S.; Ovchinnikov, D.; Pasquier, D.; Yazyev, O. V.; Kis, A. 2D Transition Metal Dichalcogenides. *Nat. Rev. Mater.* **2017**, *2*, 17033.

(20) Lopez-Sanchez, O.; Lembke, D.; Kayci, M.; Radenovic, A.; Kis, A. Ultrasensitive Photodetectors Based on Monolayer MoS 2. *Nat. Nanotechnol.* **2013**, *8*, 497–501.

(21) Yin, Z.; Li, H.; Li, H.; Jiang, L.; Shi, Y.; Sun, Y.; Lu, G.; Zhang, Q.; Chen, X.; Zhang, H. Single-Layer MoS2phototransistors. *ACS Nano* **2012**, *6*, 74–80.

(22) Zhang, W.; Chiu, M. H.; Chen, C. H.; Chen, W.; Li, L. J.; Wee, A. T. S. Role of Metal Contacts in High-Performance Phototransistors Based on WSe2monolayers. *ACS Nano* **2014**, *8*, 8653–8661.

(23) Choi, W.; Cho, M. Y.; Konar, A.; Lee, J. H.; Cha, G. B.; Hong, S. C.; Kim, S.; Kim, J.; Jena, D.; Joo, J.; Kim, S. High-Detectivity Multilayer MoS2 Phototransistors with Spectral Response from Ultraviolet to Infrared. *Adv. Mater.* **2012**, *24*, 5832–5836.

(24) Yin, Z.; Li, H.; Li, H.; Jiang, L.; Shi, Y.; Sun, Y.; Lu, G.; Zhang, Q.; Chen, X.; Zhang, H. Single-Layer MoS2 Phototransistors. *ACS Nano* **2011**, *6*, 74–80.

(25) Lopez-Sanchez, O.; Dumcenco, D. O.; Charbon, E.; Kis, A. Avalanche Photodiodes Based on MoS2 / Si Heterojunctions. *ArXiv e-prints* **2014**.

(26) Tsai, D. S.; Liu, K. K.; Lien, D. H.; Tsai, M. L.; Kang, C. F.; Lin, C. A.; Li, L. J.; He, J. H. Few-Layer MoS2 with High Broadband Photogain and Fast Optical Switching for Use in Harsh Environments. *ACS Nano* **2013**, *7*, 3905–3911.

(27) Zhong, X.; Zhou, W.; Peng, Y.; Zhou, Y.; Zhou, F.; Yin, Y.; Tang, D. Multi-Layered MoS 2 Phototransistors as High Performance Photovoltaic Cells and Self-Powered Photodetectors. *RSC Adv.* **2015**, *5*, 45239–45248.

(28) Bie, Y.-Q.; Grosso, G.; Heuck, M.; Furchi, M. M.; Cao, Y.; Zheng, J.; Bunandar, D.; Navarro-Moratalla, E.; Zhou, L.; Efetov, D. K.; Taniguchi, T.; Watanabe, K.; Kong, J.; Englund, D.; Jarillo-Herrero, P. A MoTe2-Based Light-Emitting Diode and Photodetector for Silicon Photonic Integrated Circuits. *Nat. Nanotechnol.* **2017**, 1–19.

(29) Lopez-Sanchez, O.; Lembke, D.; Kayci, M.; Radenovic, A.; Kis, A. Ultrasensitive Photodetectors Based on Monolayer MoS2. *Nat. Nanotechnol.* **2013**, *8*, 497–501.

(30) Radisavljevic, B.; Radenovic, A.; Brivio, J.; Giacometti, V.; Kis, A. Single-Layer MoS2 Transistors. *Nat. Nanotechnol.* **2011**, *6*, 147–150.

(31) Lembke, D.; Kis, A. Breakdown of High-Performance Monolayer MoS2 Transistors. *ACS Nano* **2012**, *6*, 10070–10075.

(32) Tang, H.-L.; Chiu, M.-H.; Tseng, C.-C.; Yang, S.-H.; Hou, K.-J.; Wei, S.-Y.; Huang, J.-K.; Lin, Y.-F.; Lien, C.-H.; Li, L.-J. Multilayer Graphene-WSe $_2$ Heterostructures for WSe $_2$ Transistors. *ACS Nano* **2017**, *11, 12817-12823*.

(33) Lee, C.-H.; Lee, G.-H.; van der Zande, A. M.; Chen, W.; Li, Y.; Han, M.; Cui, X.; Arefe, G.; Nuckolls, C.; Heinz, T. F.; Guo, J.; Hone, J.; Kim, P. Atomically Thin p–n Junctions with van Der Waals Heterointerfaces. *Nat. Nanotechnol.* **2014**, *9*, 676–681.

(34) Fontana, M.; Deppe, T.; Boyd, A. K.; Rinzan, M.; Liu, A. Y.; Paranjape, M.; Barbara, P. Electron-Hole Transport and Photovoltaic Effect in Gated MoS2schottky Junctions. *Sci. Rep.* **2013**, *3*, 8–13.

(35) Wang, H.; Yu, L.; Lee, Y.-H.; Shi, Y.; Hsu, A.; Chin, M. L.; Li, L.-J.; Dubey, M.; Kong, J.; Palacios, T. Integrated Circuits Based on Bilayer MoS2 Transistors. *Nano Lett.* **2012**, *12*, 4674–4680.

(36) Roy, T.; Tosun, M.; Cao, X.; Fang, H.; Lien, D.-H.; Zhao, P.; Chen, Y.-Z.; Chueh, Y.-L.; Guo, J.; Javey, A. Dual-Gated MoS 2 /WSe 2 van Der Waals Tunnel Diodes and Transistors. *ACS Nano* **2015**, *9*, 2071–2079.

(37) Ross, J. S.; Klement, P.; Jones, A. M.; Ghimire, N. J.; Yan, J.; Mandrus, D. G.; Taniguchi, T.; Watanabe, K.; Kitamura, K.; Yao, W.; Cobden, D. H.; Xu, X. Electrically Tunable Excitonic Light-Emitting Diodes Based on Monolayer WSe2 p–n Junctions. *Nat. Nanotechnol.* **2014**, *9*, 268–272.

(38) Palacios-Berraquero, C.; Barbone, M.; Kara, D. M.; Chen, X.; Goykhman, I.; Yoon, D.; Ott, A. K.; Beitner, J.; Watanabe, K.; Taniguchi, T.; Ferrari, A. C.; Atature, M. Atomically Thin Quantum Light-Emitting Diodes. *Nat. Commun.* **2016**, *7*, 1–6.

(39) Baugher, B. W. H.; Churchill, H. O. H.; Yang, Y.; Jarillo-Herrero, P. Optoelectronic Devices Based on Electrically Tunable p–n Diodes in a Monolayer Dichalcogenide. *Nat. Nanotechnol.* **2014**, *9*, 262–267.

(40) Tsai, M. L.; Su, S. H.; Chang, J. K.; Tsai, D. S.; Chen, C. H.; Wu, C. I.; Li, L. J.; Chen, L. J.; He, J. H. Monolayer MoS2 Heterojunction Solar Cells. *ACS Nano* **2014**, *8*, 8317–8322.

(41) Furchi, M. M.; Pospischil, A.; Libisch, F.; Burgdörfer, J.; Mueller, T. Photovoltaic Effect in an Electrically Tunable Van Der Waals Heterojunction. *Nano Lett.* **2014**, *14*, 4785–4791.

(42) Fontana, M.; Deppe, T.; Boyd, A. K.; Rinzan, M.; Liu, A. Y.; Paranjape, M.; Barbara, P. Electron-Hole Transport and Photovoltaic Effect in Gated MoS2 Schottky Junctions. *Sci. Rep.* **2013**, *3*, 8–13.

(43) Castellanos-Gomez, A.; Quereda, J.; van der Meulen, H. P.; Agraït, N.; Rubio-Bollinger, G. Spatially Resolved Optical Absorption Spectroscopy of Single- and Few-Layer MoS $_2$ by Hyperspectral Imaging. *Nanotechnology* **2016**, *27*, 115705.

(44) Prins, F.; Goodman, A. J.; Tisdale, W. A. Reduced Dielectric Screening and Enhanced Energy Transfer in Single- and Few-Layer MoS2. *Nano Lett.* **2014**, *14*, 6087–6091.

(45) Chernikov, A.; Berkelbach, T. C.; Hill, H. M.; Rigosi, A.; Li, Y.; Aslan, O. B.; Reichman, D. R.; Hybertsen, M. S.; Heinz, T. F. Exciton Binding Energy and Nonhydrogenic Rydberg Series in Monolayer WS2. *Phys. Rev. Lett.* **2014**, *113*, 076802.

(46) Clapp, A. R.; Medintz, I. L.; Mattoussi, H. Förster Resonance Energy Transfer Investigations Using Quantum-Dot Fluorophores. *Eur. J. Chem. Phys. Phys. Chem.* **2006**, *7*, 47–57.

(47) Medintz, I. L.; Mattoussi, H. Quantum Dot-Based Resonance Energy Transfer and Its Growing Application in Biology. *Phys. Chem. Chem. Phys.* **2009**, *11*, 17–45.

(48) Shirasaki, Y.; Anikeeva, P. O.; Tischler, J. R.; Scott Bradley, M.; Bulović, V. Efficient F??Rster Energy Transfer from Phosphorescent Organic Molecules to J-Aggregate Thin Films. *Chem. Phys. Lett.* **2010**, *485*, 243–246.

(49) Blum, C.; Zijlstra, N.; Lagendijk, A.; Wubs, M.; Mosk, A. P.; Subramaniam, V.; Vos, W. L. Nanophotonic Control of the Förster Resonance Energy Transfer Efficiency. *Phys. Rev. Lett.* **2012**, *109*, 1–5.

(50) Mak, K. F.; Lee, C.; Hone, J.; Shan, J.; Heinz, T. F. Atomically Thin MoS2: A New Direct-Gap Semiconductor. *Phys. Rev. Lett.* **2010**, *105*.

(51) Zhou, D.; Piper, J. D.; Abell, C.; Klenerman, D.; Kang, D.-J.; Ying, L. Fluorescence Resonance Energy Transfer between a Quantum Dot Donor and a Dye Acceptor Attached to DNA. *Chem. Commun. (Camb).* **2005**, 4807–4809.

(52) Murphy, C. B.; Zhang, Y.; Troxler, T.; Ferry, V.; Martin, J. J.; Jones, W. E. Probing Förster and Dexter Energy-Transfer Mechanisms in Fluorescent Conjugated Polymer Chemosensors. *J. Phys. Chem. B* **2004**, *108*, 1537–1543.

(53) Mak, K. F.; He, K.; Lee, C.; Lee, G. H.; Hone, J.; Heinz, T. F.; Shan, J. Tightly Bound Trions in Monolayer MoS 2. *Nat. Mater.* **2013**, *12*, 207–211.

(54) Li, Z.; Ye, R.; Feng, R.; Kang, Y.; Zhu, X.; Tour, J. M.; Fang, Z. Graphene Quantum Dots Doping of MoS $_2$ Monolayers. *Adv. Mater.* **2015**, *27*, 5235–5240.

(55) Matsukura, Y.; Uchiyama, Y.; Yamashita, H.; Nishino, H.; Fujii, T. Responsivity-Dark Current Relationship of Quantum Dot Infrared Photodetectors (QDIPs). *Infrared Phys. Technol.* **2009**, *52*, 257–259.

(56) Furchi, M. M.; Polyushkin, D. K.; Pospischil, A.; Mueller, T. Mechanisms of Photoconductivity in Atomically Thin MoS2. *Nano Lett.* **2014**, *14*, 6165–6170.

(57) Dean, C. R.; Young, A. F.; Meric, I.; Lee, C.; Wang, L.; Sorgenfrei, S.; Watanabe, K.; Taniguchi, T.; Kim, P.; Shepard, K. L.; Hone, J. Boron Nitride Substrates for High-Quality Graphene Electronics. *Nat. Nanotechnol.* **2010**, *5*, 722–726.

(58) Henck, H.; Pierucci, D.; Fugallo, G.; Avila, J.; Cassabois, G.; Dappe, Y. J.; Silly, M. G.; Chen, C.; Gil, B.; Gatti, M.; Sottile, F.; Sirotti, F.; Asensio, M. C.; Ouerghi, A. Direct Observation of the Band Structure in Bulk Hexagonal Boron Nitride. *Phys. Rev. B* **2017**, *95*, 1–6.

(59) Moll, J.; Daehne, S.; Durrant, J. R.; Wiersma, D. A. Optical Dynamics of Excitons in J Aggregates of a Carbocyanine Dye. *J. Chem. Phys.* **1995**, *102*, 6362–6370.

(60) Walczewska-Szewc, K.; Corry, B. Accounting for Dye Diffusion and Orientation When Relating FRET Measurements to Distances: Three Simple Computational Methods. *Phys. Chem. Chem. Phys.* **2014**, *16*, 12317–12326.

(61) Dale, R. E.; Eisinger, J.; Blumberg, W. E. The Orientation Freedom of Molecular Probes. *Biophys. J.*, 1979, *26*, 161–93.

(62) Steinberg, I. Z. Long-Range Nonradiative Transfer of Electronic Excitation Energy in Proteins and Polypeptides. *Annu. Rev. Biochem.* **1971**, *40*, 83–114.

(63) Ploetz, E.; Lerner, E.; Husada, F.; Roelfs, M.; Chung, S.; Hohlbein, J.; Weiss, S.; Cordes, T. Förster Resonance Energy Transfer and Protein-Induced Fluorescence Enhancement as Synergetic Multi-Scale Molecular Rulers. *Sci. Rep.* **2016**, *6*, 1–18.

(64) Stöferle, T.; Mahrt, R. F. Energy Transfer in Hybrid Organic/Inorganic Nanocomposites. **2009**, 73930C.

Chapter 3 Energy Transport of Hybrid Charge Transfer Excitons

3.1 Introduction

Hybrid systems constructed by interfacing organic and inorganic semiconductors provide a platform to combine unique photophysical, electronic and mechanical properties that do not normally coexist in the individual material systems.[1–5] For instance, organic semiconductors are widely recognized for their strong absorption but relatively poor charge mobility. On the other hand, inorganic semiconductors are known for their remarkable charge transport properties but lack the strong photophysical properties commonly associated with organics. Recently, molecular semiconductors integrated with 2D transition metal dichalcogenides (TMDs) to form hybrid heterostructures have been reported.[6–9] TMD monolayers are ideal materials to form such hybrid heterostructures due to their low dimensionality, which enables easy access to unique properties absent in its bulk form, and its van der Waals (vdW) nature without dangling bonds on the 2D surface. With their atomic layers weakly bound by van der Waals forces, vdW solids do not suffer from elemental diffusion at the interface or lattice mismatch between different materials, thus offering enormous choice of combinations. As a result, organic-TMD hybrid heterostructures have recently gathered a lot of interest, especially in understanding the charge generation and separation processes.[10–13]

The charge transfer process has been found to be extremely fast (on the order of a few pico-seconds or less)[1,11,13–15] across type-II hybrid organic-TMD heterointerfaces. Due to the interfacial

Coulomb potential, the spatially separated electron and hole form a tightly-bound excitons with binding energies of hundreds of millielectron volts.[3,14] While such interlayer excitons, also referred to as hybrid charge transfer excitons (HCTEs), have been reported across hybrid organic-TMD heterostructures before, the energy transport associated with HCTE states combining Frenkel excitons in organics and Wannier-Mott excitons in inorganics remains an underexplored territory of research. This is especially true in the time regime immediately following the formation of HCTE states, where ultrafast transport has been observed.[14]

Unraveling the unknown physics associated with such ultrafast transport of HCTE is imperative to the development of a material platform for next generation energy conversion and optoelectronic devices with superior and targeted performance. In this work, we study the transport of HCTEs in the sub-nanosecond time regime following optical excitation at a hybrid organic-inorganic heterojunction, featuring single layer molybdenum disulfide (MoS_2) and a highly absorbing j-aggregate thin film of organic dye TDBC (5,6-dichloro-2[3-[5,6-dichloro-1-ethyl-3-(3-sulfopropyl)-2(3H)-benzimidazolidene]-1-propenyl]-1-ethyl-3-(3-sulfopropyl) benzimidazolium hydroxide), to understand the contribution behind the observed ultrafast exciton transport. Our findings suggest the formation of fast-moving *hot* HCTE states as the primary reason behind the ultrafast transport and phonon bottleneck causing the slow thermalization of those *hot* HCTE states.

Figure 3.1 shows a schematic illustration of the hybrid 2D interface. J-aggregates are formed from fluorescent molecules and can be identified by their narrow and intense absorption spectrum.[16] The absorption spectrum of TDBC shifts from a broad monomer band centered at around 515 nm to a strong and narrow j-band peaked at 592 nm. We use monolayer MoS_2 as the inorganic material due to its atomic scale two-dimensionality and the excellent spectral overlap

with TDBC j-aggregate's emission spectrum. The narrow and intense emission spectrum of the j-aggregate molecules closely overlaps with the absorption peak of monolayer MoS_2 at 595 nm, resulting in efficient Förster resonance energy transfer (FRET) across the hybrid interface (refer Figure 2.1b).[17] Such efficient energy transport enables the experiment to be performed at much lower excitation densities (avoiding sample damage). The heterojunction was formed by mechanically exfoliating a MoS_2 monolayer on a cover glass, followed by a layer-by-layer deposition of a thin layer (~5 nm) of j-aggregate.[18] The details of the fabrication procedure can be found in the methods section of Chapter 2.

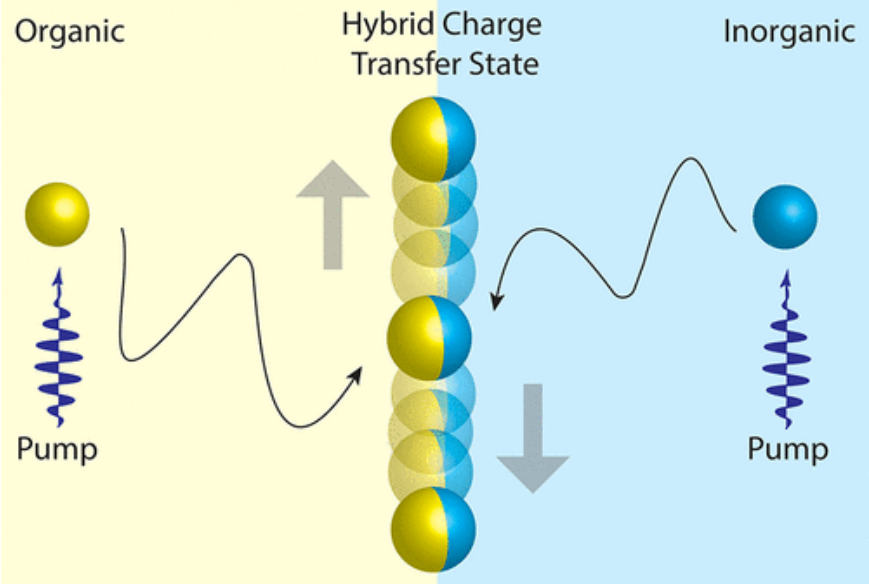

Figure 3.1 Hybrid charge transfer excitons (HCTEs) in hybrid TDBC j-aggregate and MoS_2 2D interface. The HCTEs consist of electrons from MoS_2 conduction band and holes from j-aggregate's HOMO.

3.2 Results and discussion

3.2.1 PL spectra of HCTEs

Figure 3.2 shows the PL spectra of the hybrid structure. Upon deposition of the j-aggregate film, a new peak at around 760 nm (1.63 eV), corresponding to the HCTE state was observed in the heterojunction's PL spectrum. The inset shows the type II energy band alignment of the hybrid heterojunction forming the HCTE. The offset (0.28 eV) between MoS_2 valence band and j-aggregate highest occupied molecular orbital (HOMO) is greater than MoS_2 *A* exciton binding energy (0.27 eV), thus providing the driving force for *A* exciton dissociation and hole transfer. A similar mechanism applies to j-aggregate electron transfer upon photoexcitation. The charge transfer is confirmed by their respective PL quenching as seen in Figure 3.3. We note that the j-aggregate PL spectrum remains unchanged in the presence/absence of MoS_2 except for the intensity drop due to charge transfer. Figure 3.4 shows the spectrally-integrated PL intensity map of HCTE emission under 532 nm CW photoexcitation. The emission of the HCTE state is observed across the entire MoS_2 flake as confirmed by the inset micrograph image of monolayer MoS_2 on cover glass.

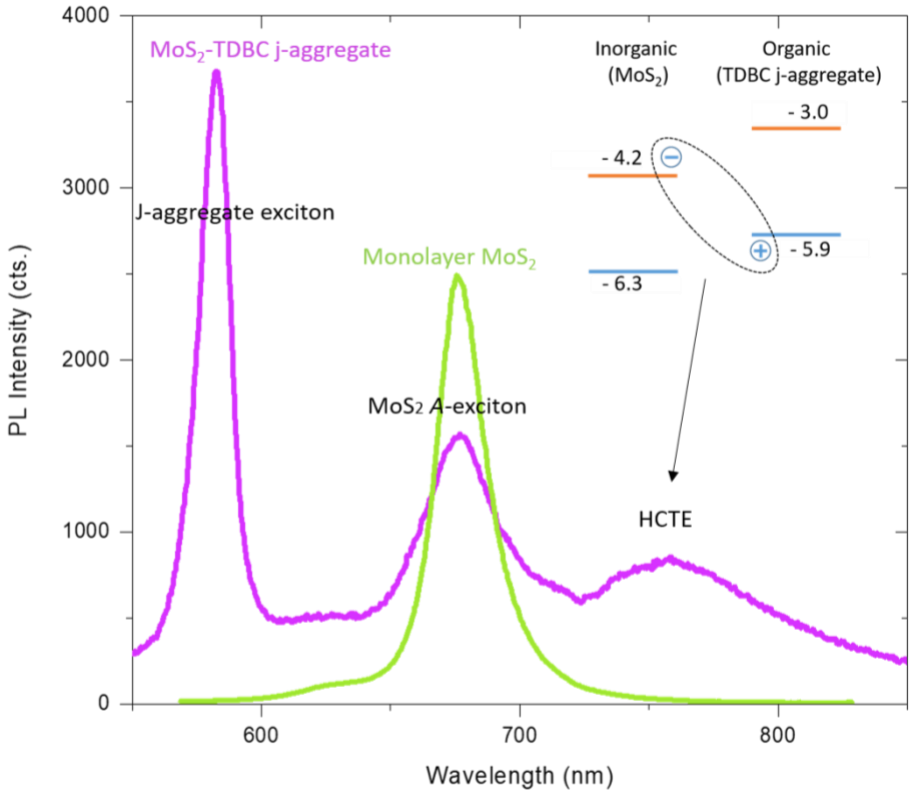

Figure 3.2 PL spectra of monolayer MoS_2 (green) and hybrid MoS_2/j-aggregate heterojunction (purple) with a 532 nm CW laser excitation. MoS_2 *A* exciton at 670 nm and TDBC j-aggregate emission at 590 nm are identified in the hybrid sample. The third resonance at 760 nm is the HCTE formed by charge transfer across the hetero-interface with type II energy band alignment, as shown in the inset. Due to favorable energy levels, interfacial transfer of electrons to MoS_2 and holes to j-aggregate occurs within a few pico-seconds after excitation.

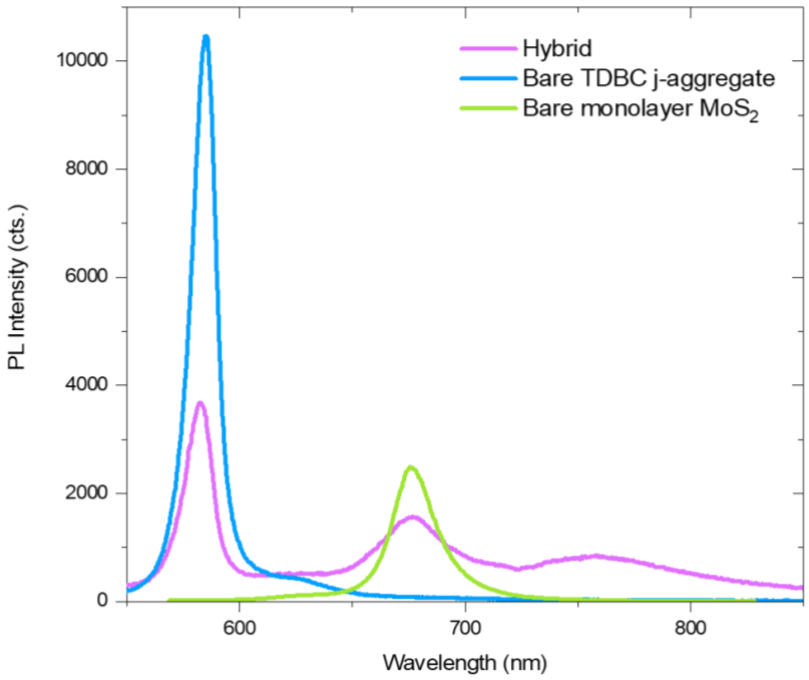

Figure 3.3 PL emission spectra from TDBC j-aggregate, monolayer MoS_2, and monolayer MoS_2/j-aggregate heterostructure. PL quenching is observed for both materials in the hybrid structure region.

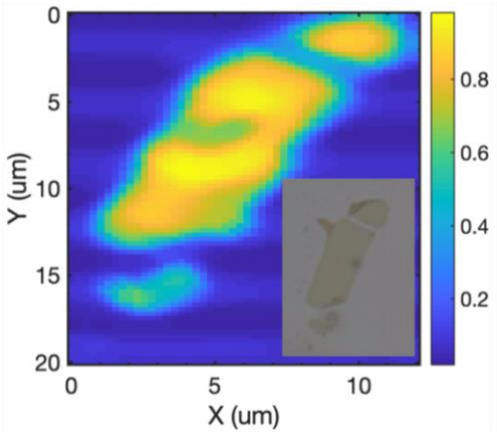

Figure 3.4 PL peak intensity map of the hybrid MoS_2 and j-aggregate at the HCTE wavelength range. The HCTE emission is observed throughout the entire MoS_2 flake as confirmed by the inset optical image of the monolayer.

3.2.2 Formation of HCTEs

We estimate the formation efficiency of HCTEs by adopting an indirect approach based on aggregate time-resolved photoluminescence (TRPL) measurements. The TRPL dynamics (measured using time-correlated single photon counting (TCSPC) with a pulsed 405 nm laser) of j-aggregate's singlet excitons (595 nm), MoS_2 *A* excitons (670 nm), and HCTEs (760 nm) are shown in Figure 3.5a. Due to the its spatially indirect nature, the HCTE exhibits an overall lifetime of 0.28 ns that is longer than that of j-aggregate and MoS_2's *A* exciton's lifetime. Inset of Figure 3.5a shows that the HCTEs are formed 40 ps after the laser excitation (the maximum value of TDBC j-aggregate's TRPL intensity is referenced as t = 0 throughout the manuscript). A similar delay was measured across several samples with an average formation delay of 36 ± 6.8 ps for the HCTEs, as shown in Figure 3.6.

Next, we monitor the excitation density dependent TRPL of the HCTE as shown in Figure 3.5b. The initial HCTE population decay rate increases with increasing excitation density, as emphasized in the inset plot, due to increased non-radiative contribution from Auger recombination (exciton-exciton annihilation). Such time evolution of the HCTE population can be modeled with the following rate equation:[19,20]

$$\frac{\partial n}{\partial t} = -\frac{(n)}{\tau} - R_A(n)^2 \tag{3.1}$$

where n is the HCTE density, τ is the exciton lifetime, and R_A is the Auger coefficient. We note that the TRPL data shown in Figure 3.5a and 3.5b were obtained by summing up the PL intensities of all the spatially diffused excitons (integrating the corresponding temporally and spatially resolved PL intensity maps, similar to the one shown in Figure 3.8, over the spatial coordinate), eliminating the need to include the diffusion term in equation (3.1). We define the HCTE density

as $n \equiv \alpha n_0$, where n_0 and n are the density of absorbed photons and corresponding HCTEs respectively, and α is the formation efficiency of HCTEs. In addition, the steady state PL intensity of excitons in the presence of Auger recombination can be modelled as:[20]

$$I_{PL}(n) \propto \frac{\ln(1+(n)R_A\tau)}{R_A}\frac{1}{\tau} \tag{3.2}$$

We fit the experimental data with equations (3.1) and (3.2) simultaneously and extract the HCTE formation efficiency of 40% and an Auger coefficient of 0.005 cm^2/s. The fitting curves obtained from the solution to equation (3.1) given by

$$n(t) = \frac{n_0}{e^{\left[\left(\frac{t}{\tau}\right)(1+n_0R_A)\right]-n_0R_A\tau}} \tag{3.3}$$

and equation (3.1) and (3.2) are shown as solid lines in Figure 3.7a and 3.7b, respectively. It is worth noting that the Auger recombination rate of HCTEs at the current hybrid interface is an order of magnitude lower than the rate of MoS_2 *A* exciton. The technique outlined here demonstrates a simpler alternative to the complex pump-probe techniques typically used to estimate exciton formation efficiencies.

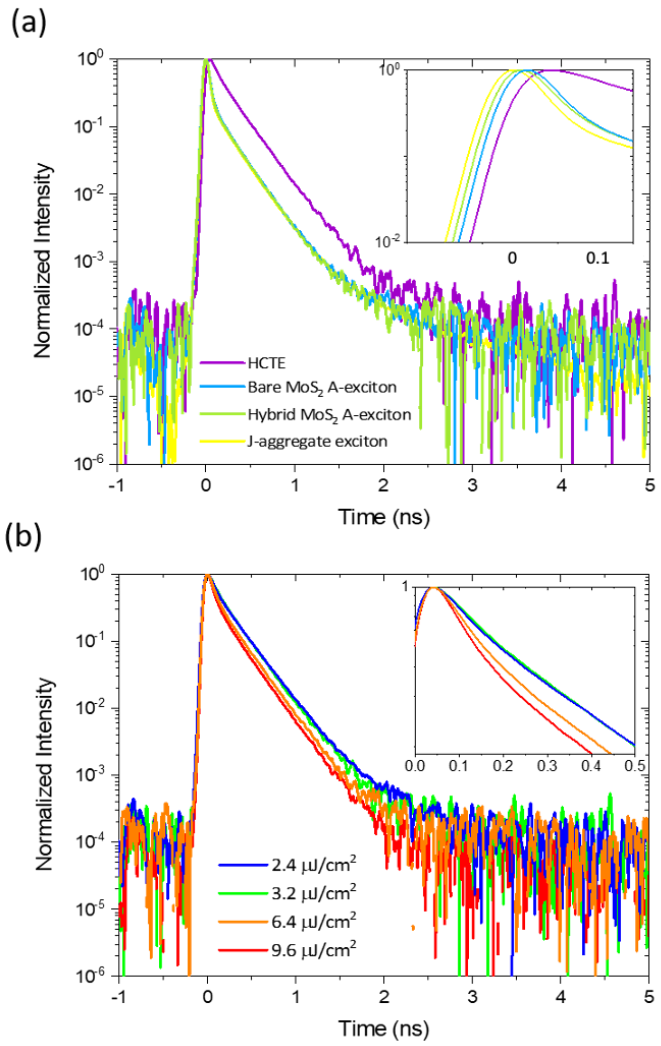

Figure 3.5 Lifetime of HCTEs. (a) Time-resolved PL dynamics of j-aggregate exciton, MoS_2 *A* exciton in bare monolayer and in the hybrid film, and HCTE. HCTEs decay much more slowly than *A* excitons due to their interlayer formation. The inset highlights the significant formation delay of HCTE of 40 ps as compared to j-aggregate excitons. (b) Time-resolved PL measurements of HCTEs at different excitation densities. The exciton density decay rate increases as the excitation power density increases, which can be attributed to Auger recombination.

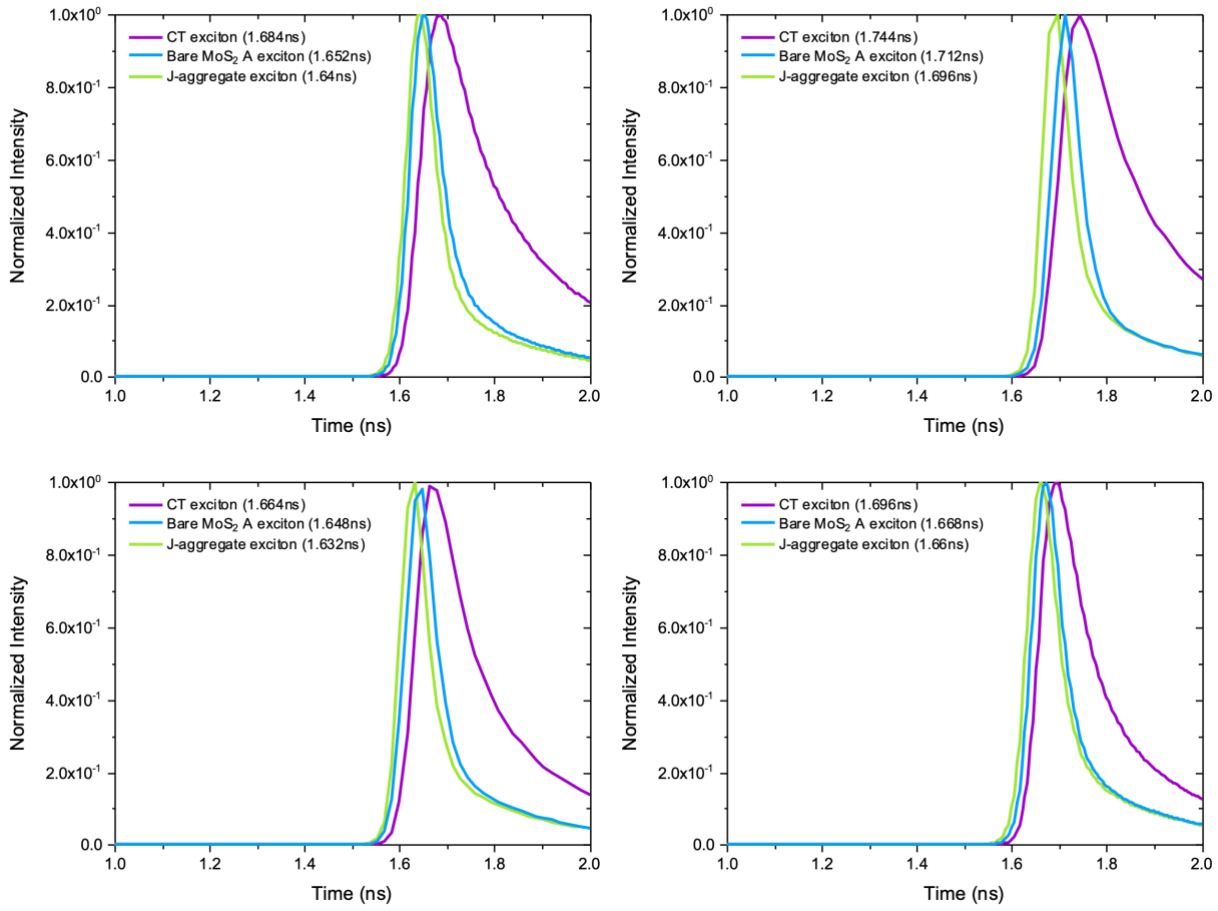

Figure 3.6 CT exciton TRPL delay times for 4 samples that show a range between 20ps and 48ps. The delay time can be approximated as CT exciton formation time since the formation of j-aggregate excitons is within a picosecond.

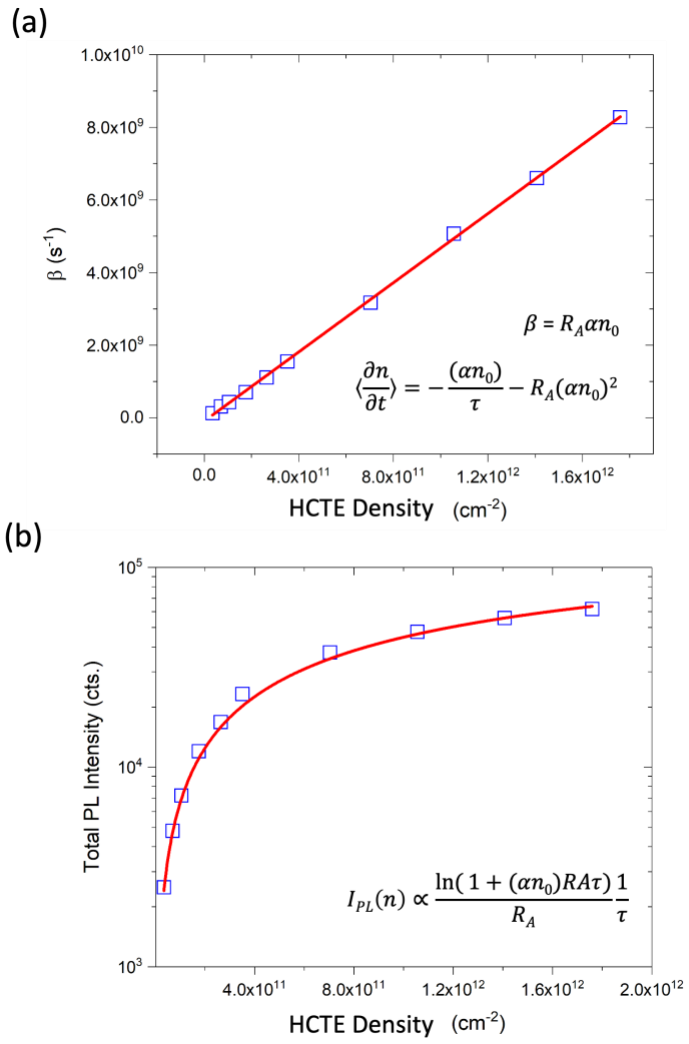

Figure 3.7 Formation efficiency of HCTEs. HCTE lifetime fitting with (c) exciton recombination rate and (d) PL yield. Both equations are functions of the Auger constant R_A, exciton lifetime τ, and HCTE density n (αn_o). Note that n_o is the density of all absorbed photons on the hybrid sample, and α is the formation ratio of HCTE. By fitting our data with the intensity and lifetime models, we find a single α that can satisfy both equations with identical Auger constant R_A. HCTE formation efficiency of 40% and Auger coefficient of 0.005 cm^2/s were estimated.

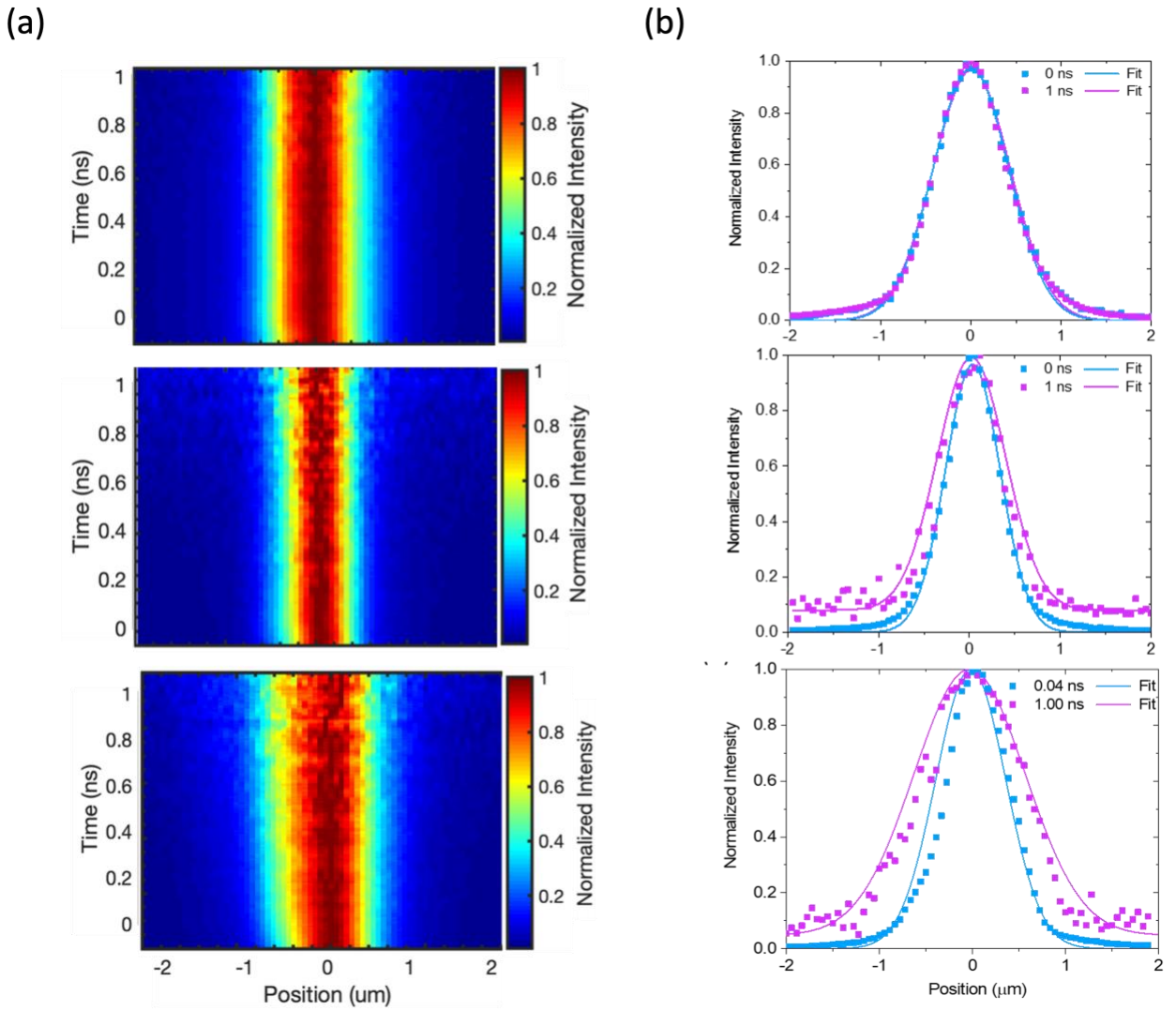

Figure 3.8 Visualized transport of j-aggregate exciton, MoS_2 *A* exciton, and HCTE. (a) Temporally and spatially resolved exciton density map of j-aggregate exciton (top), MoS_2 *A* exciton (middle), and HCTE (bottom). The data were obtained by TCSPC and a 405 nm pulsed laser. Highly diffusive HCTEs are observed compared to non-mobile j-aggregate and MoS_2 *A* excitons. (b) Normalized exciton population profiles extracted from (a) at 0 ns (blue) and 1 ns (purple), respectively. At 0 ns, j-aggregate has the largest spot (FWHM of 0.85μm) while MoS_2 *A* exciton has the smallest (FWHM of 0.6μm).

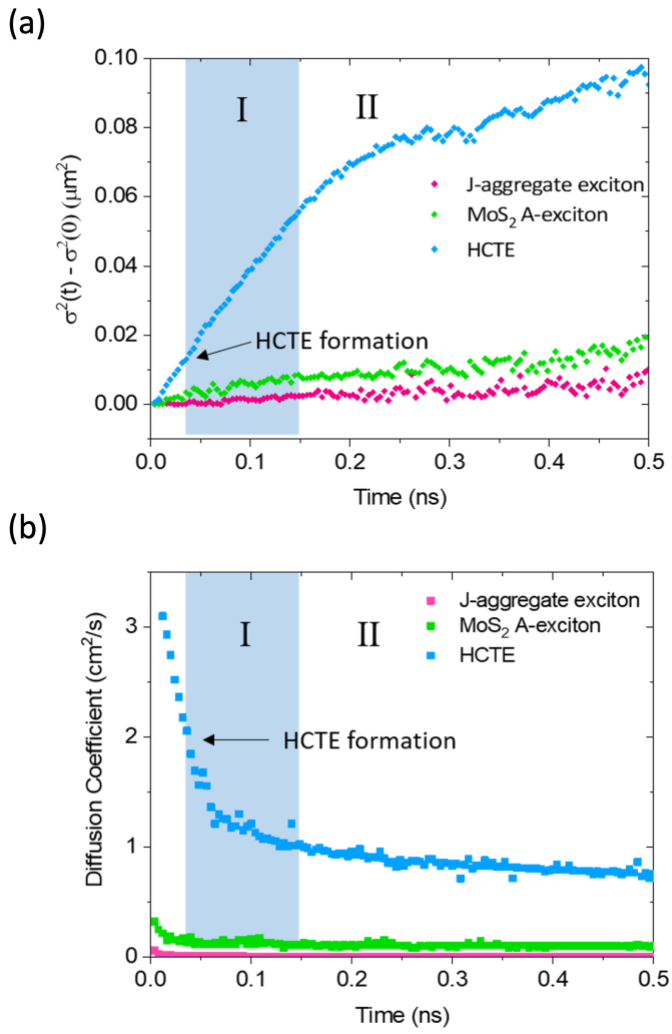

Figure 3.9 Transport properties of j-aggregate exciton, MoS_2 A exciton, and HCTE. (a) MSD change of exciton density as a function of time. HCTEs diffuse faster within region I, indicating contributions from both hot carriers and Auger scattering broadening. (b) Time dependent diffusion coefficients. HCTEs diffuse an order of magnitude faster than MoS_2 *A* excitons. J-aggregate excitons are immobile.

3.2.3 Transport of HCTEs

Figure 3.8a shows the temporally and spatially resolved PL intensity map of HCTEs obtained using a diffusion imaging microscope reported in our earlier work[21] (excitation fluence of 3.2 μJ/cm^2 and a corresponding HCTE density of 3.52×10^{11} cm^{-2} using a pulsed 405 nm laser). Figure 3.8b plots the exciton distribution at different times emphasizing the broadening of the initial distribution. The evolution of the exciton population's spatial profile created by a laser with a Gaussian intensity profile can be described with the equation:[19]

$$n(x,t) = \frac{n_i}{\sqrt{4\sigma Dt}} exp\left(\frac{x^2}{2\sigma^2(0)+4Dt}\right) \quad (3.4)$$

where D is the diffusion coefficient, n_i is the initial total exciton density, t denotes the time, and $2\sigma(t)$ is the FWHM of the Gaussian exciton density profile. Using this result, the time-dependent mean-squared displacement (MSD) change of the exciton density (defined as $[\Delta x^2(t)] \equiv \sigma^2(t) - \sigma^2(0) = 2Dt$) can be calculated and the diffusion coefficient can be extracted. However, in a 2D semiconductor system with intrinsic defects and impurities, the diffusion process is not linear with time and the MSD change is better described by the power law $[\Delta x^2(t)] = Gt^\beta$, where G and β are the transport factor and anomalous coefficient,[22] respectively. The time-dependent diffusion coefficient is then defined as $D(t) = (\alpha G t^{\beta-1})/2$.

Figure 3.9a and 3.9b plot the MSD of the exciton density distribution and the extracted time dependent diffusivity as a function of time respectively for j-aggregate excitons, MoS_2 *A* excitons, and HCTEs. Initially, HCTE are highly mobile when compared to j-aggregate and MoS_2 *A* excitons (we note, that while j-aggregate excitons do not diffuse much, the initial exciton density distribution is largest (0.85 μm with 0.5 μm excitation spot) for j-aggregates, as seen in Figure 3.8. This is consistent with reported ultrafast diffusion of excitons in j-aggregates in short time scales

that are not captured in the current experiments).[23] We notice a non-linear evolution of MSD for HCTEs, characterized by two regimes (after the formation of HCTE states) (I) 40-150 ps (110 ps) of highly mobile HCTEs, and (II) slow moving HCTE states where diffusivity appears to asymptote to 0.77 ± 0.21 cm^2/s, a value that is higher than MoS_2 *A* excitons' diffusivity, indicating the intrinsically more diffusive nature of HCTEs in the TMD/organic system. The observed nonlinearity in MSD could be explained by possible contributions from Auger broadening and/or *hot* exciton transport.[24] Auger broadening is caused by exciton-exciton annihilation.[25] Due to higher exciton density at the center of the excitation beam, the exciton-exciton annihilation rate is also higher, causing the PL intensity at the center to drop faster than at the surrounding area. As a result, the Gaussian exciton density profile appears to broaden faster. We estimate such contribution from the measured Auger coefficient and find that it is small below 3.52×10^{11} cm^{-2} (refer to Figure 3.10). Nevertheless, minor contributions from Auger exists and cannot be easily subtracted from the data.

On the other hand, since high energy photons (3.1 eV, much higher than MoS_2's optical band gap) are used to excite the sample, high energy excitons can be formed after interacting with phonons (in organics as well as in inorganics). These excitons with excess energy can dissociate into free *hot* carriers or form *hot* HCTEs (excitons with high kinetic energy). Since we know the HCTEs are formed in about 40 ps after photoexcitation as shown in Figure 3.5a, we attribute the transport observed in regime I to be dominated by *hot* HCTE states. The higher diffusivity observed prior to regime I could possibly be due to *hot* carriers. However, we ignore the analysis in the short time regime as it is very close to the limits of the TCSPC technique. Further dissociation of HCTEs into free carriers, following its formation is also possible but unlikely due to high binding energy of HCTE (~90 meV based on energy level calculations and PL emission).

However, in this case, we would expect the diffusivity to be similar to that observed prior to regime I and relaxation time to be much shorter, further justifying that the observed transport is from HCTEs.

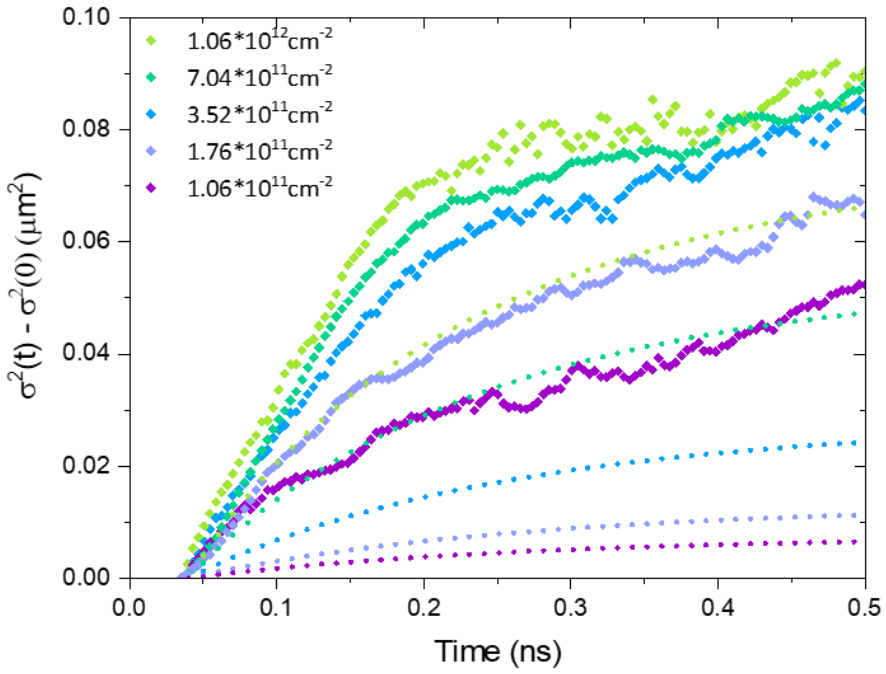

Figure 3.10 Estimated Exciton-exciton annihilation contribution (dotted curves) for each HCTE density. The process is solely dependent on the exciton densities. We note that the effect of Auger broadening is overestimated since contribution of diffusing excitons is completely neglected.

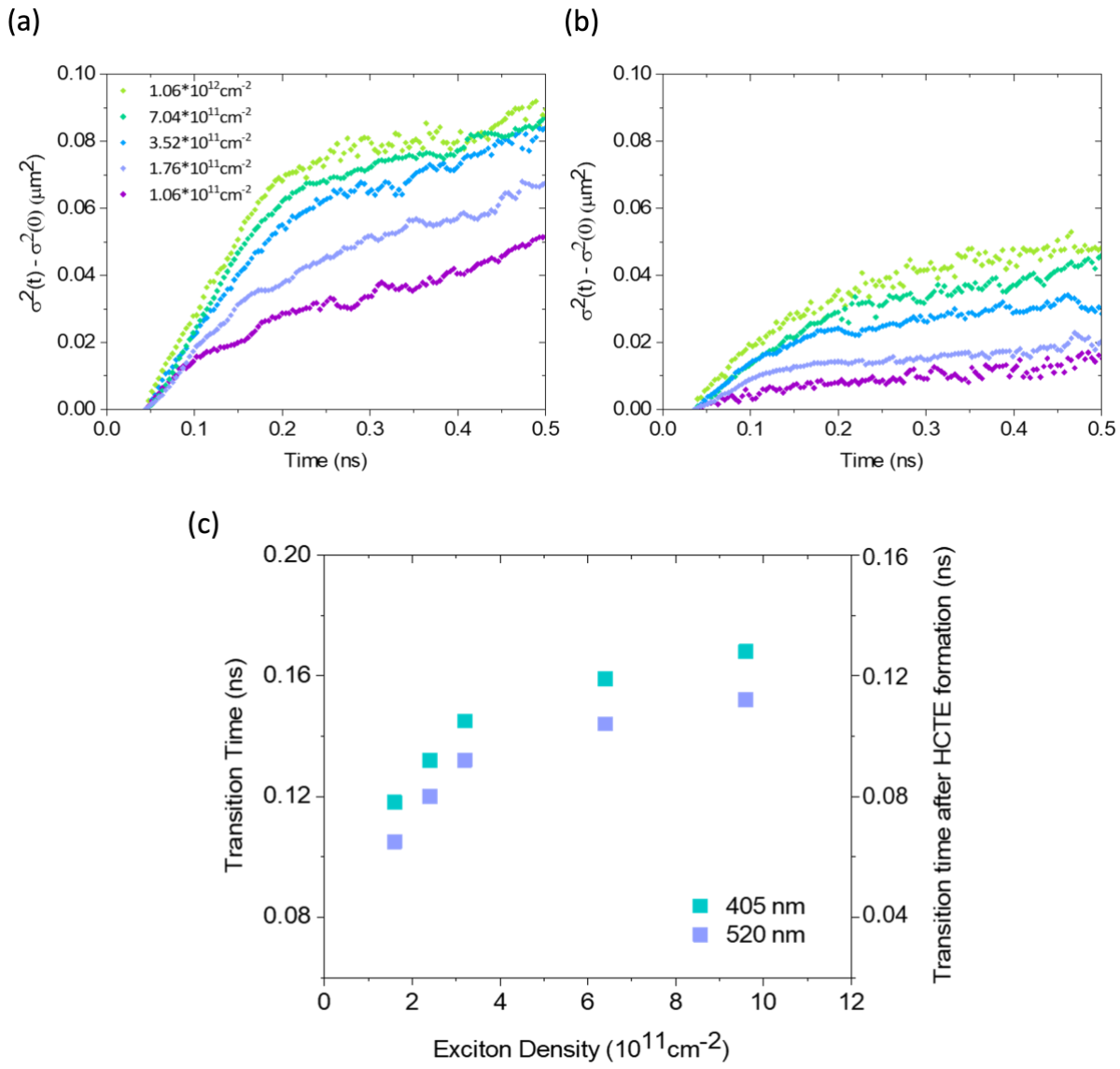

Figure 3.11 Highly mobile hot HCTEs. Power density dependent MSD of HCTEs as a function of time with (a) 405 nm pulsed and (b) 520 nm pulsed excitations. The curves with the same colors in (a) and (b) correspond to the same exciton densities, and thus same Auger recombination rates. Despite having same exciton-exciton annihilation rate, MSD of HCTEs pumped with 405 nm laser is still larger than that pumped with 520 nm laser in region I, confirming the contribution from hot HCTEs. (c) Hot exciton relaxation times (transition time) versus excitation fluences. We observe evidence of saturation above exciton densities of 4×10^{11} cm^{-2}.

3.2.4 Excitation energy and density dependent HCTE transport

We also studied the effect of excitation photon energy and density on transport. The fluence dependent MSD of HCTE as a function of time using 3.06 eV (405nm) and 2.38 eV (520 nm) pulsed lasers are shown in Figure 3.11a and 3.11b. The curves with the same color from Figure 3.11a and 3.11b correspond to the same HCTE density. This condition is achieved by exciting the samples with fluences that result in identical rates of emission of HCTE photons in both cases. The inset numbers in Figure 3.11a are the HCTE densities. Furthermore, the ratio of average power of the 520 nm to 405 nm lasers remained constant (2.7 ± 0.12) throughout the measurements (refer Figure 3.12), confirming that the contribution from Auger broadening remained identical for each excitation fluence as the Auger scattering rate is proportional to exciton density only.[25] Under such condition, we observed that the net MSD and rate of change of the MSD (corresponding to diffusivity) of HCTEs pumped with 405 nm laser was larger than their MSD rate of change when pumped with the 520 nm laser despite having the same exciton-exciton annihilation rate, validating the conclusion of *hot* exciton transport as the responsible mechanism for the high diffusivity. In addition, we observe that the time for HCTE transport to transition from regime I (*hot*) to II (*cold*) was higher for 405 nm excitation than 520 nm excitation as shown in Figure 3.11c, further supporting the existence of *hot* HCTEs as discussed in the next section.

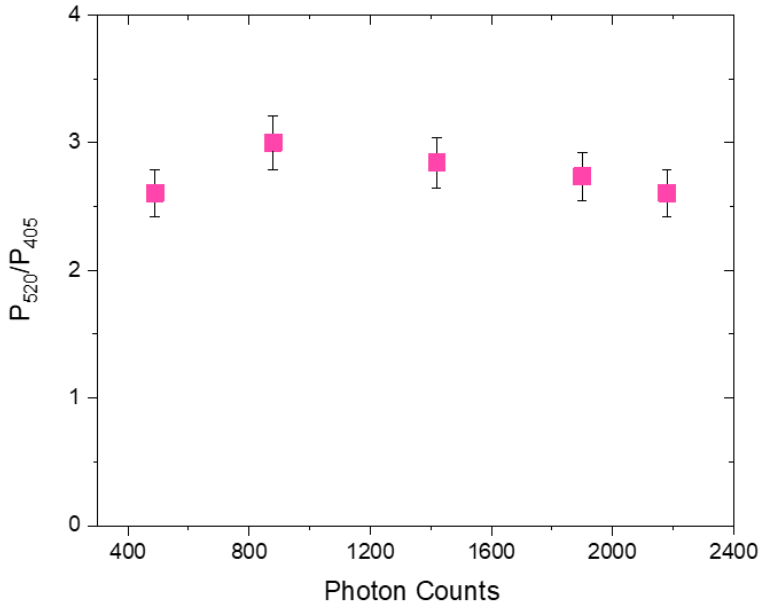

Figure 3.12 The ratio for average power of 520 nm to 405 nm laser that were used to create the same emission rate of HCTEs. The ratio of average power of the 520 nm to 405 nm lasers remained constant throughout the measurements, confirming that the contribution from Auger broadening remained identical for each excitation fluence as the Auger scattering rate is proportional to exciton density only.

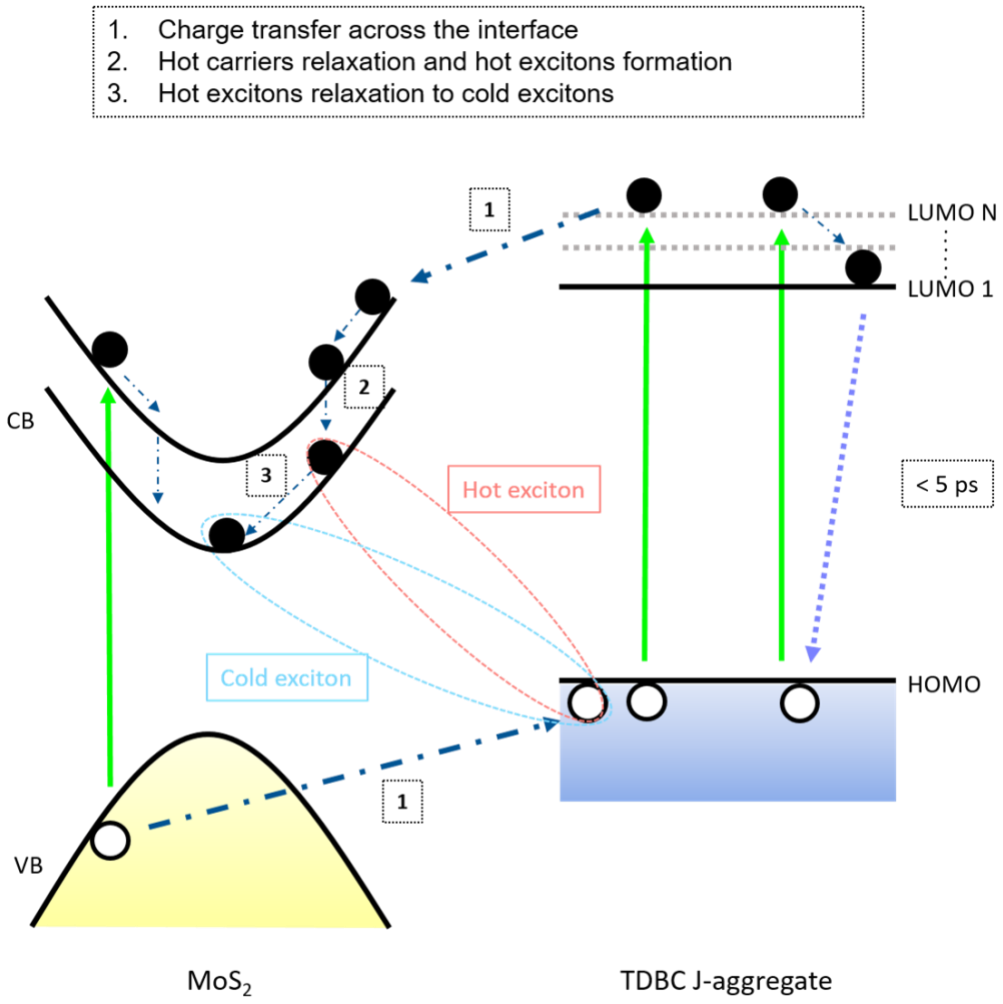

Figure 3.13 Hot exciton formation and relaxation paths for HCTEs. J-aggregate and MoS_2 exciton formation is instantaneous (compared to the time-scales of our measurement) after photoexcitation with a 3.1 eV source. 1. Within a few pico-seconds, interfacial charge transfer occurs due to the energy band alignment as electrons move to the conduction band of MoS_2 while holes move to the HOMO of j-aggregate. The j-aggregate lifetime is less than 5 ps. 2. The hot carriers of MoS_2 relax and form hot HCTEs within the first 40 ps assisted by polar optical phonons. 3. The hot excitons then relax their extra energy through acoustic exciton-phonon scattering, as discussed in the main text.

3.2.5 Relaxation dynamics of HCTEs

Figure 3.13 shows a schematic illustration of the plausible formation and relaxation paths of HCTEs at the organic-inorganic hybrid interface. Exciton formation in j-aggregates and MoS_2 is a very fast process and based on other reports,[1,15,23] we expect charge transfer to occur within the first few picoseconds after optical excitation[1] across the hybrid interface due to the favorable energy band alignments and form high energy HCTEs. The higher HCTE states have lower binding energy than MoS_2 excitons and hence there is a high probability of dissociation into *hot* carriers. Whether the relaxation from higher-energy HCTE states to the lowest-energy HCTE state is mediated through *hot* carriers or directly through bound CT states remains unclear. In either case, the relaxation creates lowest-energy HCTEs that possess non-zero kinetic energy, which results in the observed ultrafast transport. The relaxation rate of such *hot* HCTEs to *cold* HCTEs is (step 3 in Figure 3.13) governed by exciton-phonon interactions.[26–31] If the dielectric screening is small, the direct effect of the dipole field can dominate, and so the polar optical phonon (LO) interaction is typically the major scattering channel in polar materials at room temperature, which best describes our case and is confirmed from our theoretical calculations detailed in the methods section. It is worth noting that the transition time of *hot* HCTEs is longer than that of *hot* MoS_2 *A* excitons at an excitation density of 3.2 $\mu J/cm^2$ as seen in Figure 3.9a and 3.14. A similar trend is observed with higher power densities. Such variation in transition time stems from different extents of exciton-phonon interactions and can be better understood by estimating the relative strength of the Fröhlich and deformation potential interactions for MoS_2 *A* and HCT excitons with optical and acoustic phonons.

The Fröhlich optical phonon coupling model for charge carriers defines a dimensionless coupling constant δ that depends on the carrier mass and the dielectric environment.[32–37] An

estimate of the exciton-phonon Fröhlich interaction strength can be obtained with a modified version of the Fröhlich coupling constant defined as:

$$\delta = \left| \frac{e^2}{2\hbar} \sqrt{\frac{2M}{\hbar\omega_{LO}}} \left(\frac{1}{\varepsilon_\infty} - \frac{1}{\varepsilon_0} \right) \right| \tag{3.5}$$

where ε_0 is the static dielectric constant, ε_∞ is the optical dielectric constant, M is the translational mass, and ω_{LO} is the LO phonon angular frequency. A larger δ suggests a stronger exciton-phonon interaction that will result in a faster relaxation. With the assumption that the MoS_2 monolayer and HCTE experience identical dielectric environments and interact with the same optical phonons, the ratio of the Fröhlich constants depends solely on the ratio of the exciton translational masses, as shown below:

$$\frac{\delta_{CT}}{\delta_{MoS_2}} = \frac{\left| \frac{e^2}{2\hbar} \sqrt{\frac{2M_{CT}}{\hbar\omega_{LO}}} \left(\frac{1}{\varepsilon_\infty} - \frac{1}{\varepsilon_S} \right)_{CT} \right|}{\left| \frac{e^2}{2\hbar} \sqrt{\frac{2M_{MoS_2}}{\hbar\omega_{LO}}} \left(\frac{1}{\varepsilon_\infty} - \frac{1}{\varepsilon_S} \right)_{MoS_2} \right|} \approx \sqrt{\frac{M_{CT}}{M_{MoS_2}}} \tag{3.6}$$

While we are not able to estimate the translational mass of HCTEs due to the lack of hole effective mass in j-aggregate form, we expect the translational mass of HCTEs to be considerably lower than the translational mass of MoS_2 excitons since HCTEs are characterized by their exceptionally high diffusivities, as shown in Figure 3.9b. However, it remains unclear why HCTEs have small translational mass. Complex molecular dynamics simulations could provide insight but remains beyond the scope of the current work. As a result, we expect the Fröhlich coupling of HCTEs to be weaker than the Fröhlich coupling of MoS_2 excitons, resulting in a longer relaxation time for HCTEs. However, the Fröhlich coupling constant of MoS_2 *A* exciton, estimated to be 19.1 and corresponding to femtosecond relaxation time as detailed in the supplementary section, cannot explain the 100 ps relaxation that we observed. This suggest that at 300 K, the Fröhlich interaction

is the dominant exciton-phonon scattering mechanism until the exciton's excess energy drops below the optical phonon energy. Once below the optical phonon energy, the excess exciton energy is relaxed *via* the slower acoustic phonon scattering process (relaxation time for MoS_2 exciton *via* acoustic phonon scattering is in the sub picosecond regime).

Using the expressions for carrier-phonon scattering rate *via* the deformation potential interaction with the substitution of exciton translational mass for effective carrier masses, the ratio of acoustic phonon scattering rates of MoS_2 excitons and HCTEs depends on the ratio of their respective elastic properties, exciton translational masses, and deformation potential differences as shown below (refer to the supplementary material for more details):

$$\frac{\left(\frac{1}{\tau_{\mathbf{k},LA}}\right)_{CT}}{\left(\frac{1}{\tau_{\mathbf{k},LA}}\right)_{MoS_2}} = \frac{M_{CT}}{M_{MoS_2}} \frac{\rho_{MoS_2} s_{MoS_2}^2}{\rho_{CT} s_{CT}^2} \frac{\left(\Xi_{1,e} - \Xi_{1,h}\right)_{CT}^{\ 2}}{\left(\Xi_{1,e} - \Xi_{1,h}\right)_{MoS_2}^{\ 2}} \tag{3.7}$$

While we are unable to explicitly calculate the ratio of acoustic phonon scattering rates of HCTE and MoS_2 excitons due to the unavailability of hole deformation potentials and effective mass of TDBC J-aggregates, based on our experimental observations and supplementary Figure 3.14, we are able to estimate this ratio to be about 0.7. That is, HCTEs relax their excess energy *via* acoustic phonon scattering at a rate that is about 70% of the rate of MoS_2 excitons. This value corresponds to the ratio of the times at which the slopes of the MSD curves transition from their initial (high) to final (lower) value as shown in Figure 3.14. We associate these transition times with the average exciton-acoustic phonon scattering times that characterize the pico-second time scales of *hot* exciton energy relaxation of our observations. It is worth noting that the calculations of average scattering time in the methods section are estimates based on the expressions for carrier-phonon scattering and do not take into account other many-body interactions that may affect the

relaxation dynamics of MoS_2 excitons. Therefore, those calculations serve as a qualitative rather than quantitative guide to explain our observations (see methods section Figure 3.16).

Moreover, for a given optical phonon Fröhlich coupling constant, the transition time should be shorter when excited using lower energy photons due to the lower kinetic energy of excitons. This is consistent with our findings and is confirmed from the data shown in Figure 4c. Furthermore, we observe that the time for HCTEs transport to transition from regime I to regime II increases linearly with exciton density. This trend is due to the limited phonon density of states available for relaxation, also referred to as phonon bottleneck.[38,39] The transition time begins to saturate for higher excitation densities, which is possibly due to Auger recombination as more excitons begin to annihilate.[24] This is consistent with our data in Figure 3.14 as contributions from Auger scattering become non-negligible at high exciton densities.

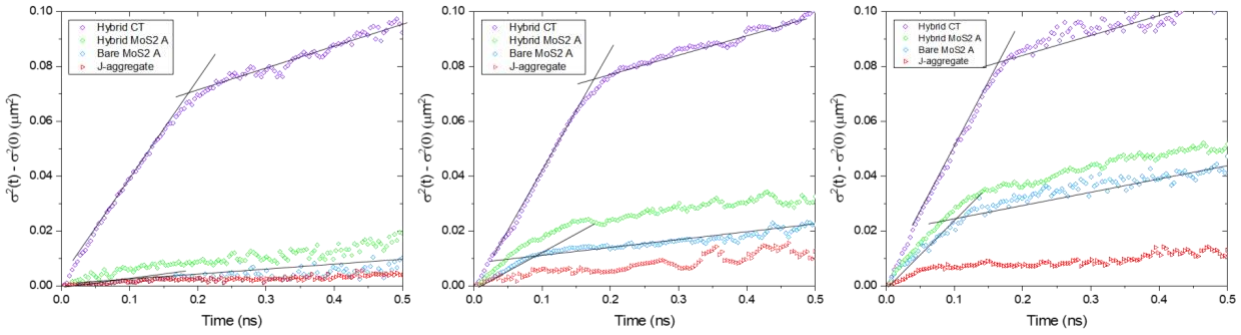

Figure 3.14 Power density dependent MSD curves and the fittings (black lines) for j-aggregate excitons, bare MoS_2 A excitons, MoS_2 A excitons in the hybrid layers, and hybrid CT excitons with power densities of 3.2 μJ/cm² (left), 6.4 μJ/cm² (middle), and 9.6 μJ/cm² (right). Two primary diffusion regimes are observed as (i) hot excitons fast transport, and (ii) cold excitons post-relaxation transport. The cross section of the fitting lines of region (i) and region (ii) of the MSD curve defines the relaxation time of hot excitons. Longer relaxation times of CT excitons are observed regardless of power density. By comparing the relaxation times (T) of bare MoS_2 A excitons and hybrid CT excitons, we obtain ratios (T_{CT}/T_{MoS2}) as 1.52, 1.45, and 1.41, respectively.

3.3 Conclusion

In conclusion, we show that the energy transport at organic-inorganic hybrid interfaces is dominated by HCTEs. We find that following photoexcitation, *hot* HCTEs are formed in about 36 ps *via* scattering with optical phonons. Based on the estimated relaxation time for acoustic and optical phonon scattering processes *via* deformation potential and Fröhlich interaction, we conclude that once the energy falls below the optical phonon energy, the excess kinetic energy is relaxed slowly *via* acoustic phonon scattering. During this time, fast-moving, *hot* HCTEs dominate the energy transport. While there could be contributions from free carriers arising from dissociation of HCTEs, we believe it is small due to high binding energy of HCTEs. Further investigation based on temperature dependent transport measurements along with transient absorption spectroscopy could shed light into the distribution of free carrier and HCTEs. The transition to *cold* excitons occurred at about 110 ps after formation (which is much longer than what is typically observed at organic/organic interfaces) and increased with excitation density, suggesting phonon bottleneck. We note that the diffusivity of HCTEs in both of the regions of transport was higher than MoS_2 *A* excitons. This work not only provides significant insight into the initial energy transport of HCTEs at organic-inorganic hybrid interfaces, but also contributes towards forming a complete physical picture of HCTE dynamics from formation to recombination. In conjunction with phonon engineering, we believe such high diffusivities in hybrid structures could enrich the applications from energy conversion to optoelectronic devices.

3.4 Methods

3.4.1 Sample preparation

MoS_2 monolayers are exfoliated from synthetically grown crystals (2D Semiconductors) and then transferred onto Si/SiO_2 and cover glass substrates using PDMS stamps (Gel Pak PF films). Potential monolayer MoS_2 samples were identified by optical contrast using Nikon upright microscope, and further confirmed using PL and Raman spectroscopy using 532 nm CW laser excitation and Princeton Instrument spectrometer (IsoPlane 320). TDBC J-aggregate films were prepared using layer-by-layer assembly with alternate polyelectrolyte (PDAC) and dye (TDBC) deposition. Both chemicals were purchased from Alfa Chemistry. The samples were first immersed into PDAC solution ($3*10^{-2}$ M) for 15 minutes and rinsed in three beakers of DI water for 2, 2, and 1 minutes respectively. The samples were then immediately transferred to the TDBC solution ($5*10^{-5}$ M) followed by the previous rinse routine. After 5 cycles, the samples were deposited with the final layer of electrolyte. To ensure uniform deposition of j-aggregate film onto the device, PL measurements were performed on random spots across the sample using a 532 nm CW laser excitation.

3.4.2 TRPL measurements for each exciton species

The TRPL dynamics are measured using time-correlated single photon counting (TCSPC) technique with a pulsed 405 nm laser. We specify each exciton species by using different filters for each measurement: j-aggregate's singlet excitons (595 nm) with 600 nm short pass filter, MoS2 A excitons (670 nm) with 650 nm long pass and 700 short pass filters, and HCTEs (760 nm) with 750 nm long pass filter.

3.4.3 Energy levels calculation of TDBC j-aggregate

The TDBC monomer was simulated using density functional theory (DFT) (Gaussian 09) with the B3LYP hybrid functionals. The basis set used was 6-31G. The simulation was performed by neglecting the effects of environment. For the TDBC monomer: HOMO Level: -0.21754 Hartree = -5.92 eV and LUMO Level: -0.10465 Hartree = -2.84 eV. The electronic structures of TDBC monomer in HOMO state and LUMO state are shown in Figure 3.15. We then model the J-aggregates as a linear chain of TDBC molecules. The TDBC molecules are considered perfect 2-level systems and we consider only nearest-neighbor interaction. Additionally, we consider only the lowest energy transition of the 1-exciton band. This assumption is reasonable since this transition is responsible for 81 % of the oscillator strength[40]. In our calculation, the effect of internal vibrations of the monomers is neglected. One can easily show that electronic transitions in J-aggregates is decoupled from the vibrational modes[41]. We calculate the eigen-frequencies using the tight-binding model, usually used to calculate the band structure in crystals: $\Omega_k = \omega_{monomer} + 2V\cos(\frac{\pi k}{N+1})$, where $\omega_{monomer}$ is transition energy of the monomer, V is nearest-neighbor coupling factor, N is molecules over which the exciton is delocalized. We calculate the intercoupling factor V from empirical data. From the reference [40], we know that the aggregate fluorescence is at 2.1 eV and the monomer fluorescence is at 2.3 eV. Considering N >> 1, we arrive at an energy difference related to $2V$. This gives us an intercoupling factor of -806.55 /cm or -0.1 eV. Due to nearest-neighbor interaction, there would be down-shifting of the LUMO level. Hence, the new LUMO level would be: $E_{LUMO} = -2.84 + 2(-0.1)\cos(\frac{\pi}{18}) = -3.036\ eV$.

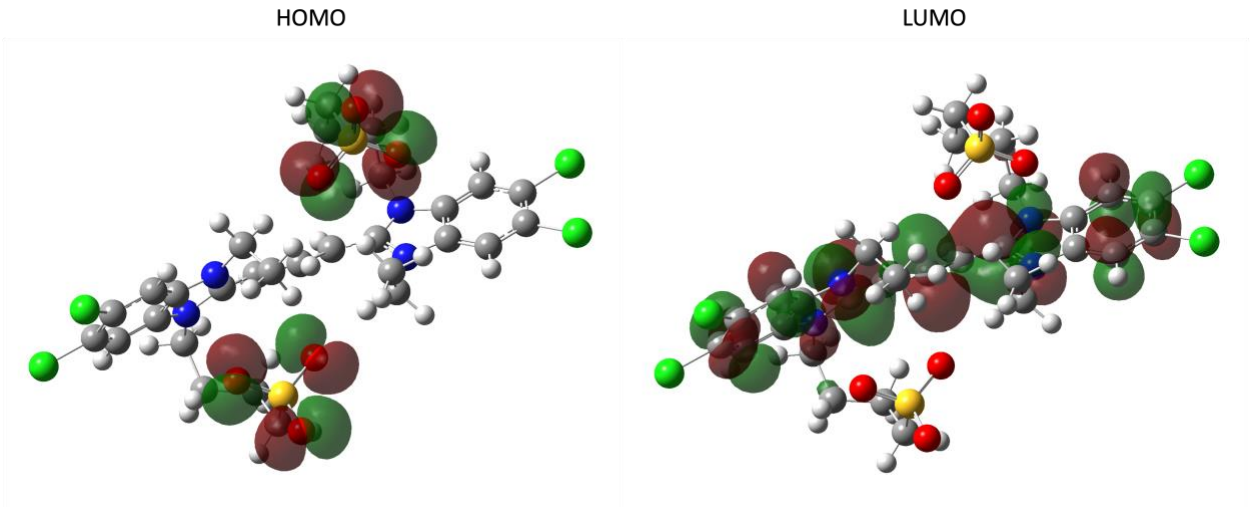

Figure 3.15 Electronic structures of TDBC monomer in HOMO state and LUMO state. The dark green areas are negatively charged, while the dark red areas are positively charged.

3.4.4 Relaxation dynamics of hot HCTEs through phonon scattering

The relaxation dynamics of excitons *via* phonon interaction can be quantitatively estimated by employing the scattering rate expressions developed for carrier-phonon scattering with the substitution of exciton translational mass for carrier effective mass. As discussed in the main text, the energy of HCTE is initially dissipated by ultrafast optical phonon scattering *via* the Fröhlich interaction. The Fröhlich constant that describes the strength of the exciton-optical phonon interaction is given by[42,43]

$$\delta = \left| \frac{e^2}{2\hbar} \sqrt{\frac{2M}{\hbar\omega_{LO}}} \left(\frac{1}{\varepsilon_\infty} - \frac{1}{\varepsilon_0} \right) \right| \tag{3.8}$$

where ε_0 is the static dielectric constant, ε_∞ is the high-frequency complex optical dielectric constant, M is the translational mass, and ω_{LO} is the LO phonon angular frequency. A larger δ

suggests higher strength of exciton-phonon interactions that will facilitate the transition from the hot state to the cold state. In addition, the exciton-phonon scattering rate in two-dimensional semiconductors can be further estimated using the approximate expression for the absorption and emission of optical phonons[44]:

$$\frac{1}{\tau_{\mathbf{k},LO}} \approx \frac{\pi\delta\omega_{LO}}{1+\frac{L_z}{4L_0}}[n_{LO}+(n_{LO}+1)\Theta(E_{\mathbf{k}}-\hbar\omega_{LO})] \tag{3.9}$$

where $E_{\mathbf{k}}$ is the exciton energy, $n_{LO}=[\exp(\hbar\omega_{LO}/k_BT)-1]^{-1}$ is the distribution function of phonons at temperature T, L_z is the layer thickness, and L_0 is a constant with dimensions of length and is defined as

$$L_0=\sqrt{\frac{\hbar}{2M\omega_{LO}}} \tag{3.10}$$

The Heaviside function $\Theta(E_{\mathbf{k}}-\hbar\omega_{LO})$ ensures that excitons with sufficient energy can emit optical phonons whereas there is no energy threshold for the absorption of optical phonons. For a two-dimensional Boltzmann distribution of hot excitons at temperature T, the average scattering time is generally given by

$$\langle\tau_{\mathbf{k}}\rangle=\frac{2}{\sqrt{\pi(k_BT)^3}}\int d\epsilon_{\mathbf{k}}\,\tau_{\mathbf{k}}\left(\frac{\epsilon_{\mathbf{k}}}{k_BT}-\frac{1}{2}\right)\sqrt{\epsilon_{\mathbf{k}}}\exp\left(-\frac{\epsilon_{\mathbf{k}}}{k_BT}\right)L_0=\sqrt{\frac{\hbar}{2M\omega_{LO}}} \tag{3.11}$$

And for the Fröhlich interaction, the average scattering time is specifically given by

$$\langle \tau_{\mathbf{k},LO} \rangle \approx \frac{1+\frac{L_z}{4L_0}}{\pi\delta\omega_{\mathrm{LO}}}\left\{\frac{1}{2n_{\mathrm{LO}}+1}\right.$$
$$+\left(\frac{1}{2n_{\mathrm{LO}}+1}-\frac{1}{n_{\mathrm{LO}}}\right)\left[\sqrt{\frac{4\hbar\omega_{LO}}{\pi k_B T}}\left(1+\frac{\hbar\omega_{LO}}{k_B T}\right)\exp\left(-\frac{\hbar\omega_{\mathrm{LO}}}{k_B T}\right)\right. \tag{3.12}$$
$$\left.\left.-\operatorname{erf}\left(\sqrt{\frac{\hbar\omega_{LO}}{k_B T}}\right)\right]\right\}$$

Simultaneously, hot HCTEs may relax their excess energy by optical phonon scattering *via* the deformation potential interaction. The scattering rate for the absorption and emission of LO phonons *via* the deformation potential interaction is given by

$$\frac{1}{\tau_{\mathbf{k},LO}} = \frac{M\left(\Xi_{0,e}-\Xi_{0,h}\right)^2}{\hbar^2\rho\omega_{LO}}\left[n_{LO}+(n_{LO}+1)\Theta(E_{\mathbf{k}}-\hbar\omega_{LO})\right] \tag{3.13}$$

where $\Xi_{0,e,h}$ are the zeroth-order deformation potentials of electron and hole and ρ is the mass density. Similarly, for a two-dimensional Boltzmann distribution of hot excitons at temperature T, the average scattering time *via* the deformation potential interaction is given approximately by

$$\langle \tau_{\mathbf{k},LO} \rangle \approx \frac{\hbar^2\rho\omega_{LO}}{M\left(\Xi_{0,e}-\Xi_{0,h}\right)^2}\left\{\frac{1}{2n_{\mathrm{LO}}+1}\right.$$
$$+\left(\frac{1}{2n_{\mathrm{LO}}+1}-\frac{1}{n_{\mathrm{LO}}}\right)\left[\sqrt{\frac{4\hbar\omega_{LO}}{\pi k_B T}}\left(1+\frac{\hbar\omega_{LO}}{k_B T}\right)\exp\left(-\frac{\hbar\omega_{\mathrm{LO}}}{k_B T}\right)\right. \tag{3.14}$$
$$\left.\left.-\operatorname{erf}\left(\sqrt{\frac{\hbar\omega_{LO}}{k_B T}}\right)\right]\right\}$$

Finally, once the energy of hot excitons has decreased below the energy of optical phonons, the remaining excess energy may be relaxed *via* acoustic phonon scattering *via* the deformation potential interaction. The scattering rate for the absorption and emission of LA phonons *via* the deformation potential interaction is given by

$$\frac{1}{\tau_{\mathbf{k},LA}} = \frac{M\left(\Xi_{1,e} - \Xi_{1,h}\right)^2 k_B T}{\rho \hbar^3 s_{LA}^2} \tag{3.15}$$

where $\Xi_{1,e,h}$ are the first-order deformation potentials of electron and hole, and s_{LA} is the speed of sound. Since the scattering rate is independent of the energy of the excitons, the average scattering rate is simply given by

$$\langle \tau_{\mathbf{k},LA} \rangle \approx \frac{\rho \hbar^3 s_{LA}^2}{M\left(\Xi_{1,e} - \Xi_{1,h}\right)^2 k_B T} \tag{3.16}$$

The average scattering time of MoS_2 excitons by acoustic and optical phonons *via* deformation potential and Fröhlich interactions are shown below.

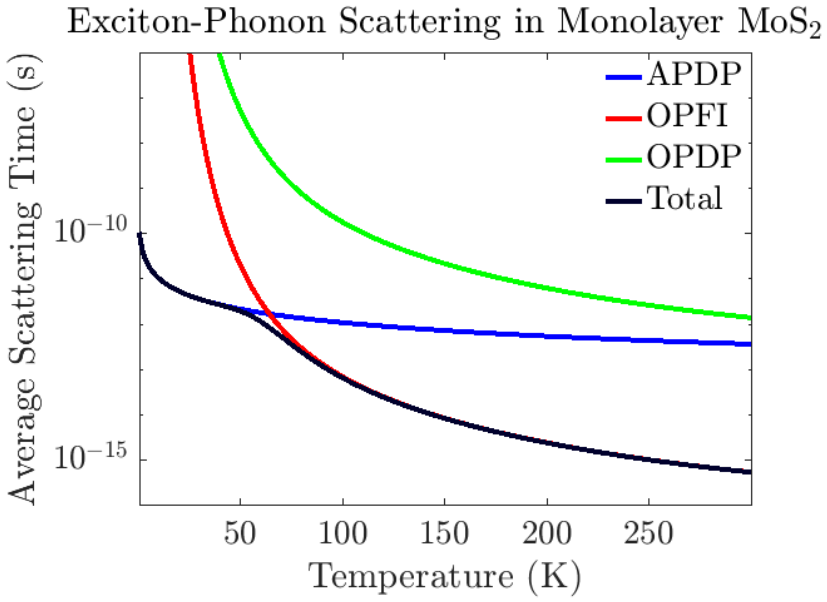

Figure 3.16 Average exciton-phonon scattering times in Monolayer MoS_2. APDP, OPDP, and OPFI stand for acoustic phonon deformation potential, optical phonon deformation potential, and optical phonon Fröhlich interaction, respectively. The material properties used in this calculation are summarized in Table 3.1.

Table 3.1 Material properties of MoS_2 used to calculate average exciton-phonon scattering times.

m_e^* (m_0)	m_h^* (m_0)	m_X^* (m_0)	$\hbar\omega_{LO}$ (meV)	$\Xi_{0,e}$ (eV/cm)	$\Xi_{0,h}$ (eV/cm)	$\Xi_{1,e}$ (eV)	$\Xi_{1,h}$ (eV)	ε_0	ε_∞ at $3eV$	δ
0.51[6]	0.58[6]	0.27	48.9[6]	5.8×10^{8} [6]	4.6×10^{8} [6]	4.5[6]	2.5[6]	15.5[7]	3+13i[7]	9.53

At 300 K, the Fröhlich interaction dominates the exciton-phonon scattering, and the excess energy of hot excitons in MoS_2 can be quickly relaxed in sub-picosecond time scales. Once below the optical phonon energy, the excess exciton energy is relaxed *via* acoustic phonon scattering. While unable to calculate the average scattering times of HCTEs due to the unavailability of the carrier's effective masses of TDBC J-aggregates in the literature, we believe the relative order-of-magnitude difference between the scattering times due to optical and acoustic phonon scattering of HCTEs is similar to that of MoS_2 excitons. As a result, we expect that HCTEs relax their excess energy first by optical phonon scattering *via* the Fröhlich interaction followed by acoustic phonon scattering.

We can estimate the relative strength of the Fröhlich and deformation potential interaction between MoS_2 and HCTEs with optical and acoustic phonons, respectively by calculating the ratio of their Fröhlich coefficients and scattering rates. For instance, with the assumption that MoS_2 and HCTE interact with the same type of phonons and experience similar dielectric environments, the ratio of their Fröhlich coefficients depends solely on the ratio of the exciton translational masses according to

$$\frac{\delta_{CT}}{\delta_{MoS_2}} = \frac{\left|\frac{e^2}{2\hbar}\sqrt{\frac{2M_{CT}}{\hbar\omega_{LO}}}\left(\frac{1}{\varepsilon_\infty}-\frac{1}{\varepsilon_s}\right)_{CT}\right|}{\left|\frac{e^2}{2\hbar}\sqrt{\frac{2M_{MoS_2}}{\hbar\omega_{LO}}}\left(\frac{1}{\varepsilon_\infty}-\frac{1}{\varepsilon_s}\right)_{MoS_2}\right|} \approx \sqrt{\frac{M_{CT}}{M_{MoS_2}}} \tag{3.17}$$

Similarly, the ratio of acoustic phonon scattering rates *via* the deformation potential interaction of MoS_2 and HCTEs depends on their elastic properties, the translational exciton masses, and deformation potential differences according to

$$\begin{aligned}\frac{\left(\frac{1}{\tau_{\mathbf{k},LA}}\right)_{CT}}{\left(\frac{1}{\tau_{\mathbf{k},LA}}\right)_{MoS_2}} &= \frac{\frac{M_{CT}\left(\Xi_{1,e}-\Xi_{1,h}\right)_{CT}^{\ 2}k_BT}{\rho_{CT}\hbar^3 s_{CT}^2}}{\frac{M_{MoS_2}\left(\Xi_{1,e}-\Xi_{1,h}\right)_{MoS_2}^{\ 2}k_BT}{\rho_{MoS_2}\hbar^3 s_{MoS_2}^2}} \\ &= \frac{M_{CT}}{M_{MoS_2}}\frac{\rho_{MoS_2}s_{MoS_2}^2}{\rho_{CT}s_{CT}^2}\frac{\left(\Xi_{1,e}-\Xi_{1,h}\right)_{CT}^{\ 2}}{\left(\Xi_{1,e}-\Xi_{1,h}\right)_{MoS_2}^{\ 2}}\end{aligned} \tag{3.18}$$

Since HCTE are characterized by their exceptionally high diffusivities, as shown in Figure 3.9b, we expect that the translational mass of HCTE is considerably lower that the translational mass of MoS_2 excitons. As a result, we expect that the Fröhlich coupling of HCTE be weaker than the Fröhlich coupling of MoS_2 excitons.

Similarly, we expect that the scattering rate of HCTE by acoustic phonons be lower than the scattering rate of MoS_2 excitons. While unable to explicitly calculate the ratio of acoustic phonon scattering rates of HCTE and MoS_2 excitons due to the unavailability of carrier deformation potentials of TDBC J-aggregates in the literature, based on our experimental observations and supplementary Figure 3.14, we are able to estimate this ratio to be about $\frac{\left(\frac{1}{\tau_{\mathbf{k},LA}}\right)_{CT}}{\left(\frac{1}{\tau_{\mathbf{k},LA}}\right)_{MoS_2}} \approx 0.7$, which corresponds to the ratio of the times at which the mean squared displacement curves' slopes

transition from their initial (high) to final (low) value. We associate these transitions times with the average exciton-acoustic phonon scattering times that characterized the hot exciton energy relaxation in our observed pico-second time scales.

We note that assumption of identical elastic properties of MoS_2 and TDBC j-aggregate was made to illustrate that the ratio of phonon-exciton scattering rates in the hybrid structure and MoS_2 cannot be calculated explicitly due to the unavailability of hole deformation potential and effective mass of TDBC j-aggregates. Based on classical mechanics, the elastic properties (Young's modulus) of the crystalline inorganic is a couple of order of magnitude higher than organics and so the elastic properties should be dominated by MoS_2.

We can eliminated such assumption and explicitly include the elastic properties of both material in Eq. (7), mass density and speed of sound, but doing so does not provide any more information because the deformation potential and hole effective mass of TDBC j-aggregates are still unknown. Therefore, with or without the assumption of similar elastic properties, based on our experimental data, we can only provide an estimate of the ratio of acoustic phonon-exciton scattering rates of TDBC j-aggregates and MoS2, which we showed to be about 0.7. That is, we estimated that HCTEs relax their excess energy *via* acoustic phonon scattering at a rate that is about 70% of the rate of MoS2 excitons. As stated in the main text, this value corresponds to the ratio of the times at which the slopes of the MSD curves transition from their initial to final values as shown in Figure 3.14.

3.5 References

(1) Petoukhoff, C. E.; Krishna, M. B. M.; Voiry, D.; Bozkurt, I.; Deckoff-Jones, S.; Chhowalla, M.; O'Carroll, D. M.; Dani, K. M. Ultrafast Charge Transfer and Enhanced Absorption in MoS2-Organic van der Waals Heterojunctions Using Plasmonic Metasurfaces. *ACS Nano* **2016**, *10*, 9899–9908.

(2) Flatten, L. C.; Coles, D. M.; He, Z.; Lidzey, D. G.; Taylor, R. A.; Warner, J. H.; Smith, J. M. Electrically Tunable Organic-Inorganic Hybrid Polaritons with Monolayer WS2. *Nat. Commun.* **2017**, *8*, 1–5.

(3) Renshaw, C. K.; Forrest, S. R. Excited State and Charge Dynamics of Hybrid Organic/Inorganic Heterojunctions. I. Theory. *Phys. Rev. B - Condens. Matter Mater. Phys.* **2014**, *90*, 1–15.

(4) Liu, X.; Gu, J.; Ding, K.; Fan, D.; Hu, X.; Tseng, Y. W.; Lee, Y. H.; Menon, V.; Forrest, S. R. Photoresponse of an Organic Semiconductor/Two-Dimensional Transition Metal Dichalcogenide Heterojunction. *Nano Lett.* **2017**, *17*, 3176–3181.

(5) Stöferle, T.; Mahrt, R. F. Energy Transfer in Hybrid Organic/Inorganic Nanocomposites. **2009**, 73930C.

(6) Walker, B. J.; Dorn, A.; Bulović, V.; Bawendi, M. G. Color-Selective Photocurrent Enhancement in Coupled J-Aggregate/Nanowires Formed in Solution. *Nano Lett.* **2011**, *11*, 2655–2659.

(7) Huang, Y.; Zhuge, F.; Hou, J.; Lv, L.; Luo, P.; Zhou, N.; Gan, L.; Zhai, T. Van der Waals Coupled Organic Molecules with Monolayer MoS_2 for Fast Response Photodetectors with Gate-Tunable Responsivity. *ACS Nano* **2018**, *4*, 4062-4073.

(8) Yu, S. H.; Lee, Y.; Jang, S. K.; Kang, J.; Jeon, J.; Lee, C.; Lee, J. Y.; Kim, H.; Hwang, E.; Lee, S.; Choi, J. Dye-Sensitized MoS $_2$ Photodetector with Enhanced Spectral Photoresponse. *ACS Nano* **2014**, *8*, 8285–8291.

(9) Huang, Y. L.; Zheng, Y. J.; Song, Z.; Chi, D.; Wee, A. T. S.; Quek, S. Y. The Organic–2D Transition Metal Dichalcogenide Heterointerface. *Chem. Soc. Rev.* **2018,** *47*, 3241-3264.

(10) Zheng, Y. J.; Huang, Y. L.; Chen, Y.; Zhao, W.; Eda, G.; Spataru, C. D.; Zhang, W.; Chang, Y. H.; Li, L. J.; Chi, D.; Quek, S. Y.; Wee, A. T. S. Heterointerface Screening Effects between Organic Monolayers and Monolayer Transition Metal Dichalcogenides. *ACS Nano* **2016**, *10*, 2476–2484.

(11) Zhu, T.; Yuan, L.; Zhao, Y.; Zhou, M.; Wan, Y.; Mei, J.; Huang, L. Highly Mobile Charge-Transfer Excitons in Two-Dimensional WS_2/Tetracene Heterostructures. *Sci. Adv.* **2018**, *4*, 3104.

(12) Jariwala, D.; Howell, S. L.; Chen, K. S.; Kang, J.; Sangwan, V. K.; Filippone, S. A.; Turrisi, R.; Marks, T. J.; Lauhon, L. J.; Hersam, M. C. Hybrid, Gate-Tunable, van der Waals *p-n* Heterojunctions from Pentacene and MoS2. *Nano Lett.* **2016**, *16*, 497–503.

(13) Homan, S. B.; Sangwan, V. K.; Balla, I.; Bergeron, H.; Weiss, E. A.; Hersam, M. C. Ultrafast Exciton Dissociation and Long-Lived Charge Separation in a Photovoltaic Pentacene-MoS2 van der Waals Heterojunction. *Nano Lett.* **2017**, *17*, 164–169.

(14) Zhu, T.; Yuan, L.; Zhao, Y.; Zhou, M.; Wan, Y.; Mei, J.; Huang, L. Highly Mobile Charge-Transfer Excitons in Two-Dimensional WS2/Tetracene Heterostructures. *Sci. Adv.* **2018**, *4*, 1–9.

(15) Hong, X.; Kim, J.; Shi, S.-F.; Zhang, Y.; Jin, C.; Sun, Y.; Tongay, S.; Wu, J.; Zhang, Y.; Wang, F. Ultrafast Charge Transfer in Atomically Thin MoS2/WS2 Heterostructures. *Nat. Nanotechnol.* **2014**, *9*, 682–686.

(16) Peyratout, C.; Daehne, L. Aggregation of Thiacyanine Derivatives on Polyelectrolytes. *Phys. Chem. Chem. Phys.* **2002**, *4*, 3032–3039.

(17) Cheng, C. H.; Li, Z.; Hambarde, A.; Deotare, P. B. Efficient Energy Transfer across Organic-2D Inorganic Heterointerfaces. *ACS Appl. Mater. Interfaces* **2018**, *10*, 39336–39342.

(18) Bradley, M. S.; Tischler, J. R.; Bulović, V. Layer-by-Layer J-Aggregate Thin Films with a Peak Absorption Constant of 106 Cm-1. *Adv. Mater.* **2005**, *17*, 1881–1886.

(19) Akselrod, G. M.; Deotare, P. B.; Thompson, N. J.; Lee, J.; Tisdale, W. A.; Baldo, M. A.; Menon, V. M.; Bulović, V. Visualization of Exciton Transport in Ordered and Disordered Molecular Solids. *Nat. Commun.* **2014**, *5*, 3646.

(20) Kulig, M.; Zipfel, J.; Nagler, P.; Blanter, S.; Schüller, C.; Korn, T.; Paradiso, N.; Glazov, M. M.; Chernikov, A. Exciton Diffusion and Halo Effects in Monolayer Semiconductors. *Phys. Rev. Lett.* **2018**, *120*, 207401.

(21) Cordovilla Leon, D. F.; Li, Z.; Jang, S. W.; Cheng, C. H.; Deotare, P. B. Exciton Transport in Strained Monolayer WSe 2. *Appl. Phys. Lett.* **2018**, *113*.

(22) Bouchaud, J.-P.; Georges, A. Anomalous Diffusion in Disordered Media: Statistical Mechanisms, Models and Physical Applications. *Phys. Rep.* **1990**, *195*, 127–293.

(23) Lee, J.-H.; Min, C.-K.; Joo, T. Ultrafast Optical Dynamics of Excitons in J-Aggregates

Optical Dynamics of Excitons in Aggregates of a Carbocyanine Dye Ultrafast Optical Dynamics of Excitons in J-Aggregates. *J. Chem. Phys. J. Chem. Phys. J. Chem. Phys. J Aggreg. J. Chem. Phys.* **2001**, *1141*.

(24) Cordovilla Leon, D. F.; Li, Z.; Jang, S. W.; Deotare, P. B. Hot Exciton Transport in WS E2 Monolayers. *Phys. Rev. B* **2019**, *100*, 1–6.

(25) Sun, D.; Rao, Y.; Reider, G. A.; Chen, G.; You, Y.; Brézin, L.; Harutyunyan, A. R.; Heinz, T. F. Observation of Rapid Exciton-Exciton Annihilation in Monolayer Molybdenum Disulfide. *Nano Lett.* **2014**, *14*, 5625–5629.

(26) Kaasbjerg, K.; Bhargavi, K. S.; Kubakaddi, S. S. Hot-Electron Cooling by Acoustic and Optical Phonons in Monolayers of MoS2 and Other Transition-Metal Dichalcogenides. *Phys. Rev. B* **2014**, *90*, 165436.

(27) Nie, Z.; Long, R.; Teguh, J. S.; Huang, C. C.; Hewak, D. W.; Yeow, E. K. L.; Shen, Z.; Prezhdo, O. V.; Loh, Z. H. Ultrafast Electron and Hole Relaxation Pathways in Few-Layer MoS2. *J. Phys. Chem. C* **2015**, *119*, 20698–20708.

(28) Miller, B.; Lindlau, J.; Bommert, M.; Neumann, A.; Yamaguchi, H.; Holleitner, A.; Högele, A.; Wurstbauer, U. Tuning the Fröhlich Exciton-Phonon Scattering in Monolayer MoS 2. *Nat. Commun.* **2019**, *10*.

(29) Sohier, T.; Calandra, M.; Mauri, F. Two-Dimensional Fröhlich Interaction in Transition-Metal Dichalcogenide Monolayers: Theoretical Modeling and First-Principles Calculations. *Phys. Rev. B* **2016**, *94*, 1–13.

(30) Chow, C. M.; Yu, H.; Jones, A. M.; Schaibley, J. R.; Koehler, M.; Mandrus, D. G.;

Merlin, R.; Yao, W.; Xu, X. Phonon-Assisted Oscillatory Exciton Dynamics in Monolayer MoSe2. *npj 2D Mater. Appl.* **2017**, *1*, 33.

(31) Sengupta, A.; Chanana, A.; Mahapatra, S. Phonon Scattering Limited Performance of Monolayer MoS2 and WSe2 *n*-MOSFET. *AIP Adv.* **2015**, *5*.

(32) Miyata, K.; Meggiolaro, D.; Tuan Trinh, M.; Joshi, P. P.; Mosconi, E.; Jones, S. C.; De Angelis, F.; Zhu, X. Y. Large Polarons in Lead Halide Perovskites. *Sci. Adv.* **2017**, *3*.

(33) Kaasbjerg, K.; Thygesen, K. S.; Jacobsen, K. W. Phonon-Limited Mobility in *n*-Type Single-Layer MoS 2 from First Principles. *Phys. Rev. B - Condens. Matter Mater. Phys.* **2012**, *85*, 1–16.

(34) Hastings, P. Polarons. *Encycl. Appl. Phys.* **2013**, *14*, 383-409

(35) Zheng, F.; Wang, L. W. Large Polaron Formation and Its Effect on Electron Transport in Hybrid Perovskites. *Energy Environ. Sci.* **2019**, *12*, 1219–1230.

(36) Feynman, R. P. *Statistical Mechanics : A Set of Lectures*, REV; Advanced book classics; Westview Press: Boulder, Colo., 1998; 5, 300-303.

(37) Leburton, J. P. Size Effects on Polar Optical Phonon Scattering of 1-D and 2-D Electron Gas in Synthetic Semiconductors. *J. Appl. Phys.* **1984**, *56*, 2850–2855.

(38) Yang, Y.; Ostrowski, D. P.; France, R. M.; Zhu, K.; Van De Lagemaat, J.; Luther, J. M.; Beard, M. C. Observation of a Hot-Phonon Bottleneck in Lead-Iodide Perovskites. *Nat. Photonics* **2016**, *10*, 53–59.

(39) Yang, J.; Wen, X.; Xia, H.; Sheng, R.; Ma, Q.; Kim, J.; Tapping, P.; Harada, T.; Kee, T. W.; Huang, F.; Cheng, Y. B.; Green, M.; Ho-Baillie, A.; Huang, S.; Shrestha, S.;

Patterson, R.; Conibeer, G. Acoustic-Optical Phonon Up-Conversion and Hot-Phonon Bottleneck in Lead-Halide Perovskites. *Nat. Commun.* **2017**, *8*.

(40) Spano, F. C. Fermion Excited States in One-Dimensional Molecular Aggregates with Site Disorder: Nonlinear Optical Response. *Phys. Rev. Lett.* **1991**, *67*, 3424.

(41) Saikin, S. K.; Eisfeld, A.; Valleau, S.; Aspuru-Guzik, A. Photonics Meets Excitonics: Natural and Artificial Molecular Aggregates. *Nanophotonics* **2013**, *2*, 21–38.

(42) Leburton, J. P. Size Effects on Polar Optical Phonon Scattering of 1-D and 2-D Electron Gas in Synthetic Semiconductors. *J. Appl. Phys.* **1984**, *56*, 2850–2855.

(43) Feynman, R. P. *Statistical Mechanics : A Set of Lectures*, REV; Advanced book classics; Westview Press: Boulder, Colo., 1998; 5, 300-303.

(44) Liu, T. H.; Zhou, J.; Liao, B.; Singh, D. J.; Chen, G. First-Principles Mode-By-Mode Analysis for Electron-Phonon Scattering Channels and Mean Free Path Spectra in GaAs. *Phys. Rev. B* **2017**, *95*, 1–11.

(45) Li, X.; Mullen, J. T.; Jin, Z.; Borysenko, K. M.; Buongiorno Nardelli, M.; Kim, K. W. Intrinsic Electrical Transport Properties of Monolayer Silicene and MoS2 from First Principles. *Phys. Rev. B* **2013**, *87*, 115418.

(46) Li, Y.; Chernikov, A.; Zhang, X.; Rigosi, A.; Hill, H. M.; van der Zande, A. M.; Chenet, D. A.; Shih, E.-M.; Hone, J.; Heinz, T. F. Measurement of the Optical Dielectric Function of Monolayer Transition-Metal Dichalcogenides. *Phys. Rev. B* **2014**, *90*, 205422.

Chapter 4 Self-erasable and Rewritable Optoexcitonic Platform

4.1 Introduction

Data processing and communication technologies have been growing exponentially in the last three decades. While the advancement in nanofabrication and metrology has significantly contributed to the growth, it has also contributed towards ability to reverse engineer products that result in enormous economic and intellectual property losses. Furthermore, the added vulnerability of the systems that utilize such products is a major concern for security applications. Thus, the requirement of an anti-tamper hardware at the systems level to detect possibility of espionage in secured communications, especially during remote operation cannot be underestimated. This is especially true since the semiconductor industry is plagued with counterfeit and tampered ICs[1-5], detection of which has become a major challenge.

The requirement of anti-tamper hardware can be categorized at various levels depending on the period. For instance, one may require products to be authenticated over long- or short-period of time without knowing precisely which part was tampered and/or when in a system. On the other hand, complete information transcription may be required to pinpoint the tampered component. Long-term hardware authentication is required over the lifetime of the product whereas short-term authentication of hardware is required during transitions such as transportation from one facility to another, tracking during lending period, etc. Hence, long-term authentication platform requires a one-time writing capability followed by multiple read cycles whereas short-term authentication

of hardware requires a rewritable information storage platform with self-erasing capability over a period of time. It is even more attractive, if the self-erasing volatility of the platform is dependent on environmental condition such as exposure to light, heat, etc. to further limit the scope of interference. Such platforms are inherently self-powered by the nature of operation and hence offer high reliability during the authentication process.

Optical and more particularly excitonic techniques that are based on optical transitions in semiconductors present an attractive solution for short-term authenticity. We demonstrate a new technique based on excitons that can be used to sense environmental changes in temperature/light to detect hardware tampering. In conjunction with organic molecules based on azobenzene that undergo structural change under exposure to light, we demonstrate an optically rewritable scratch pad that utilizes strain engineering on an overlying tungsten diselenide (WSe_2) monolayer to alter the optical bandgap, thereby changing the excitonic emission wavelength. Belonging to the class of transition metal dichalcogenides (TMD's) that are well known to support room temperature excitons, TMDs have demonstrated in both theory and experiments to be an ideal candidate for strain engineering due to the high sensitivity of bandgap to strain[6-8]. Band gap shift in tungsten diselenide (WSe_2) in the range of 25 meV ~ 100 meV (10 nm ~ 40 nm) for 1 % ~ 2 % of strain has been reported, and thus forms an ideal semiconductor material for the current study. The optical readout technique presented in the paper enables multiple, fast and remote readouts and thus is ideal for short term anti-tamper hardware.

Azobenzene, a widely applied photoisomerizing molecules, can be efficiently and reversibly switched between two structurally different forms upon exposure to different wavelengths of light and, as such is the molecule of choice for constructing light-powered molecular machines[9,10]. Light-powered and chemically fueled artificial molecular machines have long been recognized as

the key building blocks of the functional materials of the future[11]. These unique molecules have traditionally been synthesized and studied in solution, where they have been successfully used to induce conformational chemical changes in bound guest molecules or to synthesize other, smaller molecules, among other applications[12,13]. At equilibrium in the dark, azobenzene exists in the more stable *trans* conformation. Irradiation with UV light (300 – 400 nm) produces the *cis* isomer, which can revert back to the *trans* isomer thermally or upon irradiation with blue light (400 -500 nm). Azobenzene compounds have been used for optical control of conformation in diverse applications such as a photoswitch[14-16] to detect the change in the structure and function of biomolecular targets, and in strain engineering to tune the mechanical properties in low dimensional materials[17-20].

In this work, we create a compact self-erasable and rewritable optoexcitonic platform using monolayer WSe_2 on top of thin layers of an azobenzene based molecule, (*E*)-3,3'-((2-(4-((4-ethylphenyl)diazenyl)phenoxy)propane-1,3-diyl)bis(oxy))bis(propane-1,2-diol) (A3) (Molecular structures of *trans* state and *cis* isomers are shown in Figure 4.1a and detailed synthetic procedures can be found in the methods section). We induce local strain in monolayer WSe_2 by photoactivating underlying A3 molecules with irradiation of UV light, followed by selective exposure to visible light that reversibly switch the molecules between *trans* and *cis* state. The resulting strain in monolayer WSe_2 shifts the optical bandgap thereby causing a spectral shift in the photoluminescence signal. The strain can be instantaneously released by exposure to visible light or gradually over a period of time due to thermal relaxation.

4.2 Results and discussion

4.2.1 Photoisomerization of A3 molecules

Figure 4.1a shows molecular structures of the azobenzene based molecule, A3, in *trans* state and *cis* state. The thermally stable *trans* azobenzene isomer undergoes structural change to *cis* isomer upon irradiation of UV light, resulting in reduction of molecular length from 0.9 nm to 0.55 nm. The reverse transformation is gradual at ambient environment conditions but can be expedited by intense visible light irradiation or heat. We note that, the reaction of *cis* state to *trans* state is a much slower process as compared to the reverse reaction. This is partially due to the relative high absorption strength of *trans* isomer in UV regime than *cis* isomer in visible regime and the spectral intensities of the light sources used in the experiments.

Figure 4.1b shows the optical micrograph of monolayer and bilayer A3 films deposited on Si/SiO_2 substrate using Langmuir-Blodgett (LB) method[21]. The A3 molecule is highly polarized with a hydrophobic head and a hydrophilic tail, and as a result uniform layers of A3 can be achieved through specified treatments. The fabrication details can be found in the methods section. We monitor the A3 thin film isomerization dynamics over time using UV-Vis spectroscopy at room temperature. The UV-Vis absorption evolution of approximate 6 layers of A3 films (~12 nm) on cover glass following UV irradiation and visible light (Amscope series halogen lamp with an average fluence of 120 $\mu W/cm^2$) relaxation is shown in Figure 4.1c. We follow it by monitoring the transition under dark condition as shown in Figure 4.1d. We observe that 99% of the molecules remain in *cis* state within first 120 minutes as compared to less than 1% when exposed to visible light. In fact, only 20% of the molecules relax back to *trans* state after 24 hours (refer Figure 4.2). The inset of Figure 4.1d plots the percentage of molecules relaxing back to *trans*

state over 7 days. We observe that under dark conditions, 95% of the *cis* A3 molecules reverted back to *trans* state in 7 days. Thus, a message engraved on such an optoexcitonic platform would automatically disappear in about 7 days. The UV-Vis spectra of A3 molecules in solution form (10 mg/mL) and the reversible isomerization process for 5 complete cycles are shown in Figure 4.3.

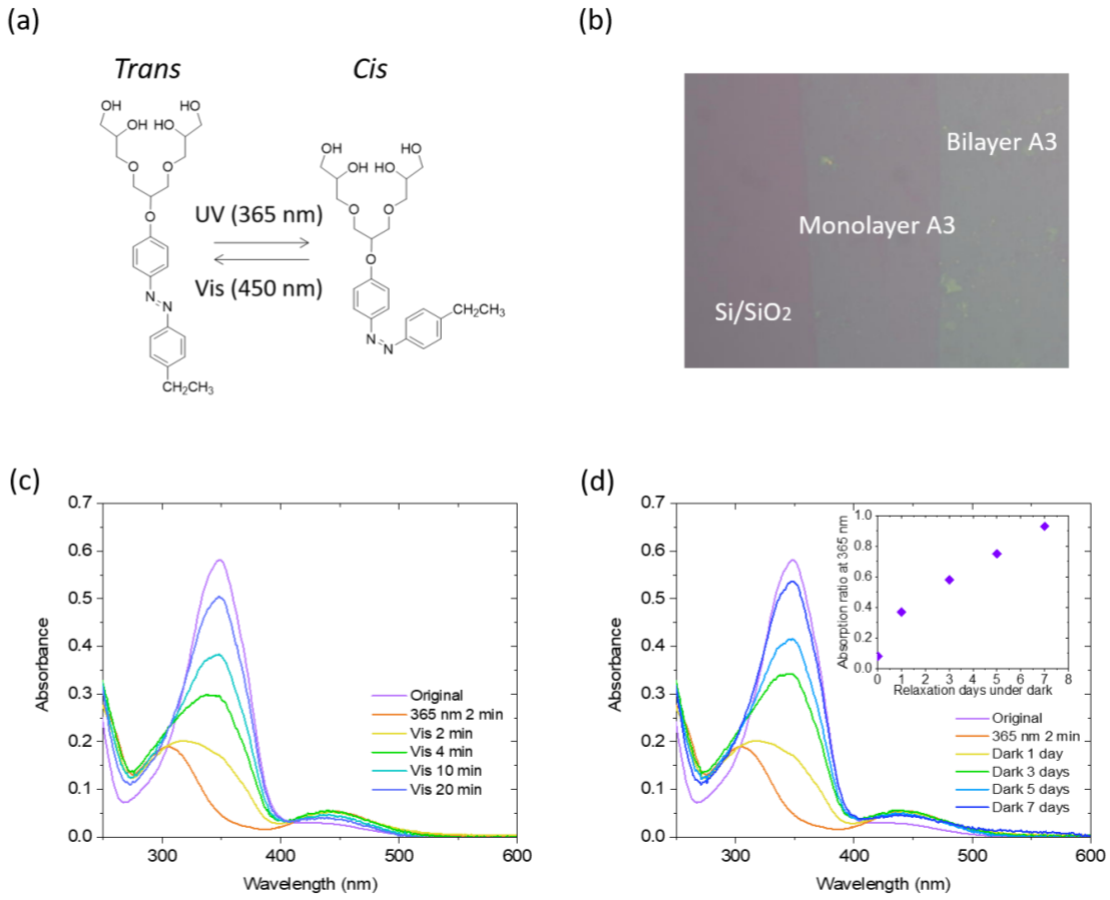

Figure 4.1 Photoisomerization of A3 films under visible light and dark environment at room temperature. (a) Chemical structures of A3 in *trans* and *cis* states. The thermally stable *trans* isomer (9 Å) can be switched to *cis* isomer (5.5 Å) upon UV irradiation, and reverted back gradually with visible light. (b) Optical micrograph of monolayer and bilayer A3 films on Si/SiO_2 substrate. The A3 films are prepared using Langmuir-Blodgett (LB) method. (c) UV-Vis absorption evolution of A3 film (5.4 nm) after UV treatment and visible light relaxation. (d) UV-Vis absorption evolution of the same A3 film under dark environment. The inset in (d) shows the percentage of *cis* A3 molecules relaxing back to *tans* state over time. It took 7 days for 95% of the A3 molecules to relax back to *trans* state under dark environment.

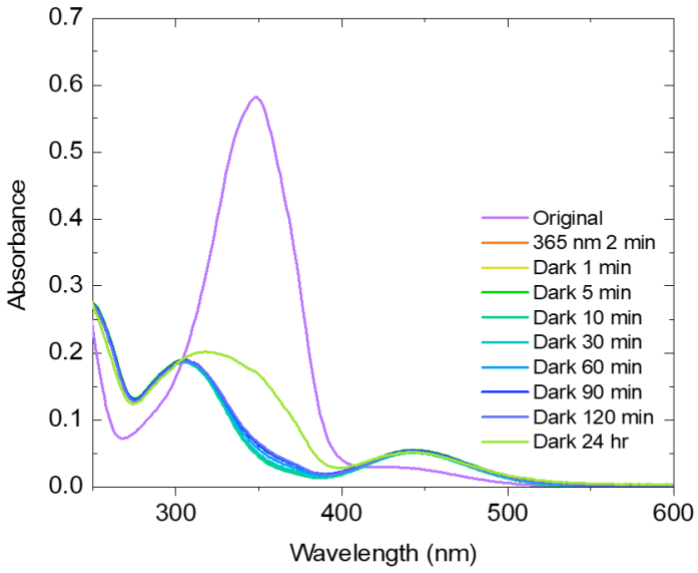

Figure 4.2 Photoisomerization of A3 molecule films (~6nm) under dark condition. We note that 99% of the molecules remain in cis state within first 120 minutes and only 20% of the molecules relax back to trans state after 24 hours.

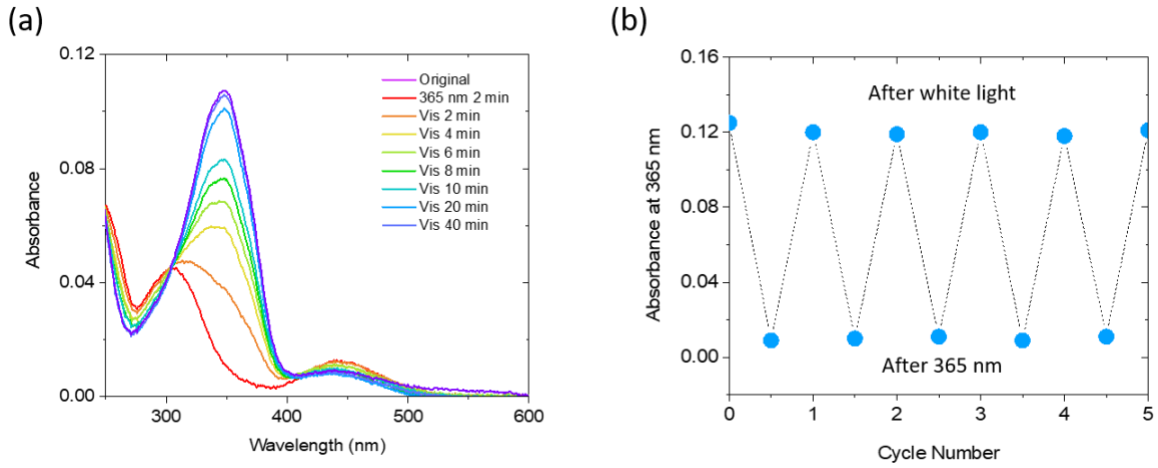

Figure 4.3 Photoisomerization of A3 molecule in solution form. We monitor the absorption intensity at 365 nm of the UV-Vis spectrum upon alternate irradiation of 2 minutes of 365 nm UV light and 60 minutes of white lights for 5 complete cycles. The absorption intensity remains fairly constant throughout each cycle.

4.2.2 Strain engineering on WSe_2 monolayer with A3 molecules

The samples were prepared by first transferring a mechanically exfoliated monolayer WSe_2 on top of bilayer A3 films. The sample were then irradiated with 365 nm UV light (with an average fluence of 100 $\mu W/cm^2$) for 5 minutes to completely convert the underlying A3 bilayer to *cis* state. A 450 nm laser was then used to achieve targeted relaxation of some of the molecules as *cis* A3 molecules shows higher absorption at this wavelength among the visible regime. The selective relaxation thus created local strain on the overlying monolayer and the process is illustrated in Figure 4.4a. We visualize the strain by conducting a sequence of PL spectral centroid map of the sample using a 532 nm excitation laser.

The brightfield image of the sample is shown in Figure 4.4b. The marked square region (10×10 μm^2) represents the scanned area for monitoring the PL shift, whereas the red line marks the linear profile scanned by the 450 nm laser during the write cycle. Figure 4.4c shows the PL centroid map monitoring the initializing of the film using UV, followed by the write cycle, and finally the relaxing phase. The transformation of all the molecules from *trans* to *cis* state is uniform and results in zero spectral shift in the PL spectrum as shown in Figure 4.4c (post UV). It is then followed by a write cycle, where a 450 nm laser (spot size of 2 μm, fluence of 25 $\mu J/cm^2$) is linearly scanned (dashed line) to create the local strain. Finally, the sample is exposed to white light to initiate relaxation and all the information is erased in ~ 40 minutes.

The strained regions are red shifted in energy due to tensile strain generated on the monolayer during the process[22,23]. Figure 4.5a shows the non-normalized PL spectrum of each step (on the dashed line). The observed PL intensity drop and broader linewidth after the write cycle (creation of local strain) are possibly due to contributions from the inhomogeneous broadening over the strained area as well as direct-to-indirect transition of the optical band gap of TMD

monolayer under high strain. The observation is consistent with reported studies based on strain[8,24,25]. In fact, the observed redshift of 11 nm translates to a very high tensile strain value of 1.1 %. The strain created by just 2 layers of A3 molecules (0.7 nm in isomerized length change) is significantly higher when compared to other reported studies that used mechanical setups to induce strain on TMDs. We also note that the PL intensity enhances from pre UV (*trans* state) to post UV (*cis* state) phase, and vice versa. This phenomenon has been observed by other group and is associated with doping and charge transfer in TMD materials[26,27]. It has also been reported that azobenzene based molecules in *trans* state provide pathways for doping and charge transfer while the photoisomerization from *trans* to *cis* configuration weakens such pathways[18,28]. In our case, the lowering emission intensity of WSe_2 monolayer by *trans* A3 molecules indicates *p*-doping where neutral excitons are suppressed by excess positive trions[26].

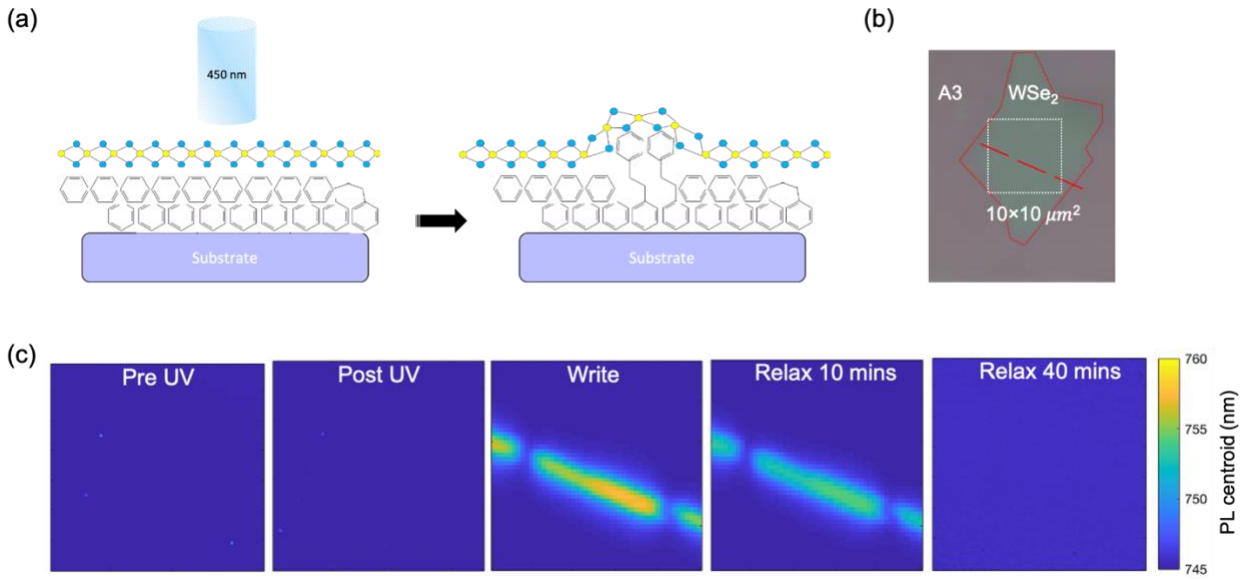

Figure 4.4 A3-initiated strain engineering on WSe_2 monolayer. (a) An illustration showing the creation of local strain on a monolayer WSe_2 by partially reverting some of the underlying *cis* molecules back to *trans* state using a 450 nm laser. We transfer a monolayer WSe_2 on top of bilayer A3 films and monitor the photoemission property. The induced strain in monolayer WSe_2 is translated into PL spectral shift. We observe a redshift of 11 nm that corresponds to 1.1% of tensile strain. The sample image is shown in (b). A sequence of PL spectral centroid map of the square region marked in (b) are shown in (c) where strained regions are mapped red shifted in energy indicating tensile strain. The sample is first irradiated with UV light for 5 minutes, where the complete underlying A3 bilayer undergoes *trans* to *cis* transformation that results in zero spectral shift in the PL spectrum. It is then followed by a writing process along the marked red lines in (b), where a 450 nm laser is used to partially relax the molecules back to *trans* state. This creates local strain as shown schematically in (a) and its effects are observed in the shift of the PL spectral centroid map. The strain resulted PL shift pattern disappears after 40 minutes of white light treatment.

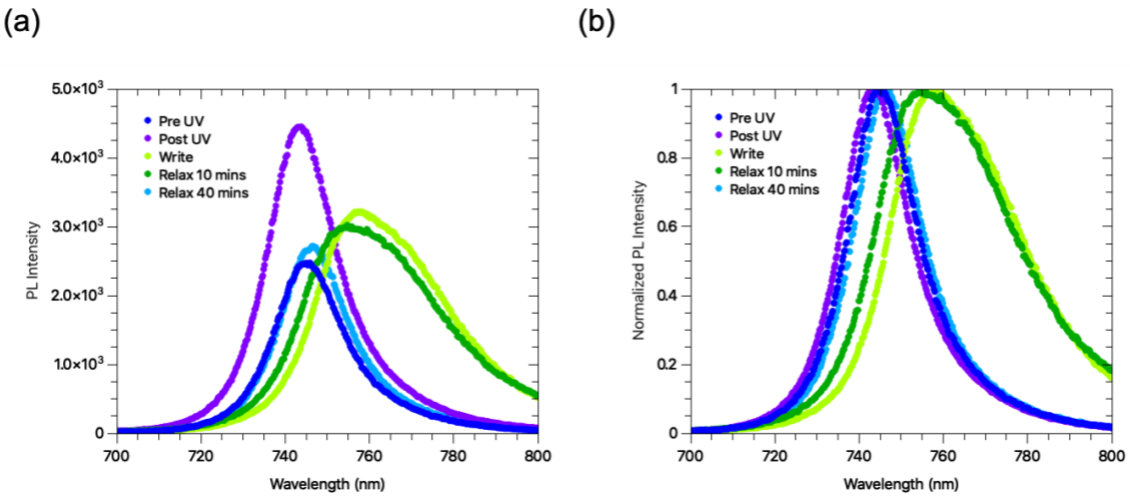

Figure 4.5 The PL spectral shift caused by strain in monolayer WSe_2. The spectra were taken at the center of the dashed line in Figure 2(c) for each step. (a) Non-normalized (b) Normalized PL spectra. We observe a redshift of 12 nm that corresponds to 1.1% of tensile strain in the writing phase. The PL redshift gradually disappears after relaxation process. The intensity drop at the strain area is caused by the direct to indirect transition of optical band gap in TMD monolayer.

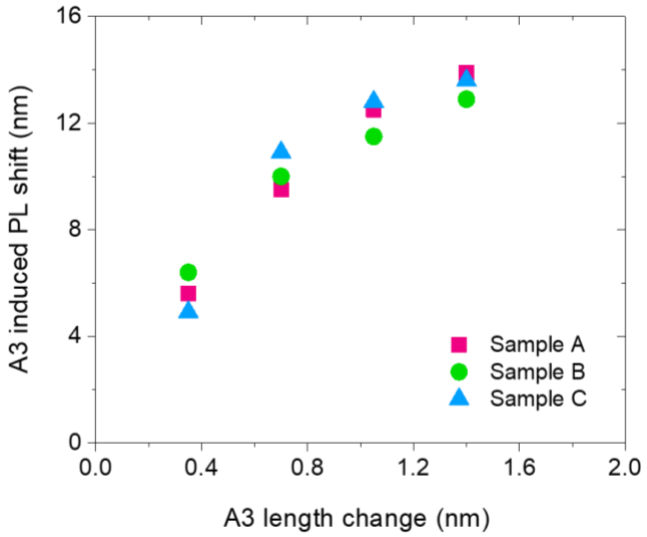

Figure 4.6 The strain created on monolayer WSe_2 is dependent on the thickness change of A3 films caused by photoisomerization. We compare the strains induced by A3 films of 1, 2, 3, and 4 layers (3 samples each) with the thickness of each layer switching from 0.9 nm (*trans* state) to 0.55 nm (*cis* state) or vice versa upon UV or white light treatment. A 0.7 nm height difference (bilayer) on the film produces an average of 9.5 nm PL red shift (1% tensile strain) on monolayer WSe_2. The PL shift increases with A3 film thickness, as expected. We observe that the PL shift increase starts to saturate for 3 and 4 layers of A3 films.

4.2.3 Relationship between A3 layers and induced strain

To further quantify the strain relationship with the underlying layer, we transfer monolayer WSe_2 on 1, 2, 3, and 4 layers of A3 films and induce local point strain using the method described earlier. Figure 4.6 compares the strain induced by A3 films of different layers (3 samples for each layer). As expected, the induced strain that is translated to PL shift, increases with A3 film thickness. The observation also confirms that the molecules in each deposited layer of A3 undergo photoisomerization. However, we observe that the increase in PL shift with number of layers appears to asymptote for higher number of A3 layers, possibly due to inability of A3 molecules to fully stretch with increased layers, thereby reducing the effective strain on the monolayer. Nevertheless, we could achieve a maximum strain of 1.4 % using four layers of A3 molecules.

4.2.4 A self-erasable and rewritable optoexcitonic platform

The ability to reversibly modulate the optical bandgap of monolayer WSe_2 by up to 1.4 % can be utilized to develop an optoexcitonic platform for an anti-tamper hardware system where the information is erased due to change in environmental condition (such as opening the system and exposing to light). Figure 4.7 demonstrates such an idea where letters *U* and *M* are sequentially written and erased on a 20 μm x 20 μm square region of monolayer WSe_2 with underlying bilayer A3. Letters are defined using a 450 nm laser (spot size ~ 2 μm) with 2 μm pixel pitch and are erased using white light irradiation. We have confirmed the repeatability of writing and erasing process over multiple samples. Such a platform can also be used to create self-destructible messages where critical information is erased at the end of expiry time.

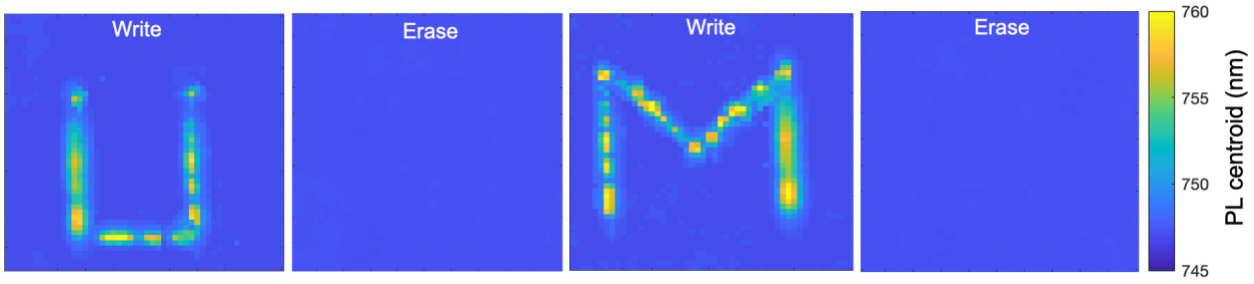

Figure 4.7 A demonstration of self-erasable and rewritable photonic platform. The PL maps show a writing and erasing sequence of letters *U* and *M* inscribed using the method described above on a 20 × 20 μm^2 area of monolayer WSe_2 on top of bilayer A3 films. Letters are written using 450 nm laser and are erased with 40 minutes of white light relaxation. (1) Write U. (2) Erase. (3) Write M. (4) Erase.

4.3 Conclusion

In summary, we demonstrate a potential anti-tamper hardware platform based on strain engineering excitonic properties of monolayer WSe_2 using underlying thin layers of A3 molecules. The induced tensile strain can be controlled using layer by layer approach and we report tensile

strain as high as 1.4 % for 4 layers of A3 molecules. The self-erasable and rewritable optoexcitonic platform has promising applications in self-destructible memory and anti-tamper hardware following further research on optimizing the A3 films for faster and more sensitive response. We believe that such an optoexcitonic platform can further benefit applications such as self-destruction of sensitive data over time, optical scratch pads to sensitive light detectors.

4.4 Methods

4.4.1 A3 molecules synthesis and preparation

(*E*)-1-(4-((1,3-bis((2,2-dimethyl-1,3-dioxolan-4-yl)methoxy)propan-2-yl)oxy)phenyl)-2-(4-ethylphenyl)diazene (1) was synthesized by a modified procedure reported in the literature[29]. (*E*)-4,4'-(diazene-1,2-diyl)diphenol (0.54 g, 2.4 mmol) was placed in a 100 mL round-bottom flask and dissolved in anhydrous *N*,*N*-dimethylformamide (DMF) under argon atmosphere. K_2CO_3 (1.00 g, 7.3 mmol) was added to the solution. The reaction mixture was stirred at room temperature for 10 minutes, followed by adding 1,3-bis((2,2-dimethyl-1,3-dioxolan-4-yl)methoxy)propan-2-yl methanesulfonate (1.43 g, 3.6 mmol). After refluxing overnight, DMF was evaporated under vacuum. The residue was dissolved in water, acidified with a saturated solution of NH_4Cl, and extracted with dichloromethane. The combined organic layers were dried over $MgSO_4$, filtered, and concentrated in vacuo. The crude product was purified by column chromatography to give 0.1 g of compound 1. ^{1}H NMR ($CDCl_3$, 300 MHz): δ = 7.87 (m, 2H), 7.80 (d, 2H), 7.32 (d, 2H), 7.06 (m, 2H), 4.02-4.19 (m, 3H), 3.45-3.89 (m, 12H), 2.74 (m, 2H), 1.19-1.44 (m, 15H) ppm.

(*E*)-3,3'-((2-(4-((4-ethylphenyl)diazenyl)phenoxy)propane-1,3-diyl)bis(oxy))bis(propane-1,2-diol) (2) was obtained as a yellow oily substance by the deprotection of compound 1 with trifluoroacetic acid (TFA). The general deprotection procedure with TFA is described in the literature[30].

4.4.2 A3 films fabrication through Langmuir-Blodgett (LB) method[31]

Firstly we prepare the amphiphile molecules (A3) that will create a monolayer in a water insoluble solvent. The subphase, typically water, is held in the hydrophobic trough top that provides good subphase containment. When the amphiphile solution is deposited on the water surface with a micro-syringe, the solution spreads rapidly to cover the available area. As the solvent evaporates, a monolayer forms at the air-water interface and a Langmuir film is created. The software-controlled barriers located at the interface then compress the monolayer until the surface pressure sensor indicates maximum packing density. A compressed, monolayer film can be considered as a two-dimensional solid with a surface area to volume ratio far above that of bulk materials. In these conditions, materials often yield fascinating new properties. Experiment using Langmuir troughs enables inference and understanding about how particular molecules pack when confined in two dimensions[32,33]. The surface pressure-area isotherm can also provide a measure of the average area per molecule and the compressibility of the monolayer.

4.5 References

(1) O'Boyle, J. (Maxim I. *Counterfeit ICs—the Serious Problem That Only We Can Make Go Away*; 2012.

(2) Holler, M.; Guizar-Sicairos, M.; Tsai, E. H. R.; Dinapoli, R.; Müller, E.; Bunk, O.; Raabe, J.; Aeppli, G. High-Resolution Non-Destructive Three-Dimensional Imaging of Integrated Circuits. *Nature* **2017**, *543*, 402–406.

(3) Shahbazmohamadi, S.; Forte, D.; Tehranipoor, M. Advanced Physical Inspection Methods for Counterfeit IC Detection. *Proc. Int. Symp. Test. Fail. Anal.* **2014**, 55–64.

(4) Guin, U.; Huang, K.; DiMase, D.; Carulli Jr, J. M.; Tehranipoor, M.; Makris, Y. Counterfeit Integrated Circuits: Detction, Avoidance, and the Challenges Ahead. *Proc. IEEE* **2014**, *102*, 1207–1228.

(5) Guin, U.; Huang, K.; Dimase, D.; Carulli, J. M.; Tehranipoor, M.; Makris, Y. Counterfeit Integrated Circuits: A Rising Threat in the Global Semiconductor Supply Chain. *Proc. IEEE* **2014**, *102*, 1207–1228.

(6) Shen, T.; Penumatcha, A. V.; Appenzeller, J. Strain Engineering for Transition Metal Dichalcogenides Based Field Effect Transistors. *ACS Nano* **2016**, *10*, 4712–4718.

(7) Liu, T.; Liu, S.; Tu, K. H.; Schmidt, H.; Chu, L.; Xiang, D.; Martin, J.; Eda, G.; Ross, C. A.; Garaj, S. Crested Two-Dimensional Transistors. *Nat. Nanotechnol.* **2019**, *14*, 223–226.

(8) Lloyd, D.; Liu, X.; Christopher, J. W.; Cantley, L.; Wadehra, A.; Kim, B. L.; Goldberg, B. B.; Swan, A. K.; Bunch, J. S. Band Gap Engineering with Ultralarge Biaxial Strains in Suspended Monolayer MoS2. *Nano Lett.* **2016**, *16*, 5836–5841.

(9) Okada, T.; Nozaki, N.; Seo, J.; Kwon, J. E.; Park, S. Y.; Hashizume, H.; Sasaki, T.; Ogawa, M. Photoinduced Structural Changes of Cationic Azo Dyes Confined in a Two Dimensional Nanospace by Two Different Mechanisms. *RSC Adv.* **2017**, *7*, 8077–8081.

(10) By, E. *RESPONSIVE Azobenzene-Containing Polymers and Liquid Crystals*.

(11) Joshi, G. K.; Blodgett, K. N.; Muhoberac, B. B.; Johnson, M. A.; Smith, K. A.; Sardar, R. Ultrasensitive Photoreversible Molecular Sensors of Azobenzene- Functionalized Plasmonic Nanoantennas. *Nano Lett.* **2014**, *14*, 532–540.

(12) Zhou, H.; Xue, C.; Weis, P.; Suzuki, Y.; Huang, S.; Koynov, K.; Auernhammer, G. K.; Berger, R.; Butt, H. J.; Wu, S. Photoswitching of Glass Transition Temperatures of Azobenzene-Containing Polymers Induces Reversible Solid-to-Liquid Transitions. *Nat. Chem.* **2017**, *9*, 145–151.

(13) Dong, M.; Babalhavaeji, A.; Collins, C. V.; Jarrah, K.; Sadovski, O.; Dai, Q.; Woolley, G.

A. Near-Infrared Photoswitching of Azobenzenes under Physiological Conditions. *J. Am. Chem. Soc.* **2017**, *139*, 13483–13486.

(14) Helmy, S.; Leibfarth, F. A.; Oh, S.; Poelma, J. E.; Hawker, C. J.; De Alaniz, J. R. Photoswitching Using Visible Light: A New Class of Organic Photochromic Molecules. *J. Am. Chem. Soc.* **2014**, *136*, 8169–8172.

(15) Beharry, A. A.; Sadovski, O.; Woolley, G. A. Azobenzene Photoswitching without Ultraviolet Light. *J. Am. Chem. Soc.* **2011**, *133*, 19684–19687.

(16) Nachtigall, O.; Kördel, C.; Urner, L. H.; Haag, R. Photoresponsive Switches at Surfaces Based on Supramolecular Functionalization with Azobenzene-Oligoglycerol Conjugates. *Angew. Chemie - Int. Ed.* **2014**, *53*, 9669–9673.

(17) Seo, S.; Min, M.; Lee, S. M.; Lee, H. Photo-Switchable Molecular Monolayer Anchored between Highly Transparent and Flexible Graphene Electrodes. *Nat. Commun.* **2013**, *4*, 1920–1927.

(18) Li, J.; Wierzbowski, J.; Ceylan, Ö.; Klein, J.; Nisic, F.; Le Anh, T.; Meggendorfer, F.; Palma, C. A.; Dragonetti, C.; Barth, J. V.; *et al.* Tuning the Optical Emission of MoS2 Nanosheets Using Proximal Photoswitchable Azobenzene Molecules. *Appl. Phys. Lett.* **2014**, *105*.

(19) Li, Z.; Lv, Y.; Ren, L.; Li, J.; Kong, L.; Zeng, Y.; Tao, Q.; Wu, R.; Ma, H.; Zhao, B.; *et al.* Efficient Strain Modulation of 2D Materials via Polymer Encapsulation. *Nat. Commun.* **2020**, *11*, 1–8.

(20) Qi, J.; Lan, Y. W.; Stieg, A. Z.; Chen, J. H.; Zhong, Y. L.; Li, L. J.; Chen, C. D.; Zhang, Y.; Wang, K. L. Piezoelectric Effect in Chemical Vapour Deposition-Grown Atomic-Monolayer Triangular Molybdenum Disulfide Piezotronics. *Nat. Commun.* **2015**, *6*, 1–8.

(21) Hussain, S. A.; Dey, B.; Bhattacharjee, D.; Mehta, N. Unique Supramolecular Assembly through Langmuir – Blodgett (LB) Technique. *Heliyon* **2018**, *4*, e01038.

(22) Desai, S. B.; Seol, G.; Kang, J. S.; Fang, H.; Battaglia, C.; Kapadia, R.; Ager, J. W.; Guo, J.; Javey, A. Strain-Induced Indirect to Direct Bandgap Transition in Multilayer WSe 2. *Nano Lett.* **2014**, *14*, 4592–4597.

(23) Aslan, O. B.; Deng, M.; Heinz, T. F. Strain Tuning of Excitons in Monolayer WSe2. *Phys. Rev. B* **2018**, *98*, 115308.

(24) Conley, H. J.; Wang, B.; Ziegler, J. I.; Haglund, R. F.; Pantelides, S. T.; Bolotin, K. I. Bandgap Engineering of Strained Monolayer and Bilayer MoS2. *Nano Lett.* **2013**, *13*, 3626–3630.

(25) Li, Y.; Wang, T.; Wu, M.; Cao, T.; Chen, Y.; Sankar, R.; Ulaganathan, R. K.; Chou, F.; Wetzel, C.; Xu, C. Y.; *et al.* Ultrasensitive Tunability of the Direct Bandgap of 2D InSe Flakes via Strain Engineering. *2D Mater.* **2018**, *5*.

(26) Nguyen, D. A.; Oh, H. M.; Duong, N. T.; Bang, S.; Yoon, S. J.; Jeong, M. S. Highly Enhanced Photoresponsivity of a Monolayer WSe2 Photodetector with Nitrogen-Doped Graphene Quantum Dots. *ACS Appl. Mater. Interfaces* **2018**, *10*, 10322–10329.

(27) Wang, Y.; Slassi, A.; Stoeckel, M. A.; Bertolazzi, S.; Cornil, J.; Beljonne, D.; Samorì, P.

Doping of Monolayer Transition-Metal Dichalcogenides via Physisorption of Aromatic Solvent Molecules. *J. Phys. Chem. Lett.* **2019**, *10*, 540–547.

(28) Kim, M.; Safron, N. S.; Huang, C.; Arnold, M. S.; Gopalan, P. Light-Driven Reversible Modulation of Doping in Graphene. *Nano Lett.* **2012**, *12*, 182–187.

(29) O. Nachtigall, C. Kördel, L. H. Urner, R. Haag, Angew. Chemie - Int. Ed. **2014**, 53, 9669.

(30) C. Kördel, C. S. Popeney, R. Haag, *Chem. Commun.* **2011**, *47*, 6584.

(31) S. A. Hussain, B. Dey, D. Bhattacharjee, N. Mehta, *Heliyon* **2018**, *4*, e01038.

(32) J. Kim, T. M. Swager, *Nature* **2001**, *411*, 1030.

(33) J. Kim, I. A. Levitsky, D. T. McQuade, T. M. Swager, *J. Am. Chem. Soc.* **2002**, *124*, 7710.

Chapter 5 Hybrid Transistors with Tunable Field-Effect Mobility

5.1 Introduction

Atomic scale thickness with sizable bandgap in monolayer transition metal dichalcogenide (TMD) can potentially revolutionize next generation devices including field-effect transistors (FETs) and photodetectors[1–4]. Despite the promising outlook for applications in electronics and optoelectronics, TMDs are still limited by the low electrical mobility under ambient conditions. Efforts to improve device performance through a variety of routes, such as modification of contact metals and gate dielectrics[5,6] or encapsulation in hexagonal boron nitride (h-BN)[7,8], have yielded limited success at room temperature. Strain engineering in semiconductor is routinely used to improve the efficiency and performance of essential electrical components such as silicon transistors, quantum well lasers, etc[9–11]. For instance, in metal oxide semiconductor field-effect transistors (MOSFETs), silicon channel is strained by using the lattice mismatch with the surrounding material. The stress in the silicon crystal alters the mobility of charge carriers and increases the switching speed of the MOSFET[12]. Monolayer TMDs are particularly suited to utilize this technique due to the large strain sensitivity of the bandgap and mechanical stability (elasticity) when subject to large strain levels. The sensitivity on the band gap of 2D TMDs to strain has been reported in a number of studies[13–17], including band gap shifts of hundreds of meV that have been induced in tungsten diselenide (WSe_2) by applying very large hydrostatic pressures and tensile strain. The effects of strain on the electronic band structure of single layer TMDs have been studied

in several works[13,18–20]. It has been shown that the application of compressive and tensile biaxial strain results in an indirect band gap in single layer TMDs. Furthermore, strained transistors have also been achieved by applying tensile strain to the material to stretch the atoms along one direction, and as a result, carriers experience reduced effective masses and less atomic force interference along this transport direction leading to higher mobilities[11,21–24].

In this study, we create a high performance and UV sensitive hybrid phototransistor based on thin layers of photoactive organic molecules overlaid by WSe_2 monolayers using strain engineering. Photochromic molecules are known to undergo reversible isomerization under light illumination at specific wavelengths. Typical photochromic molecules that respond to UV light at 365 nm are azobenzene, spiropyran, diarylethene, and stilbene[25–28]. Azobenzene, one of the most commonly used organic chromophores for optical switching, isomerizes from the *trans* to the *cis* state under UV radiation (365 nm)[29]. When azobenzene is exposed to visible light or heat, the *cis* structure of azobenzene switches back to the *trans* configuration. Strain is applied to monolayer WSe_2 of the transistor, as reported in our previous work[30], by partially photoactivating underlying azobenzene based molecules, (*E*)-3,3'-((2-(4-((4-ethylphenyl)diazenyl)phenoxy)propane-1,3-diyl)bis(oxy))bis(propane-1,2-diol) (A3) (The molecular structure is shown in Figure 4.1a) with alternate irradiation of UV light and visible light that reversibly switch the molecules between the *trans* and *cis* states. We observe a significant enhancement on the field-effect mobility of the hybrid transistor under ambient conditions that is comparable to mechanically strained TMDs and is tunable with UV or visible light sources. The tunability of mobility arises from the changing strain induced on the monolayer WSe_2 by the underlaying isomerizing azobenzene molecules. Furthermore, the phototransistor is highly sensitive to UV light, making it ideal for UV detection

applications. This capability has the potential to be used for next generation IC chips with tunable carrier mobility and even more as an ultrasensitive UV photodetector.

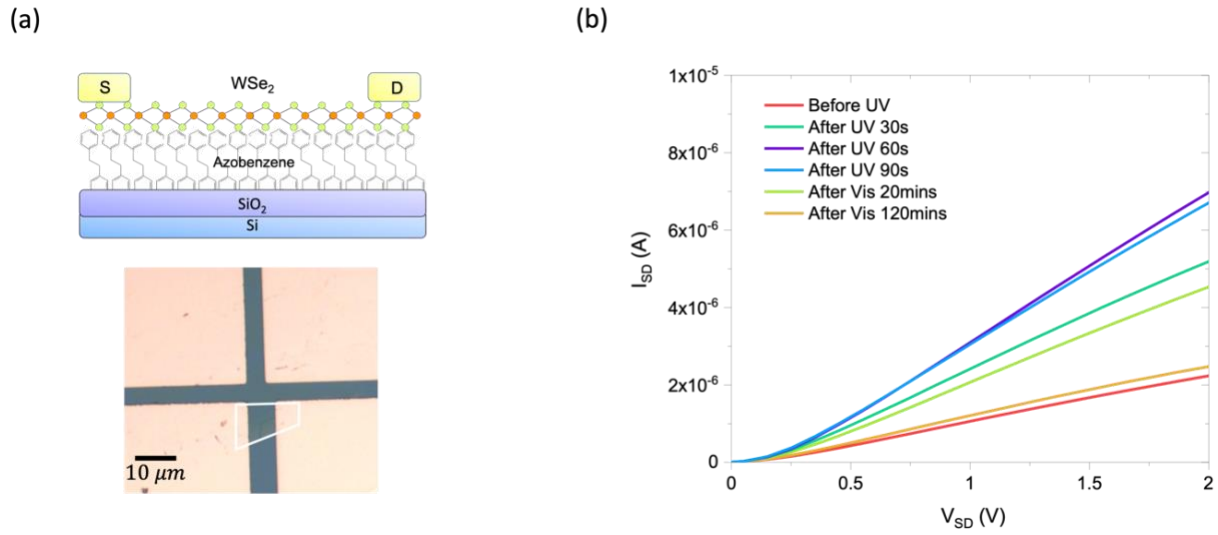

Figure 5.1 Enhanced performance of single layer WSe_2 transistor with A3 molecules. (a) Top: schematic illustration of the cross section of the hybrid transistor device. Bottom: optical microscope image of the hybrid transistor device with monolayer WSe_2 on top of bilayer A3 molecules. The channel length is 8 μm and the electrodes are Cr/Au 5/50 nm. (b) Output IV characteristics of the hybrid transistor with increasing time of UV irradiation followed by visible light relaxation. The output current was measured under dark condition right after UV exposure with the back-gate voltage set to -20 V. Significant current enhancement is observed after UV irradiation and it increases with irradiation time and saturates after about 60 seconds. The output IV measurement was then performed under visible light irradiation after 90 seconds of UV exposure. We note that the current reaches its original level after approximately 120 minutes of visible light irradiation.

5.2 Results and discussion

5.2.1 Enhanced performance of the hybrid transistor

Figure 5.1a shows the schematic illustration and the optical micrograph of the hybrid transistor consisting of monolayer WSe_2 layer (0.7 nm) on top of a thin film of bilayer A3

molecules (2 nm). Multiple devices with channel length varying from 5 to 10 μm were fabricated for this work. Figure 5.1b shows the output I-V characteristics of the hybrid transistor after UV light illumination as the underlaying A3 molecules convert from *trans* to *cis* state, followed by visible light illumination when the A3 molecules covert back from *cis* to *trans* state. The I-V plots are obtained under dark condition immediately after UV exposure to exclude any photocurrent contribution from the UV light. We observe a near linear behavior with the back-gate voltage set at -20 V. The channel conductance (slope of the curve) increases by 3-fold under UV irradiation until most of the *trans* isomers have converted to *cis* isomers around 60s. The output I-V characteristics is performed for the reverse case i.e. when the molecules relax under visible light irradiation after 90 seconds of UV exposure. The original device characteristic are obtained after approximately 120 minutes of visible light irradiation. As mentioned above, the relaxation process of the molecules takes much longer due to the relatively lower absorption in the visible regime. Here the UV light and visible light fluences are 150 μW/cm^2 and 55 μW/cm^2, respectively. The structural change can be accelerated by using more intense UV and Visible irradiations.

The output I-V characteristics of the hybrid transistor are modulated by the photoisomerization of A3 molecules, which creates strain on the monolayer WSe_2, specifically at the regions near the electrodes as illustrated in Figure 5.2a. The mechanical strain in TMDs has been proposed to boost carrier mobility[11,32], and has been shown to influence the local bandgap and quantum emission properties of TMDs[13,33]. Another possible mechanism arises from the doping and charge transfer of A3 molecules after UV excitation. More detailed discussions on the enhancement mechanisms are shown in the following sections.

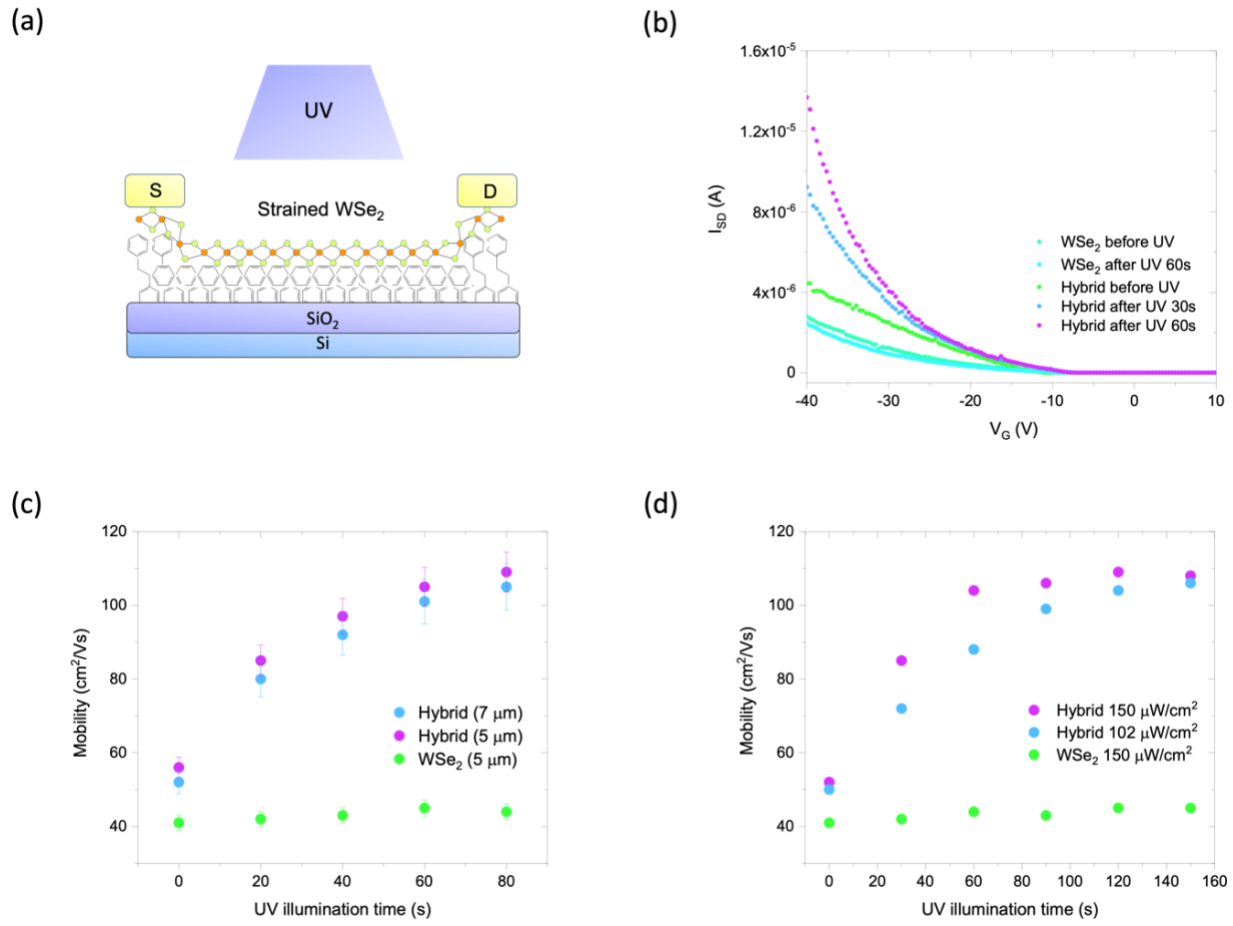

Figure 5.2 The enhanced and tunable field-effect carrier mobility in the hybrid transistor. (a) Schematic illustration of the hybrid transistor device under UV exposure. Due to photoisomerization of the underlaying A3 molecules, strain is created on WSe_2 near the electrodes. (b) IV transfer characteristics of bare WSe_2 monolayer transistor and hybrid (WSe_2 monolayer and A3 molecules) transistor under UV irradiation. The IV measurements were conducted under dark condition right after UV irradiation in order to exclude the photocurrent generated by UV light. The V_{SD} was set to 1 V. The enhancement of I_{SD} by the A3 molecules increases with UV irradiation time and it saturates after 60 seconds, similar to the observation in Figure 2. (c) Field-effect hole mobility of the bare WSe_2 monolayer transistor and hybrid transistor with various channel lengths (indicated in the legend). The hole mobility in the hybrid device is UV irradiation time-dependent and is enhanced by over 2 fold after 60 seconds. The error bars show the fluctuations of 5 measurements for each device, and which confirms the carrier mobility enhancement is independent on sample channel dimension. (d) UV irradiation time-dependent hole mobility measurements of the hybrid FET with different UV powers. As expected, it takes longer for the mobility to reach maximum when using lower powers.

5.2.2 Enhanced and tunable mobility of the hybrid transistor

We investigate the charge carrier transport properties of the hybrid transistor device modulated by the underlaying A3 molecules. Figure 5.2a shows the schematic illustration of the hybrid transistor device under UV irradiation. As demonstrated, strain is created on WSe_2 near the electrodes thanks to photoisomerization of the underlaying A3 molecules. Figure 5.2b shows the IV characteristics of a bare WSe_2 monolayer transistor and a hybrid (WSe_2 monolayer and A3 molecules) transistor under different UV irradiation time. The IV measurements are conducted under dark condition right after UV irradiation in order to exclude the photocurrent generated by UV light with the V_{SD} set to 1 V. Monolayer WSe_2 is an intrinsically *p*-type semiconductor as can be confirmed from the transfer IV curves. The significant enhancement of the source-drain current by A3 molecules increases with UV irradiation time that is consistent with the output IV results in Figure 5.2b.

Figure 5.2c shows the field-effect hole mobility of the bare WSe_2 monolayer transistor and the hybrid transistor with various channel lengths (indicated in the legend) as a function of UV irradiation time. The field-effect mobility μ_{FET} is given by:

$$\mu_{FET} = \left(\frac{dI_{SD}}{dV_G}\right) \times \left(\frac{L}{W \times C_i \times V_{SD}}\right) \tag{5.1}$$

where $\left(\frac{dI_{SD}}{dV_G}\right)$ is the transconductance, L is the channel length, W is the channel width, and C_i = 1.3×10^{-8} F/cm^2 is the capacitance of the dielectric (SiO_2) between the channel and the back gate per unit area. The hole mobility of the hybrid device is UV irradiation time-dependent and is enhanced by over 2-fold (115 cm^2/Vs) after 60 seconds as compared to its bare WSe_2 counterpart (42 cm^2/Vs), which remains unchanged after UV exposure. We note that the initial mobility of the hybrid transistor under dark condition (UV exposure time at 0 s) is about 30% higher than that of

the bare WSe_2 transistor, indicating the initial doping effect from *trans* A3 molecules to monolayer WSe_2. The error bars in the plot show the fluctuations of the results of 5 measurements at each UV exposure time for each device. Since the calculated field-effect mobilities for the two channel lengths of the hybrid transistors overlap with the fluctuation ranges, we note that the enhanced carrier mobility is independent on the channel dimension as mobility is an intrinsic property of a material.

Figure 5.2d shows the UV power dependent field-effect mobility as a function of UV irradiation time. As expected, it takes longer for the mobility to reach its maximum value when using lower fluence levels. It further confirms that the hole mobility reaches values as high as 110 cm^2/Vs for both cases simply by photoactivating the underlaying A3 molecules using UV light. Ultra-high carrier mobility in TMD semiconductors (electron mobility of monolayer MoS_2 450 cm^2/Vs and hole mobility of monolayer WSe_2 158 cm^2/Vs) has been reported using crested dielectric substrates that create random mechanical strain on the monolayers. On the one hand, the strain can stretch the distance between neighboring atoms in the channel, resulting in less atomic force interference for carrier transport. On the other hand, the strain can reduce the effective mass of the transport carrier of the monolayer semiconductor, enabling faster carrier transport. In our case, the strain on the WSe_2 monolayer generated by A3 molecules is at the two electrode regions, as shown in the illustration of Figure 5.2a.

The total mobility of the hybrid transistor includes initial mobility (unstrained area) and enhanced mobility induced by UV irradiation and isomerization of underlaying A3 molecule (strained area). The enhancement of the WSe_2 monolayer's hole mobility can be caused by both strain and charge transfer; however, the weighs of each contribution remains unclear. We note that the doping from A3 molecules of *trans* state is estimated from the initial mobility under dark

condition as discussed in Figure 5.2c. Once the UV light source is turned on, the enhanced mobilities from both strain and charge transfer caused by A3 molecules of both *trans* and *cis* state happen simultaneously, making it a challenge to differentiate between the two.

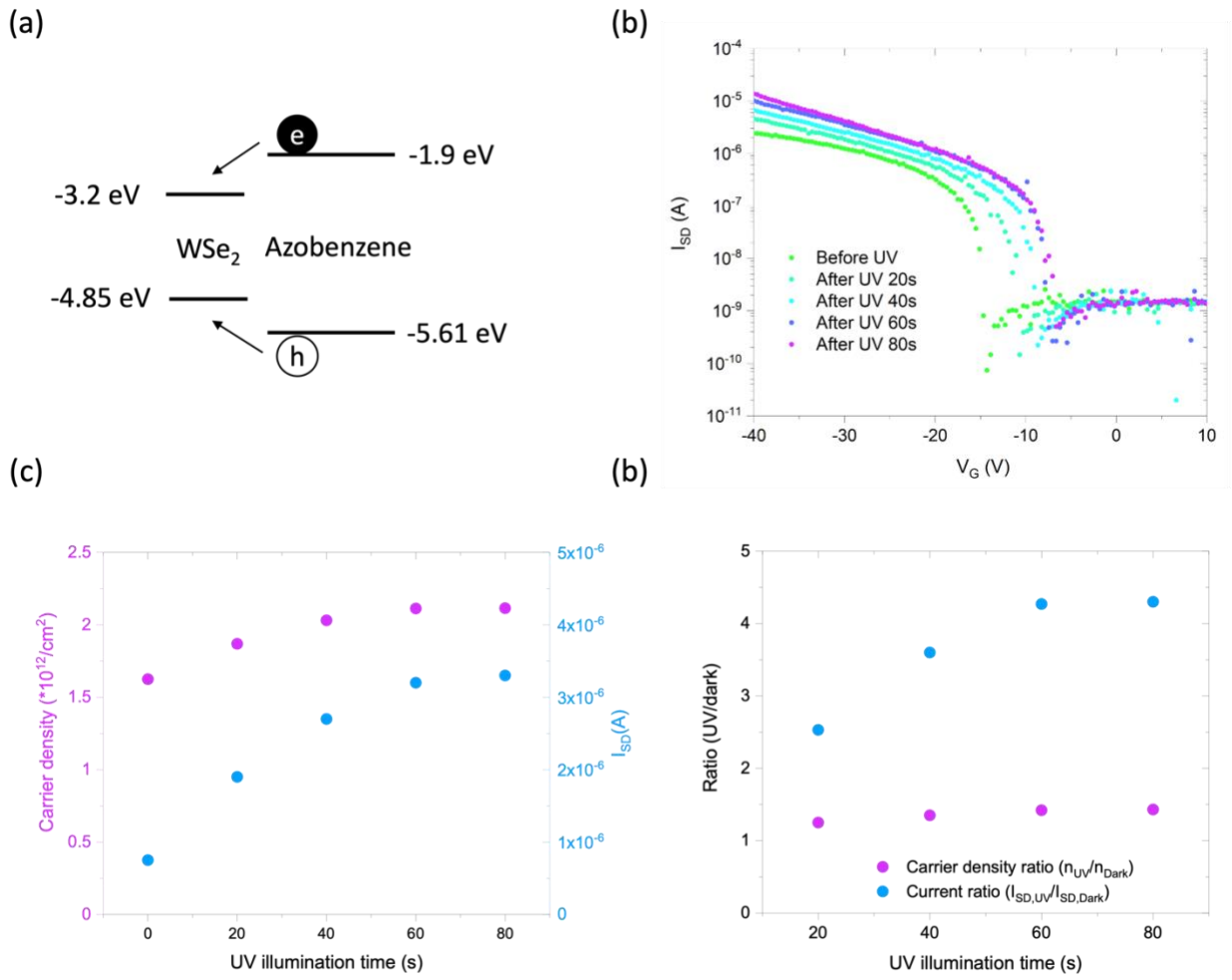

Figure 5.3 The effect of charge transfer on field-effect mobility enhancement. The effect of charge transfer on field-effect mobility enhancement. (a) Illustration of energy levels of monolayer WSe_2 and azobenzene isomers in trans state. After UV light illumination, charges in A3 molecules transfer to WSe_2 due to favorable energy band alignment. (b) IV transfer characteristics in log scale before and after UV irradiation. The threshold voltage shifts toward positive gate voltage after UV exposure, indicating positive charge transfer from A3 molecules of *trans* state to WSe_2. (c) Charge carrier density and source-drain current as a function of UV irradiation time. (d) Enhancement of carrier density and source-drain current after UV irradiation compared to original dark condition.

5.2.3 Strain and charge transfer in the hybrid transistor

To tackle the challenge, we analyze the current enhancement by charge transfer from A3 molecules to WSe_2 qualitatively and quantitatively. Figure 5.3a shows the energy levels of valence

band (VB) and conduction band (CB) of monolayer WSe_2 and highest occupied molecular orbital (HOMO) and lowest unoccupied molecular orbital (LUMO) of azobenzene isomers in *trans* state. After photoexcitation by UV light, the electrons in *trans* A3 molecules are excited to LUMO, leaving holes in HOMO. These free charge carriers in A3 molecules have tendency to transfer to WSe_2 due to favorable energy level alignment, and as a result, increase the source-drain current. The charge transfer process gets much slower after the isomers convert from *trans* to *cis* state due to the relatively low absorption of *cis* isomers in the UV regime. This can be verified in Figure 5.3b that shows the IV transfer characteristics of the hybrid transistor before and after UV irradiation in log scale. While the significant shift of the threshold voltage (V_{TH}) after UV irradiation indicates efficient charge transfer from A3 molecules to WSe_2, the charge transfer rate (the V_{TH} shift) saturates at approximately 60s as most of molecules switch from *trans* to *cis* state.

Figure 5.3c shows the carrier density and source-drain current as a function of UV irradiation time. The source-drain current is measured under dark condition after UV light exposure as described in previous sections with V_{SD} and V_G set to 1V and -20 V, respectively. The charge carrier density (n) above threshold voltage (V_{TH}) in linear output regime (Figure 5.1b) can be estimated by:

$$n = \frac{C_i}{q}(V_G - V_{TH}) \tag{2}$$

As discussed above, we observe threshold voltage shift after UV irradiation from the transfer IV characteristics as shown in Figure 5.3b, which translates to the increased carrier density with UV exposure time as shown in Figure 5.3c. As expected, both carrier density and channel current saturate after 60 seconds of UV irradiation. We observe a more drastic source-drain current enhancement as compared to the carrier density increase caused by charge transfer in the WSe_2

channel, which can be better perceived in Figure 5.3d, where we compare the ratio of charge carrier density and source-drain current under dark and UV conditions. Since the current is proportional to the charge density in the channel under the conditions of Ohmic contact and linear bias region, the current enhancement is primarily contributed by the strain.

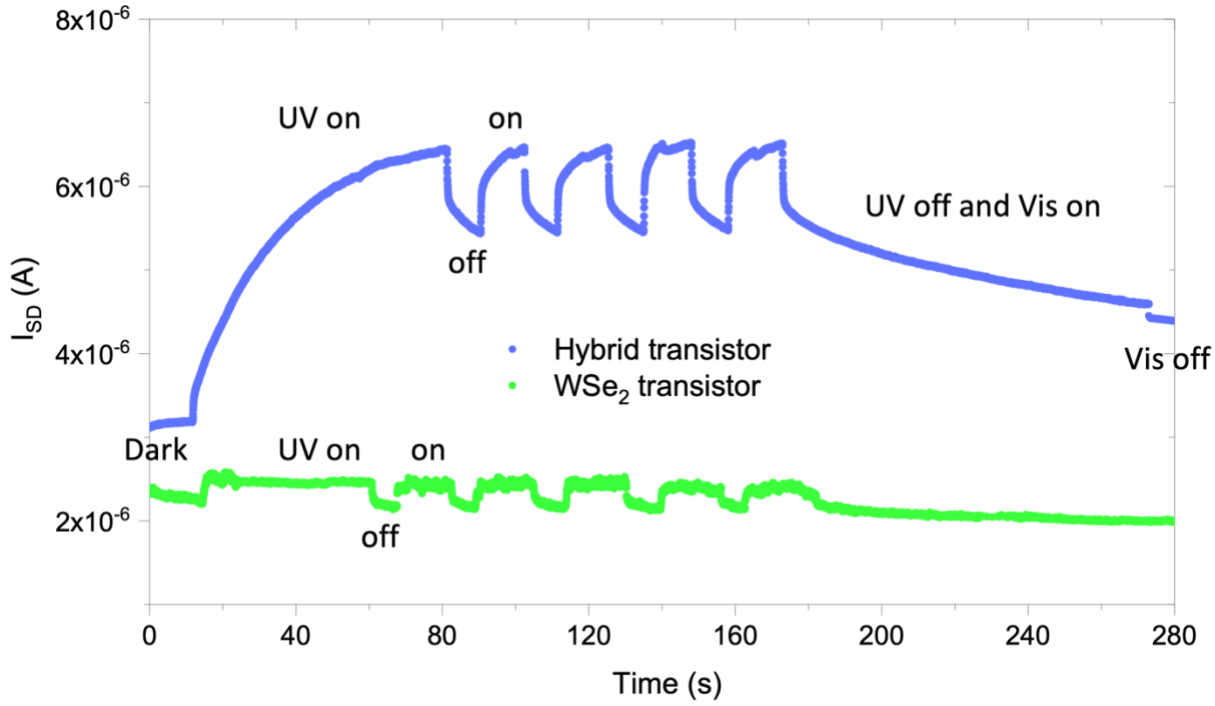

Figure 5.4 Ultrasensitive UV response of the hybrid transistor. Unlike the measurements above, the photocurrent is included in this data plot as we continuously switch the UV source on and off throughout the process. By turning the UV on, the current begins to increase with time that consists of contributions from both A3 molecules enhancement and photocurrent generated by the UV light. It takes approximately 60 seconds for the current to reach maximum as confirmed by Figure 2 since that is the time for all the A3 molecules to switch from trans state to cis state with our UV source. After reaching the maximum, we can simply monitor the photocurrent by switching UV on and off. As demonstrated, the photocurrent on/off ratio is 2 times higher for the hybrid transistor when normalized to their respective dark currents. In the last segment of the hybrid transistor, we turned off the UV light and switched on the visible light to observe the effect of molecules' relaxation on the current. As expected, the current gradually decays as the molecules' relaxation is a much slower process.

5.2.4 Ultrasensitive UV photoresponse of the hybrid transistor

Finally, the UV response of the hybrid transistor is demonstrated in Figure 5.4. Unlike the previous measurements that are conducted under dark condition, the photocurrent generated by the UV light (150 μW/cm^2) is monitored here as we continuously switch the UV source on and off throughout the process for both hybrid and bare WSe_2 phototransistors. The dark current of the hybrid transistor is approximately 30% higher than that of the bare WSe_2 transistor that is consistent with the previous discussion (Figure 5.2c). After turning on the UV source, the current begins to increase with time which consists of contributions from both A3 molecules enhancement and photocurrent generated by the UV light. It takes approximately 60 seconds for the current to reach maximum as confirmed by Figure 5.1 since that is the time required for all the A3 molecules to switch from *trans* state to *cis* state with our UV source. After reaching the maximum value, we simply monitor the photocurrent by switching the UV source on and off. Both the dark current and the photocurrent enhancement caused by A3 molecules and UV light are significant on the hybrid transistor, as compared to those of the bare WSe_2 transistor. The enhancement can be attributed to both strain and charge transfer, as discussed in the previous section. We note that since one critical condition for sensitive photodetectors is the signal to noise ratio (the photocurrent versus dark current), we calculate the UV photocurrent on/off ratios of our hybrid transistor device and find that it is about three times higher than the bare WSe_2 device. When normalized the UV power to the incident area, the UV photoresponsivity of the hybrid transistor is estimated to be 155 A/W, which is more than four-fold higher than its bare WSe_2 counterpart (37 A/W), hence making it a superior UV photodetector. In the last segment of the hybrid transistor exposure sequence, we turn off the UV light and switch on the visible light (55 μW/cm^2) to observe the effect of the A3 molecules' relaxation. As expected, the total current gradually decays as A3 molecules convert

from *cis* state back to *trans* state and release the strain on the monolayer WSe_2. We note that the current remains at a higher level compared to the original dark current in this time window as the relaxation is a much slower process as discussed above (120 minutes from our visible light source). Finally, the visible light is switched off. The hybrid phototransistor exhibits not only tunable mobility but also superior UV photodetection ability.

5.3 Conclusion

In summary, we have developed highly sensitive phototransistors based on monolayer 2D semiconductors and photoactive molecules with tunable and ultra-high field-effect carrier mobility. By photo-isomerizing the underlaying A3 molecules using UV and visible light, the carrier mobility of the hybrid FET device can be tuned from 50 to as high as 125 cm^2/Vs, which is comparable to most recent reported high performance TMDs based transistors. We then investigate the possible enhancement mechanisms of charge transfer and strain by looking into the threshold voltage of the hybrid device before and after UV exposure and calculating the charge density variations. Consequently, the strain is the primary mechanism for increased channel current and hence the enhanced carrier mobility. This hybrid design not only optimize the intrinsic properties of organics and inorganics but also broaden new capabilities that can be used for the next generation IC chips with tunable and high mobility and ultrasensitive UV photodetectors.

5.4 Methods

5.4.1 Hybrid transistor fabrication

Monolayer WSe_2 were exfoliated from commercial crystals (HQ Graphene) and then transferred onto bilayer A3 thin films on Si/SiO_2 substrates using PDMS stamps (Gel Pak PF films). Potential monolayer WSe_2 samples were identified by optical contrast using Nikon upright microscope, and further confirmed using PL spectroscopy using 532 nm CW laser excitation and Princeton Instrument spectrometer (IsoPlane 320). The samples were then patterned using photolithography, followed by metal deposition (Cr/Au with thicknesses of 5/50 nm) and lift off process.

5.4.2 Device testing

A probe station is used to measure the IV output and transfer characteristics of the devices along with the 2901a series source meter units from Keysight Technologies. The photoresponse of the devices is measured by irradiating the samples with UV flood exposure from a commercial UV lamp. The devices are measured under room temperature ambient environment.

5.5 References

(1) Radisavljevic, B.; Radenovic, A.; Brivio, J.; Giacometti, V.; Kis, A. Single-Layer MoS2 Transistors. *Nat. Nanotechnol.* **2011**, *6*, 147–150.

(2) Lopez-Sanchez, O.; Lembke, D.; Kayci, M.; Radenovic, A.; Kis, A. Ultrasensitive Photodetectors Based on Monolayer MoS 2. *Nat. Nanotechnol.* **2013**, *8*, 497–501.

(3) Lembke, D.; Kis, A. Breakdown of High-Performance Monolayer MoS2 Transistors. *ACS Nano* **2012**, *6*, 10070–10075.

(4) Wang, H.; Yu, L.; Lee, Y.-H.; Shi, Y.; Hsu, A.; Chin, M. L.; Li, L.-J.; Dubey, M.; Kong, J.; Palacios, T. Integrated Circuits Based on Bilayer MoS2 Transistors. *Nano Lett.* **2012**, *12*, 4674–4680.

(5) Shen, P. C.; Su, C.; Lin, Y.; Chou, A. S.; Cheng, C. C.; Park, J. H.; Chiu, M. H.; Lu, A. Y.; Tang, H. L.; Tavakoli, M. M.; *et al.* Ultralow Contact Resistance between Semimetal and Monolayer Semiconductors. *Nature* **2021**, *593*, 211–217.

(6) Zhang, W.; Chiu, M. H.; Chen, C. H.; Chen, W.; Li, L. J.; Wee, A. T. S. Role of Metal Contacts in High-Performance Phototransistors Based on WSe2monolayers. *ACS Nano* **2014**, *8*, 8653–8661.

(7) Dean, C. R.; Young, A. F.; Meric, I.; Lee, C.; Wang, L.; Sorgenfrei, S.; Watanabe, K.; Taniguchi, T.; Kim, P.; Shepard, K. L.; *et al.* Boron Nitride Substrates for High-Quality Graphene Electronics. *Nat. Nanotechnol.* **2010**, *5*, 722–726.

(8) Laturia, A.; Van de Put, M. L.; Vandenberghe, W. G. Dielectric Properties of Hexagonal Boron Nitride and Transition Metal Dichalcogenides: From Monolayer to Bulk. *npj 2D Mater. Appl.* **2018**, *2*, 1–7.

(9) Peelaers, H.; Van De Walle, C. G. Effects of Strain on Band Structure and Effective

Masses in MoS2. *Phys. Rev. B - Condens. Matter Mater. Phys.* **2012**, *86*, 1–5.

(10) Qi, J.; Lan, Y. W.; Stieg, A. Z.; Chen, J. H.; Zhong, Y. L.; Li, L. J.; Chen, C. D.; Zhang, Y.; Wang, K. L. Piezoelectric Effect in Chemical Vapour Deposition-Grown Atomic-Monolayer Triangular Molybdenum Disulfide Piezotronics. *Nat. Commun.* **2015**, *6*, 1–8.

(11) Shen, T.; Penumatcha, A. V.; Appenzeller, J. Strain Engineering for Transition Metal Dichalcogenides Based Field Effect Transistors. *ACS Nano* **2016**, *10*, 4712–4718.

(12) Lee, W.; Hwangbo, Y.; Kim, J. H.; Ahn, J. H. Mobility Enhancement of Strained Si Transistors by Transfer Printing on Plastic Substrates. *NPG Asia Mater.* **2016**, *8*.

(13) Conley, H. J.; Wang, B.; Ziegler, J. I.; Haglund, R. F.; Pantelides, S. T.; Bolotin, K. I. Bandgap Engineering of Strained Monolayer and Bilayer MoS2. *Nano Lett.* **2013**, *13*, 3626–3630.

(14) Schmidt, R.; Niehues, I.; Schneider, R.; Drüppel, M.; Deilmann, T.; Rohlfing, M.; De Vasconcellos, S. M.; Castellanos-Gomez, A.; Bratschitsch, R. Reversible Uniaxial Strain Tuning in Atomically Thin WSe2. *2D Mater.* **2016**, *3*, 2–9.

(15) Klajn, R.; Nachtigall, O.; Kördel, C.; Urner, L. H.; Haag, R.; Popeney, C. S.; Haag, R.; Li, Z.; Lv, Y.; Ren, L.; *et al.* Reversible Uniaxial Strain Tuning in Atomically Thin WSe2. *Nano Lett.* **2014**, *4*, 1–9.

(16) Amin, B.; Kaloni, T. P.; Schwingenschlögl, U. Strain Engineering of WS2, WSe2, and WTe2. *RSC Adv.* **2014**, *4*, 34561–34565.

(17) Aslan, O. B.; Deng, M.; Heinz, T. F. Strain Tuning of Excitons in Monolayer WSe2. *Phys. Rev. B* **2018**, *98*, 115308.

(18) Liu, X.; Wang, Y.; Li, F.; Li, Y. Two-Dimensional Stanane: Strain-Tunable Electronic Structure, High Carrier Mobility, and Pronounced Light Absorption. *Phys. Chem. Chem.*

Phys. **2016**, *18*, 14638–14643.

(19) Pak, S.; Lee, J.; Lee, Y. W.; Jang, A. R.; Ahn, S.; Ma, K. Y.; Cho, Y.; Hong, J.; Lee, S.; Jeong, H. Y.; *et al.* Strain-Mediated Interlayer Coupling Effects on the Excitonic Behaviors in an Epitaxially Grown MoS2/WS2 van Der Waals Heterobilayer. *Nano Lett.* **2017**, *17*, 5634–5640.

(20) Desai, S. B.; Seol, G.; Kang, J. S.; Fang, H.; Battaglia, C.; Kapadia, R.; Ager, J. W.; Guo, J.; Javey, A. Strain-Induced Indirect to Direct Bandgap Transition in Multilayer WSe 2. *Nano Lett.* **2014**, *14*, 4592–4597.

(21) Liu, T.; Liu, S.; Tu, K. H.; Schmidt, H.; Chu, L.; Xiang, D.; Martin, J.; Eda, G.; Ross, C. A.; Garaj, S. Crested Two-Dimensional Transistors. *Nat. Nanotechnol.* **2019**, *14*, 223–226.

(22) Choi, H. H.; Yi, H. T.; Tsurumi, J.; Kim, J. J.; Briseno, A. L.; Watanabe, S.; Takeya, J.; Cho, K.; Podzorov, V. A Large Anisotropic Enhancement of the Charge Carrier Mobility of Flexible Organic Transistors with Strain: A Hall Effect and Raman Study. *Adv. Sci.* **2020**, *7*, 1–10.

(23) Zeng, L.; Holmér, J.; Dhall, R.; Gammer, C.; Minor, A. M.; Olsson, E. Tuning Hole Mobility of Individual P-Doped GaAs Nanowires by Uniaxial Tensile Stress. *Nano Lett.* **2021**, *21*, 3894–3900.

(24) Ge, Y.; Wan, W.; Feng, W.; Xiao, D.; Yao, Y. Effect of Doping and Strain Modulations on Electron Transport in Monolayer MoS2. *Phys. Rev. B - Condens. Matter Mater. Phys.* **2014**, *90*, 1–6.

(25) Dong, M.; Babalhavaeji, A.; Collins, C. V.; Jarrah, K.; Sadovski, O.; Dai, Q.; Woolley, G. A. Near-Infrared Photoswitching of Azobenzenes under Physiological Conditions. *J. Am.*

Chem. Soc. **2017**, *139*, 13483–13486.

(26) Crivillers, N.; Orgiu, E.; Reinders, F.; Mayor, M.; Samorì, P. Optical Modulation of the Charge Injection in an Organic Field-Effect Transistor Based on Photochromic Self-Assembled-Monolayer-Functionalized Electrodes. *Adv. Mater.* **2011**, *23*, 1447–1452.

(27) Merino, E.; Ribagorda, M. Control over Molecular Motion Using the Cis-Trans Photoisomerization of the Azo Group. *Beilstein J. Org. Chem.* **2012**, *8*, 1071–1090.

(28) Zhou, H.; Xue, C.; Weis, P.; Suzuki, Y.; Huang, S.; Koynov, K.; Auernhammer, G. K.; Berger, R.; Butt, H. J.; Wu, S. Photoswitching of Glass Transition Temperatures of Azobenzene-Containing Polymers Induces Reversible Solid-to-Liquid Transitions. *Nat. Chem.* **2017**, *9*, 145–151.

(29) Kördel, C.; Popeney, C. S.; Haag, R. Photoresponsive Amphiphiles Based on Azobenzene-Dendritic Glycerol Conjugates Show Switchable Transport Behavior. *Chem. Commun.* **2011**, *47*, 6584–6586.

(30) Cheng, C. H.; Yang, D. S.; Kim, J.; Deotare, P. B. Self-Erasable and Rewritable Optoexcitonic Platform for Antitamper Hardware. *Adv. Opt. Mater.* **2020**, *8*, 1–5.

(31) Hussain, S. A.; Dey, B.; Bhattacharjee, D.; Mehta, N. Unique Supramolecular Assembly through Langmuir – Blodgett (LB) Technique. *Heliyon* **2018**, *4*, e01038.

(32) Li, Z.; Lv, Y.; Ren, L.; Li, J.; Kong, L.; Zeng, Y.; Tao, Q.; Wu, R.; Ma, H.; Zhao, B.; *et al.* Efficient Strain Modulation of 2D Materials via Polymer Encapsulation. *Nat. Commun.* **2020**, *11*, 1–8.

(33) Deng, S.; Sumant, A. V.; Berry, V. Strain Engineering in Two-Dimensional Nanomaterials beyond Graphene. *Nano Today* **2018**, *22*, 14–35.

Chapter 6 Conclusion

6.1 Summary of research work

In Chapter 2, we combined organic and inorganic (2D TMDs) semiconductors that enable us to integrate complementary advantages of each material system into a single hybrid material platform. Specifically, we investigated the energy transfer mechanisms across a hybrid interface consisting of j-aggregates of organic dye and monolayer molybdenum disulphide (MoS_2). The excellent overlap between the photoluminescence spectra of j-aggregates and the absorption of MoS_2 *B*-exciton, enabled the material system to be used to study Förster resonance energy transfer (FRET) across the hybrid interface. We reported a short Förster radius of 1.88 nm for the hybrid system. We achieved this by fabricating photodetectors based on the hybrid organic-inorganic interface that combined the high absorption of organics with high charge mobility of inorganics. Concomitantly, the hybrid photodetectors showed nearly 93 ± 5 % enhancement of photoresponsivity in the excitonic spectral overlap regime due to efficient energy transfer (ET) from j-aggregate to MoS_2. This work not only provided valuable insight into the ET mechanism across such hybrid organic-inorganic interfaces but also demonstrated the feasibility of the platform for designing efficient energy conversion and optoelectronic devices.

In Chapter 3, we followed up the work from Chapter 2 by investigating the energy transport in the same organic-inorganic (2D TMDs) hybrid platform formed between semiconductors that

supported stable room temperature excitons. We found that following photoexcitation, fast-moving *hot* hybrid charge transfer excitons (HCTEs) were formed in about 36 ps *via* scattering with optical phonons at the interface between j-aggregates of organic dye and inorganic monolayer MoS_2. Once the energy fell below the optical phonon energy, the excess kinetic energy was relaxed slowly *via* acoustic phonon scattering resulting in energy transport that was dominated by fast-moving *hot* HCTEs that transitioned into *cold* HCTEs in about 110 ps. We modeled the exciton-phonon interactions using Fröhlich and deformation potential theory and attributed the prolonged transport of *hot* HCTEs to phonon bottleneck. We found that the measured diffusivity of HCTEs in both *hot* and *cold* regions of transport was higher than the diffusivity of MoS_2 *A* exciton and verified these results by conducting the experiments with different excitation energies. This work not only provided significant insight into the initial energy transport of HCTEs at organic-inorganic hybrid interfaces, but also contributed to the formulation of a complete physical picture of the energy dynamics in hybrid materials, which were poised to advance applications in energy conversion and optoelectronic devices.

In Chapter 4, we explored another territory of organic-2D TMDs hybridization by utilizing nanoscale strain engineering to create a self-erasable and rewritable platform for anti-tamper hardware. The reversible structural change between *trans* and *cis* isomers in azobenzene (A3) molecules was utilized to strain the overlying tungsten diselenide (WSe_2) monolayer, thereby affecting its optical bandgap. Using such hybrid material combination we generated large (>1%) local strain that resulted in dramatic shift (> 11 nm) in photoluminescence wavelength. The strain in layered A3 films could be rapidly relaxed under exposure to visible light or could be retained up to seven days under dark condition. Thus, by utilizing hyperspectral imaging, we demonstrated a self-erasable and rewritable optoexcitonic platform that responded to environmental changes

(light/temperature) to detect tampering of hardware system. In addition, the results opened avenues for varied applications in information storage, time sensitive self-destructive memories to light detection.

In Chapter 5, we followed up the work from Chapter 4 and applied strain engineering that used nanometer scale two-dimensional semiconductors and allowed for the realization of high performance optoelectronic devices by inducing strain on an ultrathin and uniform conducting channel with enhanced carrier mobility. In this study, we developed highly sensitive field-effect transistors (FETs) based on monolayer two-dimensional tungsten diselenide (WSe_2) and azobenzene based molecules with tunable carrier mobility. The underlaying photoactive molecules were photo-isomerized between *trans* and *cis* states using UV and visible light that created strain on monolayer WSe_2, enhancing the carrier mobility of the hybrid transistor device from 50 to as high as 125 cm^2/Vs, approximately an order of magnitude higher than typical TMDs based transistors. Furthermore, the hybrid transistor exhibited sensitive UV photodetection ability, with photoresponsivity more than four times higher than its bare WSe_2 counterpart. The hybrid transistor broadened the horizon of isolated components toward novel and multi-functional IC chips.

6.2 Future outlook

In spite of significant effort to gain insight on hybrid interfaces and achieve functional devices with organic-inorganic heterojunctions, the following key limitations and related challenges remain to be addressed. Functional applications of the hybrid heterojunctions strongly depend on charge carrier transport occurring at the heterointerface between organic and inorganic

semiconductors. However, extensive theory or models that govern the interface charge and exciton transport at the 2D limit are still needed to explain more complicated phenomena. Most theories and assumptions are still developed based on bulk material systems describing the interface physics at macroscopic scale that may not be the real case for 2D materials. Even though the combination of 2D TMDs and organic materials have extraordinary potential for flexible device applications, and despite the limited number of inspiring demonstrations of conceptual flexible devices, the industrial scale transformation of the existing conceptual devices should not be underestimated. In terms of electronic device applications, as the major building block of modern semiconductor electronics, the performance of organic-inorganic heterojunction transistors should be on par with state-of-the-art silicon technologies. However, the low carrier mobility and especially inferior charge injection of organic semiconductors severely hinder the development of high speed transistors and the apparent short channel effect encountered by the organic electronics. Challenges are always accompanied by opportunities, with ongoing promising scientific results and increasing integration capabilities, I believe that hybrid interfaces of organics and 2D inorganics have a bright future to advance future technologies.